



**TECHNISCHE
UNIVERSITÄT
DRESDEN**

**Synthesis, Characterization and Chemical
Functionalization of Nitrogen Doped Carbon Nanotubes
for the Application in Gas- and Bio-Sensors**

Von der Fakultät Maschinenwesen
der
Technischen Universität Dresden
zur
Erlangung des akademischen Grades

Doktoringenieur (Dr.-Ing.)

angenommene Dissertation

M. Eng. Yangxi Fu

geboren am 02.11.1987 in Shaanxi (China)

**Vorsitzender der
Promotionskommission**

Prof. Dr. -Ing. habil. Markus Kästner
Technische Universität Dresden

1. Gutachter

Prof. Dr. Gianaurelio Cuniberti
Technische Universität Dresden

2. Gutachter

Prof. Dr.-Ing. Thomas Wallmersperge
Technische Universität Dresden

Tag der Einreichung: 28.04.2017

Tag der Verteidigung: 24.10.2017

Abstract

In this work, a chemiresistor-type sensing platform based on aligned arrays of nitrogen-doped multi-walled carbon nanotubes (N-MWCNTs) was developed. Our N-MWCNT based sensors can be made on both rigid and flexible substrates; they are small, have low power consumption and are suitable for highly efficient and reliable detection of different biomolecules and gases, at room temperature. The performance of these sensors was demonstrated for avian influenza virus (AIV) subtype H5N1 DNA sequences and toxic gases NO and NH₃ at low concentrations.

In our study, chemical vapor deposition (CVD) method was applied to synthesize vertically aligned nitrogen doped carbon nanotube arrays on a large area (> 1 cm²) on Si/SiO₂ substrate using Fe/Al₂O₃ layer as a catalyst and a mixture of ethanol and acetonitrile as a C/N source. Especially, the diameter, length, nitrogen-doping concentration and morphology of the nanotubes were controllably tailored by adjusting the thickness of catalyst film, reaction duration and temperature as well as the amount of nitrogen-containing precursor.

For integrating N-MWCNTs into chemiresistor devices, we developed a direct contact printing method for a dry, controllable and uniform transferring and positioning of the CVD-grown vertical nanotubes onto well-defined areas of various rigid and flexible substrates. After horizontally aligned N-MWCNT arrays were formed on a target substrate, interdigitated metallic microelectrodes with an interspacing of 3 μm were deposited perpendicular to the nanotube alignment direction to fabricate chemiresistor devices for biomolecule and gas sensing. This way, well-aligned nanotubes were laid across the Au/Cr interdigitated electrode fingers, had a strong adhesion with the electrodes and served as conducting channels bridging the electrodes.

The N-MWCNT based chemiresistor device was applied as a label-free DNA sensor for a highly sensitive and fast detection of AIV subtype H5N1 DNA sequences. For this, the nanotubes were functionalized with probe DNA, which was non-covalently attached to sidewalls of the N-MWCNTs via π - π interaction. Such functionalized sensors were applied to quantitatively detect complementary DNA target with concentration ranging from 20 pM to 2 nM after 15 min incubation at room temperature. The sensors showed no response to non-complementary DNA target for concentrations up to 2 μM showing an excellent selectivity.

Investigations on the efficient gas sensing of N-MWCNT-based chemiresistor of reducing/oxidizing gases NH₃ and NO were also reported in this work. The aim was to assess the possibility for N-MWCNTs to be applied as innovative sensing materials for room temperature gas sensing. N-MWCNTs with varying doping levels (N/C ratio of 5.6 to 9.3at%) were used as sensing materials and exposed to NH₃ (1.5-1000 ppm) and NO (50-1000 ppm) for exploring and

comparing their sensing performance. This study offered an effective route for further modification of CNTs according to various sensing application.

Finally, our investigations showed a high potential of the developed N-MWCNT-based sensing platform for various applications ranging from environmental monitoring to point-of-care medical diagnostics.

Kurzfassung

Die vorliegende Arbeit zeigt die Entwicklung einer Chemiresistor-Sensorplattform, die auf einem Array von mehrwandigen, mit Stickstoff dotierten Kohlenstoff-Nanoröhrchen basiert (nitrogen-doped multi-walled carbon nanotubes, N-MWCNTs). Die Sensoren sind für eine hocheffiziente und zuverlässige Detektion von verschiedenen Biomolekülen und Gasen bei Raumtemperatur geeignet. Sie sind mikroskopisch klein, können sowohl auf starren als auch auf flexiblen Substratmaterialien aufgebracht werden und zeichnen sich durch geringen Energieverbrauch aus. Die Leistungsfähigkeit dieser Sensoren wurde durch Nachweis von DNA-Sequenzen des Vogelgrippe-Virus Typ H5N1 und geringer Konzentrationen der gesundheitsschädlichen Gase Stickstoffmonooxid (NO) und Ammoniak (NH₃) demonstriert.

Bei unseren Untersuchungen wurde die Methode der chemischen Gasphasenabscheidung (chemical vapor deposition, CVD) verwendet, um eine Matrix aus vertikal angeordneten N-MWCNTs auf großen Flächen (> 1 cm²) auf einem Si/SiO₂-Substrat zu synthetisieren, wobei eine Fe/Al₂O₃-Oberflächenschicht als Katalysator und eine Mischung aus Ethanol und Acetonitril als Kohlenstoff- und Stickstoffquelle verwendet wurden. Speziell durch Einstellung der Schichtdicke des Katalysatorfilms, der Reaktionsdauer und der Temperatur sowie des Mengenanteils des stickstoffhaltigen Präkursors konnten Durchmesser, Länge, Stickstoffkonzentration und Morphologie der Nanoröhrchen kontrolliert werden.

Die Integration der Nanoröhrchen in Chemiresistor-Sensorelemente erfolgte durch ein direktes Kontaktprinting-Verfahren, das ein trockenes, kontrollierbares und einheitliches Auftragen von mittels CVD abgeschiedenen Kohlenstoff-Nanoröhrchen auf definierte Flächen der unterschiedlichen starren und elastischen Substratmaterialien ermöglicht. Nach der Bildung von horizontal angeordneten Reihen von Kohlenstoff-Nanoröhrchen auf einem Targetmaterial wurden interdigitale Metallelektroden mit einem Abstand von 3 µm senkrecht zu der Vorzugsrichtung der Kohlenstoff-Nanoröhrchen aufgedampft, um daraus die Chemiresistor-Bauelemente zur sensorischen Erfassung von Biomolekülen und Gasen herzustellen. Auf diese Weise sorgt die starke Adhäsion zwischen den geordneten Nanoröhrchen und der fingerähnlichen Anordnung der interdigitalen Au/Cr-Elektroden für eine Brückenbildung der Leitungsbahnen zwischen den Elektroden.

Die N-MWCNT-basierte Chemiresistor-Plattform wurde als markierungsfreier DNA-Sensor für eine hochsensitive und schnelle Detektion von DNA-Sequenzen des Vogelgrippe-Virus vom Typ H5N1 verwendet. Dafür wurden die Nanoröhrchen mit DNA-Sonden funktionalisiert, die über eine nichtkovalente π - π -Wechselwirkung an den Seitenflanken der Nanoröhrchen anhaften. Die so funktionalisierten Sensoren konnten zur quantitativen Erfassung von komplementären DNA-

Targets im Konzentrationsbereich zwischen 20 pM und 2 nM nach 15 min Inkubationszeit bei Raumtemperatur verwendet werden. Die Sensoren zeigten eine hohe Selektivität, für nichtkomplementäre DNA-Targets in Konzentrationen von bis zu 2 μ M waren sie nicht sensitiv.

Als weitere Anwendung eines N-MWCNT-basierten Chemiresistors werden Untersuchungen zur effizienten Gaserfassung der reduzierenden/oxidierenden Gase NH_3 und NO vorgestellt. Ziel war es, die Einsatzmöglichkeit dieser Kohlenstoff-Nanoröhrchen als innovative Sensormaterialien für die Erfassung von Gasen bei Raumtemperatur zu beurteilen. Die N-MWCNT-Nanoröhrchen mit variierender Dotierungsstufe (N/C-Verhältnis zwischen 5.6 und 9.3 at%) wurden als Sensormaterial den Gaskonzentrationen von 1.5-1000 ppm NH_3 und von 50-1000 ppm NO ausgesetzt, um damit die Sensorleistungen zu untersuchen und zu vergleichen. Diese Studie bietet einen effektiven Ansatz zur weiteren Modifikation von Kohlenstoff-Nanoröhrchen in Bezug auf verschiedene Anwendungsfelder in der Sensorik.

Letztendlich zeigten unsere Untersuchungen das hohe Potenzial der hier entwickelten Sensor-Plattform auf der Basis von N-MWCNT-Nanoröhrchen für verschiedene Anwendungen – von der Umweltüberwachung bis hin zur medizinischen Point-of-Care Diagnostik.

Content

ABSTRACT	II
KURZFASSUNG	IV
CONTENT	VI
LIST OF ABBREVIATIONS	IX
LIST OF SYMBOLS	XI
LIST OF FIGURES	XIII
LIST OF TABLES	XVIII
1. INTRODUCTION	1
1.1. BACKGROUND	1
1.2. MOTIVATION	2
1.3. FUNDAMENTALS OF CARBON NANOTUBES	4
1.3.1. <i>ELECTRONIC STRUCTURE OF CARBON NANOTUBES</i>	8
1.3.2. <i>PROPERTIES OF CARBON NANOTUBES</i>	9
1.3.2.1. ELECTRICAL PROPERTIES	10
1.3.2.2. MECHANICAL PROPERTIES	10
1.3.2.3. THERMAL PROPERTIES	11
1.3.3. <i>DOPING OF CNTS</i>	11
1.3.3.1. BORON FUNCTIONALIZED NANOTUBES	11
1.3.3.2. NITROGEN FUNCTIONALIZED NANOTUBES	12
2. EXPERIMENTAL	16
2.1. PROCESSING AND EQUIPMENT FOR THE GROWTH OF CNTS	16
2.1.1. <i>PREPARATION OF SAMPLES</i>	16
2.1.2. <i>CVD SETUP AND PROCESS</i>	16
2.2. CNTS TRANSFER PROCESS	17
2.2.1. <i>CLEANING</i>	17
2.2.2. <i>SURFACE MODIFY</i>	18
2.2.3. <i>CONTACT PRINTING</i>	18
2.3. DEVICE FABRICATION	19
2.3.1. <i>PHOTOLITHOGRAPHY</i>	19
2.3.2. <i>THERMAL EVAPORATION AND LIFT-OFF PROCESS</i>	21
2.3.3. <i>ANNEALING</i>	21
2.4. CHARACTERIZATION METHODS	22
2.4.1. <i>SCANNING ELECTRON MICROSCOPY (SEM)</i>	22
2.4.2. <i>TRANSMISSION ELECTRON MICROSCOPY (TEM)</i>	22
2.4.3. <i>X-RAY PHOTOELECTRON SPECTROSCOPY (XPS)</i>	22
2.5. ELECTRICAL AND SENSING MEASUREMENTS	23

2.5.1. ELECTRICAL CHARACTERIZATION	23
2.5.2. BIOSENSING MEASUREMENT.....	24
2.5.2.1. DNA PREPARATION	24
2.5.2.2. FUNCTIONALIZATION STEPS.....	24
2.5.2.3. DNA SENSING	25
2.5.3. GAS SENSING EXPERIMENT.....	25
3. SYNTHESIS AND CHARACTERIZATION OF VERTICALLY ALIGNED N-MWCNT ARRAYS	27
3.1. OVERVIEW OF SYNTHESIS METHOD	27
3.1.1. "IN SITU" DOPING METHOD.....	27
3.1.1.1. ARC-DISCHARGE	27
3.1.1.2. CHEMICAL VAPOR DEPOSITION.....	28
3.1.2. POST TREATMENT METHOD	29
3.1.2.1. THERMAL TREATMENT	29
3.1.2.2. LOW ENERGY N_2^+ ION IMPLANTATION.....	29
3.1.2.3. N_2 PLASMA TREATMENT	29
3.2. RESULTS AND DISCUSSION	31
3.2.1. CATALYST	32
3.2.2. GROWTH RATE AND DURATION	34
3.2.3. PRECURSOR COMPOSITION AND GROWTH TEMPERATURE	36
3.3. CONCLUSION	43
4. HORIZONTAL ALIGNMENT OF CNT ON SURFACES	45
4.1. OVERVIEW OF CNTS TRANSFER	45
4.1.1. WET METHODS	46
4.1.1.1. DROP CASTING	46
4.1.1.2. SPRAY COATING.....	47
4.1.1.3. SPIN COATING	47
4.1.1.4. DIP COATING	48
4.1.1.5. INK-JET PRINTING	48
4.1.2. DRY METHODS	49
4.1.2.1. SOFT LITHOGRAPHY.....	49
4.1.2.2. TRANSFER PRINTING	50
4.1.2.3. DIRECT CONTACT PRINTING	51
4.2. RESULTS AND DISCUSSION	52
4.2.1. STABILITY AND SCALABILITY.....	55
4.2.1.1. THE INFLUENCE OF EXTERNAL PRESSURE	56
4.2.1.2. THE INFLUENCE OF SURFACE DENSITY	58
4.2.2. CHEMICAL FUNCTIONALIZATION OF TARGET SUBSTRATES.....	59
4.2.3. OTHER INSULATED TARGET SUBSTRATES	63
4.2.3.1. QUARTZ.....	63
4.2.3.2. GLASS.....	64
4.2.3.3. POLYIMIDE FILM.....	65
4.3. CONCLUSION	66

5. PERFORMANCE OF N-MWCNTS BASED BIOSENSOR	67
5.1. OVERVIEW OF AIV DETECTION	67
5.1.1. AVIAN INFLUENZA VIRUS	67
5.1.2. DIRECT DETECTION TECHNIQUES.....	68
5.1.2.1. HISTORIC “GOLD STANDARD” IDENTIFICATION	68
5.1.2.2. DNA DETECTION	70
5.1.3. INDIRECT DETECTION TECHNIQUES	72
5.1.3.1. ELISA.....	72
5.1.3.2. ELECTROCHEMICAL IMMUNOSENSORS	72
5.1.3.3. APTAMER-BASED DIAGNOSTICS.....	73
5.2. FUNCTIONALIZATION	73
5.2.1. COVALENT FUNCTIONALIZATION OF CARBON NANOTUBES	74
5.2.2. NON-COVALENT FUNCTIONALIZATION OF CARBON NANOTUBES.....	74
5.3. RESULTS AND DISCUSSION	76
5.3.1. CNT CHARACTERIZATION AND DEVICE LAYOUT.....	76
5.3.2. FUNCTIONALIZATION AND ELECTRICAL CHARACTERIZATION.....	78
5.3.3. QUANTITATIVE DETECTION OF TARGET DNA	79
5.3.4. THE INFLUENCE OF DOPING CONCENTRATION ON SENSING BEHAVIOR.....	81
5.3.5. SELECTIVITY.....	82
5.4. CONCLUSION	84
6. PERFORMANCE OF N-MWCNTS BASED GAS SENSOR	86
6.1. OVERVIEW OF CNT BASED GAS SENSORS	86
6.2. RESULTS AND DISCUSSION	88
6.2.1. CNT CHARACTERIZATION AND DEVICE LAYOUT.....	88
6.2.2. ANNEALING EFFECT	90
6.2.3. EXPOSURE TO AMMONIA	91
6.2.4. EXPOSURE TO NO.....	95
6.2.5. APPLICATIONS IN ENVIRONMENTAL AND HUMAN BREATH MONITORING	96
6.3. CONCLUSION	98
7. SUMMARY AND OUTLOOK.....	99
7.1. SUMMARY	99
7.2. REMAINING ISSUES AND OUTLOOK.....	100
APPENDIX A.....	103
BIBLIOGRAPHY.....	104
ACKNOWLEDGEMENTS	136

List of abbreviations

0D	Zero dimension
1D	One dimension
2D	Two dimension
3D	Three dimension
AACVD	Aerosol-assisted CVD
AFM	Atom force microscope
AIV	Avian influenza virus
BOE	Buffered oxide etch
cELISA	Competitive enzyme-linked immunosorbent assay
CNTs	Carbon nanotubes
CVD	Chemical vapor deposition
DFT	Density-functional theory
DI	Deionized
DNA	Deoxyribonucleic acid
DNA T	Target DNA
EDAC	N-ethyl-N'-(3-dimethylaminopropyl)carbodiimide hydrochloride
ELISA	Enzyme-linked immunosorbent assay
FET	Field effect transistor
GCE	Glassy carbon electrode
HA	Haemagglutinin
HI	Hemagglutination-inhibition
HPAIV	Highly pathogenic avian influenza virus
HRTEM	High-resolution transmission electron microscope
I-V	Current vs. voltage
MFC	Mass flow controller
MWCNT(s)	Multi-walled carbon nanotube(s)

NA	Neuraminidase
N/C	Nitrogen/carbon
N-CNT(s)	Nitrogen doped carbon nanotube(s)
NHS	N-hydroxysuccinimide
N-MWCNT(s)	Nitrogen doped multi-walled carbon nanotube(s)
N-SWCNT(s)	Nitrogen doped single-walled carbon nanotube(s)
NW(s)	Nanowire(s)
ODTS	Octadecyltrichlorosilane
PB	Phosphate buffer
PCR	Polymerase chain reaction
PDMS	Poly-dimethylsiloxane
PECVD	Plasma-enhance CVD
PET	Polyethylene terephthalate
PoCT	Point-of-care testing
PMMA	Poly(methyl methacrylate)
RNA	Ribonucleic acid
RT-PCR	Reverse transcription polymerase chain reaction
SD	Source-drain
ssDNA	Single-stranded DNA
SEM	Scanning electron microscope
STM	Scanning tunneling microscope
SWCNTs	Single-walled carbon nanotubes
SWCNT-FET	Single-walled carbon nanotube based field effect transistor
TEM	Transmission electron microscope
UV	Ultraviolet
VLS	Vapor-liquid-solid
XPS	X-ray photoelectron spectroscopy

List of symbols

\mathbf{a}	Unit cell vector for the hexagonal lattice
a	Length of the unit cell vector
a_{cc}	Carbon-carbon bond length
$\mathbf{C}_{n,m}$	Chiral vector
c	Circumference of the nanotube
d_t	Carbon nanotube diameter
E	Electron energy
e	Elementary charge
E_A^{AB}	Interfacial binding energy between materials A and B
E_F	Fermi energy
E_g	Energy gap
h	Planck constant
I	Current
I_{ds}	Drain-source current
I_g	Gate current
\mathbf{k}	Wave vector
K	Dirac point
L	The length of CNT
L_m	Mean free path length
L_φ	Phase relaxation length
(n, m)	Chiral index
p	Vapor pressure
P	External pressure
R	Resistance
R_0	Initial resistance
R/R_0	The change of resistance

S	Sensitivity
T	Temperature
t	Time
V	Voltage
Γ	Center of the Brillouin zone
γ	The nearest-neighbor hopping parameter
$\gamma_{A(B)}$	Surface free energy of material A(B)
γ_{AB}	Interfacial free energy
θ	Chiral angle

List of figures

- Fig. 1.1:** The hybridization of an s-orbital (blue) and two p-orbitals (red) forms three planar sp^2 hybridized orbitals (orange) with a characteristic angle of 120° presented by Philschatz [40]. The remaining hybridized orbital $2p_z$ is parallel to the z axis, which is not shown here. 4
- Fig. 1.2:** (a) Mother of all graphitic forms presented by Geim [39], that graphene is a 2D building structure for carbon materials of all other dimensionalities, which can be wrapped up into 0D Bucky balls, rolled into 1D nanotubes or stacked into 3D graphite. (b) Electronic dispersion of graphene in the honeycomb lattice presented by Neto [43], right: zoom in of the energy bands close to one of the Dirac points. 5
- Fig 1.3:** (a) A graphene sheet with lattice vectors \mathbf{a}_1 and \mathbf{a}_2 presented by A. Maiti [56]. θ is the chiral angle for a (3,1) CNT; orange and purple lines are along the circumferences of armchair and zigzag tubes, respectively. (b) A (5,5) armchair tube. (c) A (9,0) zigzag tube [56]. 7
- Fig. 1.4:** (a) Tight-binding electronic band structure of graphene showing that the Γ , M , and K high symmetry points [59]. (b) Cutting lines of the (5,5), (7,1), and (8,0) tubes (solid) mapped onto Brillouin zone [59]. (c) The DOS vs. energy E for (5,5), (7,1), and (8,0) nanotubes showing the effect of chirality on the band gap: (5,5) armchair and (7,1) display a metallic behavior, while (8,0) tube is a semiconductor [59, 66]. 9
- Fig. 1.5:** Scheme illustration of types of nitrogen species that can be incorporated into graphitic carbon. 12
- Fig. 1.6:** Schematic representations of the band structure and Fermi level of (a) pristine metallic carbon nanotubes in the ideal case, (b) realistic metallic carbon nanotubes in surrounding gaseous environment, (c) N doped CNTs. Blue triangles stand for the energies in the conduction bands, while purple for the valence bands. The Fermi level is shown by the pink zone as a range of its possible positions. (Depending on the amount of adsorbed oxygen and incorporated dopants, Fermi level can be situated higher or lower within the pink area.) 13
- Fig. 1.7:** HRTEM images (left) and the schematics of electron transport inside MWCNT (right) of (a) pristine MWCNT (copyright of Nanotech Innovations) and (b) nitrogen doped bamboo-like MWCNT. (The scale of databar in HRTEM images is 5 nm.) 15
- Fig. 2.1:** Photographs (a) and schematic diagram (b) of CVD setup for the synthesis of N-MWCNTs. 17
- Fig. 2.2:** (a) Schematic representation of ODTS modification of a Si/SiO₂ substrate, ODTS molecules are densely packed on the surface of substrate. (b) Schematic of the direct contact-printing transfer process of CVD-grown vertically aligned MWCNTs. (P, pressure). 18

Fig. 2.3: Schematic view of the chemiresistor-type devices in this study: (a) a single gas sensor, (b) biosensor matrix. Cr/Au electrodes were patterned on the surface of substrate with pre-patterned horizontally aligned MWCNT arrays at certain areas.	19
Fig. 2.4: Flow charts of the photolithography to fabricate interdigitated electrode patterns on substrate with horizontally aligned CNTs using (a) positive and (b) negative resists.	20
Fig. 2.5: Schematic diagram of the photolithography and metal electrodes deposition process, resist AZ5214e was applied as (a) positive and (b) negative photoresist.	21
Fig. 2.6: (a) An optical photo of probe station for the electrical measurements, the inset is an image of two tungsten needles probing the sensing device. (b) Diagrams for measuring SD I-V curves (top) and transfer characteristics (bottom) of devices.	23
Fig. 2.7: Schematic configuration of the gas measurement system with a small volume gas chamber equipped with read-out electronics for the sensor measurements [111].	26
Fig. 3.1: (a) Widely-accepted growth mechanisms for CNTs: (top) tip-growth model, (down) base-growth model [150]. (b) TEM image of a bamboo-liked nitrogen doped carbon nanotube. (c) Magnified HRTEM image of the tip of a nanotube.	32
Fig. 3.2: SEM images of N-CNTs grown from (a) 0.5, (b) 1.0, and (c) 2.0 nm Fe multilayer system. (d) The comparison of diameter and length of the N-MWCNTs grown from 0.5 and 1.0 nm Fe multilayer system. (Data bar: 1 μm , precursor: pure acetonitrile, reaction temperature: 885 $^{\circ}\text{C}$.)	33
Fig. 3.3: (a) SEM micrograph of the N-MWCNTs grown via CVD with duration of: 1, 3, 5, 7, 10 and 15 min. The (b) length and (c) growth rate of N-MWCNTs plotted as a function of reaction duration ranging from 0 to 15 min.	35
Fig. 3.4: (a) Vapor pressure of acetonitrile and ethanol at ambient temperatures, which was calculated through Antoine equation as shown in appendix A. (b) XPS C1s and N1s spectra of N-CNTs synthesized by using varying concentrations of acetonitrile in ethanol as feedstocks. N1s spectra showing different types of nitrogen incorporated in N-MWCNTs synthesized from (c) 100, (d) 50, (e) 30, and (f) 20vol% acetonitrile in ethanol.	38
Fig. 3.5: Low- (left) and high-magnification (right) TEM images showing bamboo-like N-MWCNTs with N doping concentration of (a) 8.3, (b) 7.3, (c) 5.5 and (d) 5.0 at%.	41
Fig. 3.6: Statistic distribution of (a) diameter, (b) number of sidewalls and (c) distance of bamboo-like compartments of CVD-grown nitrogen doped multiwalled MWCNTs with a varying N concentration from 5 to 8.3%. The growth temperature of sample 1 is 850 $^{\circ}\text{C}$, while that of sample 2-4 is 900 $^{\circ}\text{C}$	42
Fig. 4.1: A relationship diagram of wet and dry transfer methods.	46
Fig. 4.2: Schematic and brightfield microscope image of the “coffee ring” effect, that deposits formed from evaporating drops containing particles [194].	47

- Fig. 4.3:** Transfer-printing process flows for CNT devices onto non-conventional substrates reported by Thanh [177]: (a) the CNT devices are pre-fabricated on a Si/SiO₂ substrate, (b) PMMA is spin-coated on the device, (c) SiO₂ is etched, (d) and the PMMA/CNT-device film floats in the water bath, (e, f) the PMMA/CNT-device film is flipped over and placed on a foreign substrate, (g, h) PMMA/CNT-device film is printed on a non-conventional substrate followed with dissolution of PMMA. 50
- Fig. 4.4:** Comparison of morphologies of nanotubes (a) before and after the transfer process through (b) drop casting and (c) direct contact printing methods. (a) Scanning electron micrographs of close-packed arrays of N-MWCNTs on a large region of Si/SiO₂ growth substrate. (b) SEM images of inhomogeneous network of N-MWCNTs transferred on Si/SiO₂ target substrate through drop casting N-MWCNTs/SDS dispersion. (c) SEM image of regular array assembly of isolated N-MWCNTs located on a large area of Si/SiO₂ target substrate which was transferred from the growth substrate through direct contact printing with an external pressure of ~3 kPa. 53
- Fig. 4.5:** (a) Schematic presentation of the direct contact printing process of CVD grown MWCNTs. (b, c) SEM image of N-MWCNTs synthesized from pure acetonitrile grown on a Si/SiO₂ substrate before (b) and after (c) contact-printing process. (d) SEM image of the alignment of N-MWCNTs transferred onto Si/SiO₂ target substrate. The external pressure applied during contact-printing process is 2 kPa. (The scale of data-bar is 1 μm.) 54
- Fig. 4.6:** (a) Top view (SEM image) of N-MWCNTs synthesized from pure acetonitrile grown on a Si/SiO₂ substrate before contact-printing process. (b) The length distribution of transferred N-MWCNTs on target substrate Si/SiO₂ plotted as a function of cycle numbers. (c) SEM images of horizontally aligned N-MWCNTs on Si/SiO₂ target substrate, which were repeatedly transferred from a same MWCNT sample for 1-8 times. (The scale of data-bar is 2 μm.) 56
- Fig. 4.7:** SEM images of transferred N-MWCMT arrays onto Si/SiO₂ target substrates via direct contact printing with different pressure of (a) 0.5, (b) 1.0, (c) 2.0, and (d) 3.0 kPa exerted on the interface between the growth and the target substrates. (The scale of data-bar is 1 μm.) 57
- Fig. 4.8:** (a-c) SEM images of vertical N-MWCNTs grown on the Si/SiO₂ substrates via CVD method which have various coverage of nanotubes: (a) 24.8%, (b) 17.3% and (c) 1.6%, respectively. (d-f) SEM images of resulting horizontal N-MWCNTs transferred from the growth substrate (a-c) to the target Si/SiO₂ substrates, the coverage of surface in (d-f) is 0.9%, 0.8% and 0.2%, respectively. (The scale of the data-bar is 2 μm.) 59
- Fig. 4.9:** Water contact angles of target substrate Si/SiO₂ (a) before and (b) after ODTs surface modification (The volume of the droplet is 10 μL). 61
- Fig. 4.10:** SEM image of N-MWCNTs directly contact-printed at 5 kPa on the surface of Si/SiO₂ substrate without (a) or with (b) ODTs treatment. (The scale of the data-bar is 5 μm.) 62

Fig. 4.11: SEM images of (a) regular array assembly of N-MWCNTs and (b) a single N-MWCNT printed on the quartz substrate partially covered by deposited Cr/Au (3nm/50nm) interdigitated electrodes with an interspacing distance of $\sim 3 \mu\text{m}$	63
Fig. 4.12: (a) SEM image of a large region of uniformly printed N-MWCNTs arrays coated with Cr/Au (3nm/50nm) interdigitated electrodes (interspacing distance of $3 \mu\text{m}$) on a glass substrate. (b) Higher magnification SEM image of N-MWCNT arrays bridging two neighboring interdigitated electrodes.	64
Fig. 4.13: SEM images of N-MWCNTs arrays printed on polyimide films (a) without or (b) with the coverage of Cr/Au (3nm/50nm) interdigitated electrodes.	65
Fig. 5.1: AIV isolation, culture and identification protocol flowchart [242].	69
Fig. 5.2: Schematic diagram of electrical detection of biosensors reported by Chartuprayoon et al. [6]: (a) chemiresistor, (b) back-gated chemical field effect transistor, and (c) ion-gated field effect transistor.....	72
Fig. 5.3: (a) Schematic illustration of the CNT based chemiresistor-type DNA sensor functionalization and sensing steps. (b) Chemical structure of Triton™ X-100 [288]. (c) Image of the probe station during electronic characterization of a sensing device.....	75
Fig. 5.4: Optical images of CNT chemiresistor biosensor chips each containing 400 sensing devices fabricated on various substrates (from left to right: quartz, glass and Kapton® polyimide film).....	76
Fig. 5.5: Low-voltage SEM images of N-MWCNT based chemiresistor sensor device on (a) quartz, (b) glass, (c) Kapton® substrate; the higher magnified images in the insets show horizontally aligned N-MWCNT arrays bridging Cr/Au interdigitated electrodes. (The interspacing distance of the electrodes is of $3 \mu\text{m}$.).....	77
Fig. 5.6: (a) Typical I-V curves of N-MWCNT (N concentration of $\sim 8.3\%$) based chemiresistor DNA sensor before and after annealing in vacuum at $200 \text{ }^\circ\text{C}$. (b) I-V curves of N-MWCNT based chemiresistor DNA sensor before and after functionalization steps. (c) Resistance of the device before and after the functionalization experiments measured at voltage $V = 2.0 \text{ V}$ for every step.	78
Fig. 5.7: (a) I-V curves and (b) resistance change (R/R_0) of N-MWCNT based DNA sensors (N concentration of $8.3\text{at}\%$) as the response to processing with increasing concentrations of DNA T from 0 pM to 2 nM ($V = 2.0 \text{ V}$).....	80
Fig. 5.8: Comparison of sensing responses of sensors based on N-doped MWCNTs with N/C ratio of 9.3 (square), 8.2 (down-triangle) and 6.1% (up-triangle). All sensors show similar downwards trend of resistance change R/R_0 for concentrations up to 200 pM . Increase of R/R_0 at 2 nM is attributed to the competing effect described in the text. Lines connecting points are used to guide an eye. ($V = 2.0 \text{ V}$).....	82

Fig. 5.9: Functionalization steps and sensing response of N-MWCNT-based chemiresistive sensor to non-complementary H1N1 DNA T. Lines connecting points are used to guide an eye.	82
Fig. 6.1: Transfer characteristic change after exposure to NO ₂ (triangles) and NH ₃ (squares) of the SWCNT-FET gas sensor firstly reported by Kong et al. [15]	87
Fig. 6.2: Photos of gas sensing chemiresistor devices fabricated on (a) Si/SiO ₂ and (b) glass substrates. (c) Optical microscope image of interdigitated electrodes of the gas-sensing device fabricated on a glass substrate.....	89
Fig. 6.3: SEM images of interdigitated-electrode areas of N-MWCNT based gas sensors on glass substrate with N concentration of (a) 8.3, (b) 7.3, (c) 5.5 and (d) 5.0at%. Horizontally aligned N-MWCNT arrays lie under the electrodes with an interspacing distance of ~3 μm.....	89
Fig. 6.4: I-V curves of chemiresistor devices based on N-MWCNTs with varying N doping concentration of (a) 8.3 and (b) 5.0at% before and after annealing at 200 °C. The insets are the magnified range at the center area of the I-V curves.	91
Fig. 6.5: (a) Real-time resistance changes ($(R/R_0)\%$, $R_0 = 1.54 k\Omega$) of the N-MWCNT based gas sensor with nitrogen concentration of 5.5% as the response to increasing concentrations of NH ₃ ranging from 1.5 to 50 ppm ($V = 0.1 V$); exposure times are delimited by the vertically lines with the corresponding concentration. (b) Sensitivity ($S = R - R_0 /R_0 \times 100\%$) of the device as a function of NH ₃ gas concentrations.....	92
Fig. 6.6: Real-time sensing response ($R/R_0\%$) of N-MWCNT based resistive device with a N concentration of (a) 5.5 and (c) 8.3% upon exposure to NH ₃ gas at 200, 500 and 1000 ppm at room temperature ($V = 0.1 V$); exposure times are delimited by the vertically lines with the corresponding concentration. (b) The dependence of sensitivity ($ R - R_0 /R_0 \times 100\%$) of N-MWCNTs with N concentration of (b) 5.5 and (d) 8.3% on increasing concentration of NH ₃ gas.	94
Fig. 6.7: Real time response ($R/R_0\%$) of devices based on N-MWCNTs with different N-doping of (a) 5.0 and (b) 8.3% to 1000 ppm NO at a constant voltage of 0.1 V.....	96

List of tables

Table 1.1: Parameters of carbon nanotubes [58].....	7
Table 3.1: The comparison of N-doping methods and N concentration on CNT structures.	30
Table 3.2: Element concentration and concentration of pyridinic, quaternary and pyrrolic N (at%) in N-MWCNTs synthesized with 20%, 30%, 50% and 100% acetonitrile fraction.	39
Table 4.1: Contact angle and surface free energy for SiO ₂ substrates before and after ODTS surface treatment reported by Lim [217].	61
Table 5.1: Comparison of detection range of different sensors for AIV viruses.	83
Table 6.1: Composition of human breathing [333].....	98
Table A1: Vapor pressure of acetonitrile and ethanol at different temperatures from 10 to 40 °C.	103

1. Introduction

1.1. Background

With industrialization and urbanization rapidly expanding over the centuries, a series of public health problems caused by environmental contamination and emerging infectious diseases have arisen and attracted growing concern in the worldwide. The number of hazardous substances continues to increase, which poses a great threat to human health, like toxic gases, hazardous chemicals, bacteria, viruses and so on. Therefore, the detection and analysis of these substances become increasingly important in many areas, including the monitoring of air quality, detecting chemicals or harmful organisms, diagnosing virus and cancer cells, etc. [1-3]

Chemical sensor is a device that selectively detects specific chemical substance (analytes) from the environment and generates a measurable signal whose magnitude is functionally related to the analyte concentration [4, 5]. It plays an essential role in the fields of environmental protection and monitoring, disaster and disease prevention, as well as industrial analysis [6, 7]. Current technologies for toxic gases or disease virus detection are sensitive but still face many significant issues, like low stability, low selectivity, high analyst consumption, high energy consumption, large size of testing equipment as well as requiring trained lab professionals, etc. [8, 9] These serious issues make the current analysis to not fulfill the public imminent needs for fast, reliable, highly-sensitive, low-cost and user-friendly chemical sensors.

Ever since carbon nanotubes (CNTs) have been discovered by Iijima in 1991 [10], key milestones for the development of nanosized chemical sensor have been reached [11]. Carbon nanotubes have been proven to be sensitive to the environment, for example, oxygen absorption from the surroundings drives CNT devices into a p-type conducting state [12, 13]. Carbon nanotubes have comparable size with many analytes, like gas molecules, DNA sequence, virus, etc. Only a few absorbed molecules are sufficient to change their electronic characteristics, so chemical sensors based on CNTs can detect an extremely low concentration of analytes. Besides, CNTs also possess superior physical and electrical properties which make them become promising active materials for sensing, like tiny size leads to low energy consumption, high surface area to volume ratio results in high sensitivity, easy functionalization that allows for imbuing selectivity, good flexibility make them compatible with microfabrication techniques, and high thermal stability that allows them to be deployed in various environments [11].

In 1996, Britto [14] firstly applied CNTs as biosensors to detect the reversible oxidation of dopamine, then Dai and coworkers [15] demonstrated in 2000 that single-walled carbon nanotubes (SWCNTs) can be applied as a fast and sensitive gas sensor to NH_3 and NO at

ambient temperatures. To date, integrating CNTs with conventional chemical sensors is becoming increasingly popular in recent studies [16-19]. CNTs have been demonstrated that are sensitive to many gas species such as hydrogen (H₂) [20, 21], methane (CH₄) [22], oxygen (O₂) [12], carbon monoxide (CO) [23], etc. In addition, it has been found that many biomolecules such as proteins, enzymes, and DNA sequences, are easily adsorbed on to the nanotube sidewalls and can be attached directly to functional groups on the CNTs [24-26], which make CNTs a huge potential to be used in label-free, highly sensitive and selective chemical sensors for point-of-care (PoCT) diagnostics [24].

Although numerous scientific breakthroughs have been achieved, much research of CNT based chemical sensor still remains at a proof-of-concept and/or prototype stage [11]. Thanks to their small size and high aspect ratio, relatively strong van der Waals interaction between CNTs leads to agglomeration of CNTs in both powder and dispersion form. This makes individualization, processing, and integration of CNTs still quite challenging, thus greatly limits their sensing applications. Another big issue is that it is still difficult to predict whether a SWCNT is metallic or semiconducting in a raw mixture of as-synthesized SWCNTs. Difficulty in production or selection of pure semiconducting SWCNTs leads to very high price (1 mg of >99% pure semiconducting SWCNTs still costs 899 USD [27]), which greatly increases the cost of fabricated SWCNT based electronic devices, and thus limits their application.

1.2. Motivation

The main motivation for this work is the development of a series of small, stable, sensitive and low-cost CNT based chemical sensors fabricated in simple and controllable fabrication procedures, which could be applied to fast and reliably detect gas- and bio-molecules in the ambient temperature. More specifically, our study is facing boundaries between the controllable synthesis and functionalization of CNTs and the fabrication and integration of chemiresistive sensors implementing through CNTs. The goal is to link these components together for the purpose of gas sensing to NH₃ and NO as well as biosensing to avian influenza virus (AIV).

The prominent highlight of the study is a comprehensive picture of reliable CNT based chemical sensors from initial syntheses, fabrication to final detection was provided in detail, the entire content including controllable materials synthesis, well-defined nanostructure transfer and alignment, stable and standard nanodevice integration and fabrication process, as well as the application for gas- and bio-molecule detection. We aim to accurately control each step and make the whole process reliable, efficient, stable, low-cost, low power consumption and simple for fabrication.

As widely known, a number of nanostructures such as metal oxides, graphene, Si nanowire and conductive polymer have been reported in literature holding the potential as active materials in chemical sensors. Semiconducting metal oxides have been reported presenting high sensitivity to environmentally hazardous gases (e.g., WO_3 nanostructures are promising candidates for NO_2 sensing and gold-loaded SnO_2 sensors are very sensitive for NO and N_2O sensing) [28]. However, these sensors often operate at high temperatures (200-600 °C) to achieve enhanced chemical reactivity between the sensor materials and the gas molecules [29, 30], leading to high energy consumption and the requirement of complicated or expensive fabrication techniques. On the other hand, silicon nanowires show promising performance to DNA resulting from their high surface-to-volume ratio, but smaller nanostructures like CNTs with virtually all atoms on their surface provide additional advantages in DNA detection [31]. According to Yaqoob et al. [32], reduced graphene oxide has more active sites for the absorption of molecules in comparison to multi-walled CNTs (MWCNTs), while MWCNTs possess excellent mechanical flexibility and superior electrical properties. In addition, Jiménez-Cadena [33] pointed out that organic polymers are cheap and very sensitive to several analytes, but lack of selectivity and stability regarding time and temperature. Compared with other active nanostructures, CNT sensors usually offer advantages in terms of a smaller size, lower energy consumption, the capability of room-temperature operation, faster response and higher sensitivity [11, 24, 34-36].

MWCNTs and SWCNTs have similar properties. Compared with single-walled carbon nanotube, multi-walled carbon nanotube process inferior sensing performance because of its multilayer structure, that outer walls shield the inner nanotubes from chemical interactions [37]. Nonetheless, bulk synthesis of pure and well-aligned SWCNTs is quite difficult as it requires precise control over growth and atmospheric condition. Additionally, unknown proportional distribution of semiconducting and metallic nanotubes in the as-synthesized mixture also makes the sensing performance of devices lack stability, reliability, and repeatability. Compared with SWCNTs, MWCNTs exhibit these advantages, such as lower cost, ease of bulk synthesis, higher purity, higher tensile strength properties, enhanced thermal and chemical stability [37]. Therefore, multi-walled carbon nanotubes were selected as active materials in this study to simplify the whole synthesis and reduce the fabrication cost.

To improve the sensing performance of MWCNTs, nitrogen functionalization was applied, which have been proved to feasibly introduce active chemical sites as well as tailor the electronic properties of CNTs (see detailed description in section 1.3.3.2). Especially, well-aligned N doped MWCNTs (N-MWCNTs) with a controllable N-doping concentration could easily be synthesized via chemical vapor deposition (CVD) method. Due to this controllable synthesis, N-MWCNTs have a similar size distribution, similar electronic properties as well as active

chemical sites and can be considered as reliable materials for sensing devices, which is too hard to be achieved for SWCNTs.

1.3. Fundamentals of carbon nanotubes

Carbon element has six electrons, which occupy $1s^2$, $2s^2$ and $2p^2$ orbitals respectively. Four of those are valence electrons in $2s$, $2p_x$, $2p_y$ and $2p_z$ atom orbitals, which are capable of forming chemical bonds. When a carbon atom bonds with three neighboring carbon atoms, one s-orbital $2s$ combines with two p-orbitals $2p_x$ and $2p_y$ and form a set of planar sp^2 orbitals with a characteristic angle of 120° , known as sp^2 hybridization (see Fig. 1.1).

0-dimensional (0D) fullerenes, 1-dimensional (1D) carbon nanotubes, 2-dimensional (2D) graphene, and 3-dimensional 3(D) graphite are all belonged to $2p^2$ allotropes of carbon. Generally, 2D graphene in a hexagonal honeycomb structure is considered as a basic building block of other carbon allotropes, as shown in fig 1.2(a), which is available to be wrapped to generate fullerenes, rolled up to form carbon nanotubes and stacked to produce graphite [38, 39].

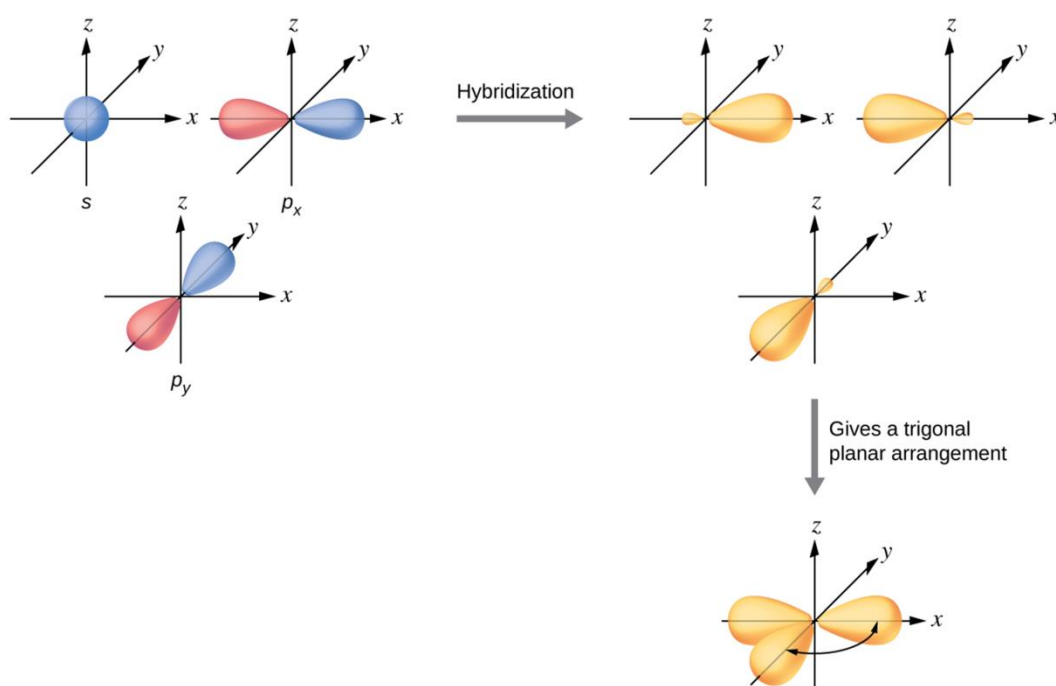


Fig. 1.1: The hybridization of an s-orbital (blue) and two p-orbitals (red) forms three planar sp^2 hybridized orbitals (orange) with a characteristic angle of 120° presented by

Philschatz [40]. The remaining hybridized orbital $2p_z$ is parallel to the z axis, which is not shown here.

In sp^2 hybridization, sp^2 orbitals aligned themselves to form the strong in-plane σ bonds, leaving the additional $2p_z$ orbitals arranged perpendicular to the plane. Each carbon atom contributes one π electron, and one electron has spin-up or spin-down states. Therefore, out-of-plane π orbitals overlap with neighboring carbon atoms, leading to the formation of the lower π bands (valance bands) and the upper π^* bands (conduction bands). At absolute zero temperature, π bands are completely filled while π^* bands are empty. These half-filled π -bands permit free moving electrons, which is responsible for the noticeable electrical conductivity of graphene. Based on a tight-binding model, the energy dispersion relation of graphene can be expressed with the wave vectors (k_x, k_y) [41]:

$$E(k_x, k_y) = \pm\gamma \cdot \left(1 + 4 \cos\left(\frac{\sqrt{3}k_x a}{2}\right) \cos\left(\frac{k_y a}{a}\right) + 4 \cos^2\left(\frac{k_y a}{2}\right) \right)^{1/2} \quad (1.1)$$

Where “ \pm ” applies to π^* - and π -bands; γ is responsible to the transfer integer between the nearest-neighbor π orbitals; k_x and k_y provide the wave vector \mathbf{k} , and a is the length of the unit cell vector. This energy dispersion is illustrated in Fig. 1.2(b), that the upper band π^* and the lower band π obey a linear dependence of energy on wave vector and meet at the Dirac points K [42]. At the Dirac points, the density of electron states (DOS) of graphene at the Fermi energy (E_F) is zero, thus explains graphene is a zero-bandgap semiconductor.

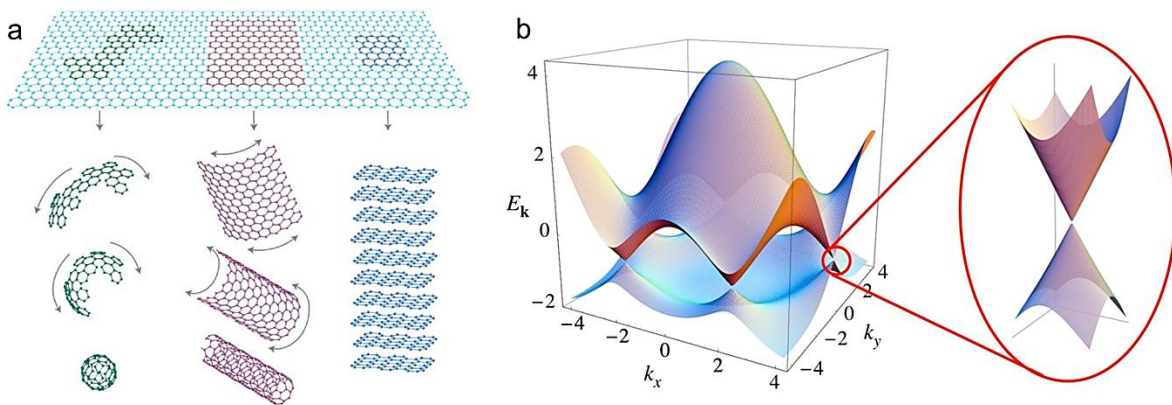


Fig. 1.2: (a) Mother of all graphitic forms presented by Geim [39], that graphene is a 2D building structure for carbon materials of all other dimensionalities, which can be

wrapped up into 0D Bucky balls, rolled into 1D nanotubes or stacked into 3D graphite. (b) Electronic dispersion of graphene in the honeycomb lattice presented by Neto [43], right: zoom in of the energy bands close to one of the Dirac points.

CNTs were firstly reported and characterized by Iijima in 1991 [10]. As a 1D allotrope of carbon, a carbon nanotube can be described as a graphene rolled into a hollow cylindrical tube, and its terminating caps are formed from pentagons and hexagons [10, 44, 45]. According to the number of rolled-up layers, carbon nanotubes can be divided into single-walled carbon nanotubes and multi-walled carbon nanotubes. SWCNTs have diameters typically between 0.43 and 2 nm [46, 47]. MWCNTs are multiple tubes encircling one another with an inter-wall spacing of 0.34-0.36 nm [45, 48, 49], which have diameters varying from 2 nm and up to more than 50 nm depending on wall numbers [50-54]. CNTs present extremely large length-to-diameter ratio, and their lengths can range from hundreds of nanometers to over 18.5 cm [55].

The structure of an ideal infinite and straight single-walled carbon nanotube can be described by the chiral vector $\mathbf{C}_{n,m}$ [44, 56], depending on its rolling-up direction (shown in Fig. 1.2). The $\mathbf{C}_{n,m}$ can be given by:

$$\mathbf{C}_{n,m} = n\mathbf{a}_1 + m\mathbf{a}_2 \quad (1.2)$$

where n and m are integers ($0 \leq |m| \leq |n|$), and \mathbf{a}_1 and \mathbf{a}_2 are uncial cell vectors for the hexagonal lattice.

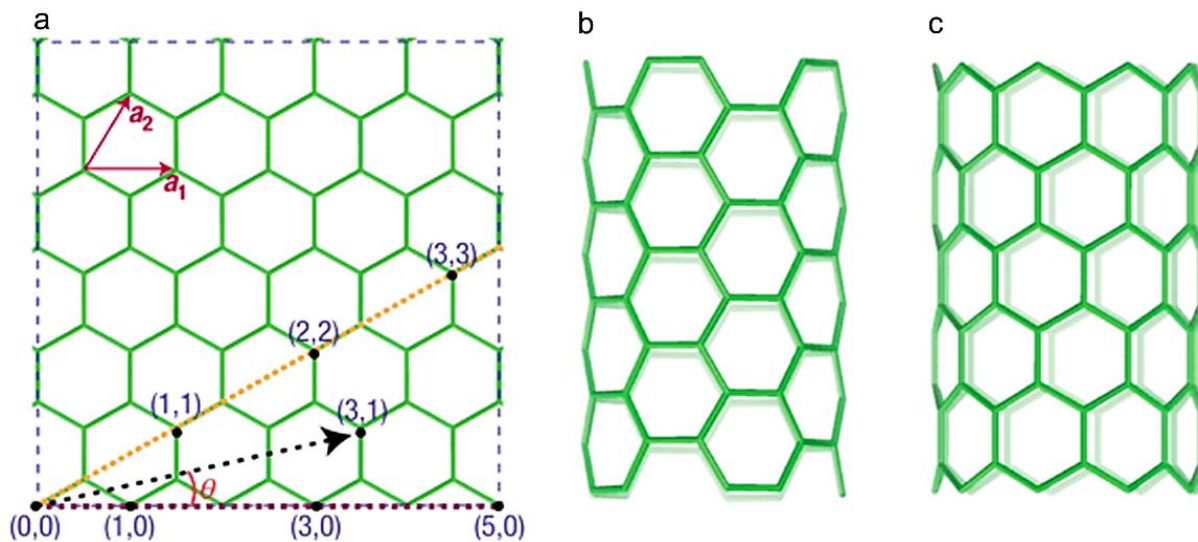


Fig 1.3: (a) A graphene sheet with lattice vectors \mathbf{a}_1 and \mathbf{a}_2 presented by A. Maiti [56]. θ is the chiral angle for a (3,1) CNT; orange and purple lines are along the circumferences of armchair and zigzag tubes, respectively. (b) A (5,5) armchair tube. (c) A (9,0) zigzag tube [56].

From the (n, m) indices, the chiral angle θ can be directly determined, which is the degree between the vectors \mathbf{C} and \mathbf{a}_1 ($0^\circ \leq |\theta| \leq 30^\circ$) [57]. As shown in Fig. 1.3(a), the armchair and zigzag nanotubes correspond to chiral angles of $\theta = 30^\circ$ and $\theta = 0^\circ$, respectively, and others are chiral nanotubes. From the (n, m) indices, some properties of SWCNTs can also be calculated, as shown in Table 1.1 [44, 58].

Table 1.1: Parameters of carbon nanotubes [58].

Symbol	Name	Formula	Value
a_{cc}	Carbon-carbon bond length		1.421 Å (graphite)*
a	Length of the unit cell vector	$a = \mathbf{a}_1 = \mathbf{a}_2 = a_{cc}\sqrt{3}$	2.461 Å
$\mathbf{C}_{n,m}$	Chiral vector	$\mathbf{C}_{n,m} = n\mathbf{a}_1 + m\mathbf{a}_2$	n, m : integers
$\mathbf{a}_1, \mathbf{a}_2$	Unit cell vector	$\left(\frac{\sqrt{3}}{2}, \frac{1}{2}\right)a, \left(\frac{\sqrt{3}}{2}, -\frac{1}{2}\right)a$	
c	Circumference of the nanotube	$c = a\sqrt{(n^2 + nm + m^2)}$	
d_t	Carbon nanotube diameter	$d_t = \frac{ \mathbf{C}_{n,m} }{\pi}$ $= \frac{\sqrt{3}a_{cc}}{\pi}\sqrt{m^2 + mn + n^2}$	
θ	Chiral angle	$\sin \theta = \frac{\sqrt{3}m}{2\sqrt{(n^2 + nm + m^2)}}$ $\cos \theta = \frac{2n + m}{2\sqrt{(n^2 + nm + m^2)}}$ $\tan \theta = \frac{\sqrt{3}m}{2n + m}$	$0^\circ < \theta < 30^\circ$

Note: for graphite $a_{cc} = 1.421$ Å [49], but for CNTs, the C-C bonds are elongated slightly due to the curvature of the tube, which does not exceed 0.008 Å [44].

1.3.1. Electronic structure of carbon nanotubes

Because ideal infinite SWCNTs can be considered as a rolled-up graphene sheet, the electronic structure can be described as a quantum phenomenon based on Brillouin zone of 2-dimensional graphene [58, 59]. Due to the periodic boundary conditions in the circumferential, the wave vectors \mathbf{k} along the rolling-up direction of nanotubes become quantized, while only a certain sets of the vectors along the tube axis is allowed (length of the tube $\gg d_t$). This defined the allowed modes along the direction of tube axis, which can be described as:

$$\mathbf{C} \cdot \mathbf{k} = 2\pi\mu, \quad |\mu| = 0, \dots, N - 1 \quad (1.3)$$

This can be indicated by the cutting lines in the Brillouin zone, which is depended on the nanotube's diameter and chirality [42]. Fig. 1.4(b) presents three different configurations of the cutting lines in Brillouin zone, that the configurations $n = m$ (8,8) and $n - m = 3i$ (7,1) corresponds to the cutting line crossing the K point resulting in metallic behavior; while the others $n - m \neq 3i$ correspond to the K point being located between two adjacent cutting lines, leading to semiconducting behavior [42]. Based on equation 1.2 and 1.3, band gap E_g of both a metallic or a semiconducting single-walled nanotube can be described by [59, 60].

$$E_g = 0, \quad \text{for } n - m = 3i, \quad |i| = 0, \dots, N - 1 \quad (1.4(a))$$

$$E_g = \frac{2\gamma a_{cc}}{d_t}, \quad \text{for } n - m \neq 3i, \quad |i| = 0, \dots, N - 1 \quad (1.4(b))$$

According to equation 1.4, 2/3 of the single-walled nanotubes correspond to semiconducting nanotubes and 1/3 to metallic nanotubes; the band gap of semi-conducting carbon nanotubes (sc-SWCNTs) depends on the nanotube's diameter [59, 61, 62]. According to experimental results reported by Collins et al. [63], SWCNTs with diameters of 1.0, 1.4, and 2.0 nm present electronic band gaps of approximately 0.85, 0.60, and, 0.43 eV, respectively. The corresponding density of electronic states for the (5,5), (7,1), and (8,0) tubes are shown in Fig. 1.4(c), that a sc-SWCNT has a density state of zero at Fermi level whereas a metallic SWCNTs has a finite DOS. As shown in Fig. 1.4(c), (7,1) tube also has a tiny gap attribute to its curvature effects, but which displays a metallic behavior at room temperature [59]. The existence of both semiconducting and metallic SWCNTs was also experimentally confirmed by Odom [64] and Wildöer [65] using scanning tunneling microscopy (STM) to characterize electronic density of state of SWCNTs. Because a single metallic layer of nanotubes results in the entire nanotube displaying metallic behavior, most multiwalled carbon nanotubes display a metallic behavior [53].

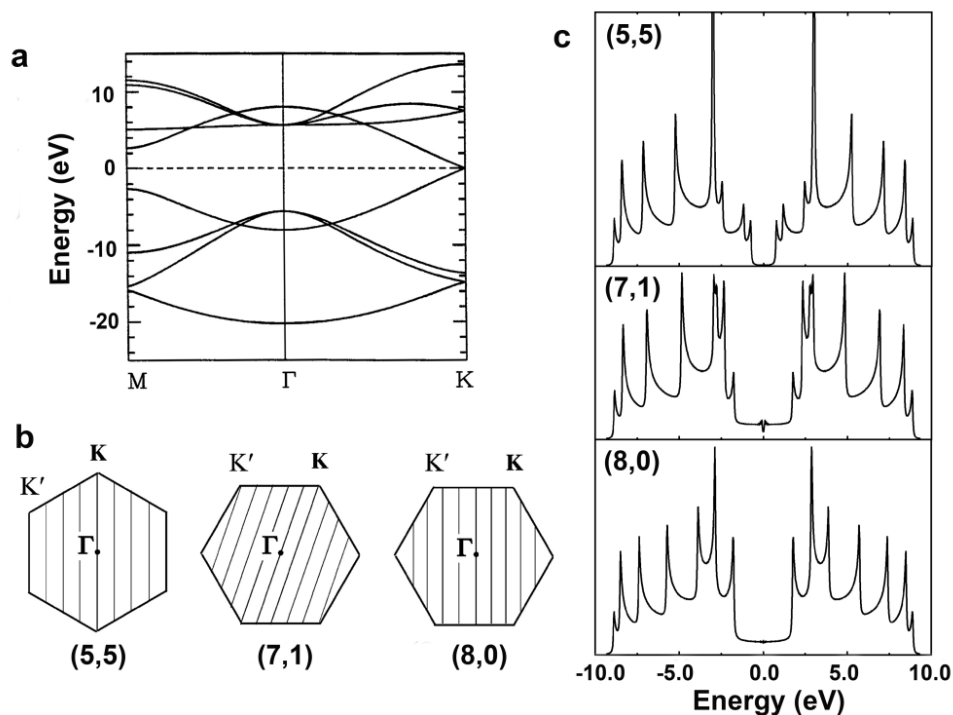


Fig. 1.4: (a) Tight-binding electronic band structure of graphene showing that the Γ , M , and K high symmetry points [59]. (b) Cutting lines of the (5,5), (7,1), and (8,0) tubes (solid) mapped onto Brillouin zone [59]. (c) The DOS vs. energy E for (5,5), (7,1), and (8,0) nanotubes showing the effect of chirality on the band gap: (5,5) armchair and (7,1) display a metallic behavior, while (8,0) tube is a semiconductor [59, 66].

Although electronic structures of carbon nanotubes are based on a graphene model, they still have slight deviations attribute to the curvature effects of nanotubes [13]. For instance, C-C bonds become slightly polarized after rolling-up into nanotubes, circumferential bonds elongate while axially oriented bonds shorten, leading to probable effects on nanotubes' conduction path [13].

1.3.2. Properties of carbon nanotubes

As known to all, CNTs exhibit remarkable electronic, mechanical, thermal and chemical properties, which have attracted numerous attention due to their potential applications in many different areas, such as mechanical reinforcement in polymer composites [67], as active elements in nanosized field effect transistor (FET) [68], and as sensitive materials in chemical sensors [69-71].

1.3.2.1. Electrical properties

Due to 1 dimension of SWCNTs, the conduction of a nanotube along the circumferential direction is quantized, which can be considered as charge carriers transmitting through a 1-dimensional conduction channel. The conduction mechanism of nanotubes depends on the nanotube's width (W) and length (L). The mean free path (L_m) is applied to describes the average distance over which the initial momentum of an electron is destroyed, and phase relaxation length (L_ϕ) is the length over which an electron changes most of its original phase [72]. For a nanotube, if $W > L_\phi$ and $L > L_m$, the nanotube displays a diffusive conduction; if $W < L_\phi$ and $L \sim L_m$, the nanotube present a quasi-ballistic behavior; and if $W < L_\phi$ and $L < L_m$, the nanotube is a ballistic conductor. Hertel et al. [73] studied electron-phonon interaction in SWCNTs at room temperature using femtosecond time-resolved photoemission measurements, and the result showed that the L_m in metallic SWCNTs is of the order of several micrometers. This length is well above the typical conducting channel lengths of SWCNT-based devices with a sub-micron range. Thus, CNTs can be regarded as excellent electronic conductors for low-power consumption electronics [13].

Due to multilayers, the electronic properties of MWCNTs are not as easy to control as those of SWCNTs [13], but which also have a potential for applying as ballistic conductors. According to Poncharal et al. [74], multiwalled carbon nanotubes also show ballistic conductivity at room temperature with the length of L_m in tens of microns range. But Sanvito [75] reported that the ballistic conduction properties of each SWCNT shell in a MWCNT may be destroyed, because an electron wave propagating along a SWCNT shell has a certain probability to be scattered into a neighboring shell. Therefore, L_m of MWCNTs is considerably shorter than that of SWCNTs at room temperature, resulting in a weaker 1D character of MWCNTs [13].

1.3.2.2. Mechanical properties

Because of the strong sp^2 covalent bonds between carbon atoms, CNTs have a simple chemical composition and bonding configuration but exhibit extraordinary mechanical properties [44, 45, 76]. The highest measured strength of a carbon nanotube is up to 63 GPa, which reaches an order of magnitude stronger than that of high strength carbon fibers [77]. In 1997, Lu [78] predicted Young's modulus of nanotubes, which is four times larger than that of the diamond. Overney et al. [32] calculated Young's modulus of short SWCNT using *ab initio* local density calculations, which was of 1500 GPa [79]. According to Zhang [76], Young's modulus of a nanotube can reach to 1.2 TPa.

1.3.2.3. Thermal properties

Due to strong sp^2 covalent bindings, long range crystallinity, long phonon mean free path, and large speed of sound, CNTs also exhibit prominent thermal properties along the tube axis [80]. According to Hone [81], the thermal properties of carbon nanotubes are dominated by phonons, not like other materials, the thermal conductivity of which are determined by the phonons and the electrons. Berber et al. [13] have calculated the phonon thermal conductivity of isolated nanotubes, the highest theoretical phonon thermal conductivity of an individual SWCNT can reach up to 37,000 W/mK, which is close to that of pure diamond, the highest thermal conductivity (41,000 W/mK) ever measured at 104 K [81]. Even at ambient temperature, the theoretical thermal conductivity for an isolated nanotube still can reach up to 6600 W/mK, exceeding the reported room-temperature thermal conductivity of pure diamond [81].

1.3.3. Doping of CNTs

CNTs exhibit specific chemical and physical properties; however, CNTs are not soluble and agglomerate easily due to strong van der Waals interactions [82, 83]. Additionally, pristine CNTs exhibit almost chemically inert surface, covalent attachment of molecules to completely sp^2 -bonded carbon atoms on nanotube surface has proven to be quite difficult [45]. Therefore, surface treatment of CNTs is necessary in order to improve the interaction with their surroundings. Several approaches are applied to increase the CNT reactivity: (i) the most common functionalization with strong acidic treatments introduce dangling bonds, diverse radicals and functional groups on the nanotubes' sidewalls, but also damage the structure of CNTs in the meanwhile, leading to degradation of their electronic properties [84, 85]; (ii) other methods involve the doping of CNTs by introducing heteroatoms within the nanotube's lattice, including B [86], N [85, 87], P [88, 89], Si [90], etc. Doping CNTs with heteroatoms generally can induce charge redistribution along the defective area, affect electronic properties and improve the surface reactivity of nanotubes [85, 88, 89, 91]. Among these heteroatoms, boron and nitrogen are the natural candidates because of their similar atomic sizes as that of carbon and of their electron acceptor and donor characters, respectively [92, 93].

1.3.3.1. Boron functionalized nanotubes

Doping CNTs with boron (B) atoms can improve the electronic and conductive properties of CNTs. Deng [94] reported that B doped carbon nanotubes are advantageous for the determination of glucose oxidase with cyclic voltammetry, due to extra edge plane sites on the surface and more functionalized groups at the defect sites of nanotubes. Mukhopadhyay [95] inserted lithium (Li) ions into boron doped MWCNTs, which was applied to for lightweight and energy-efficient Li batteries; boron doped MWCNTs present a higher reversible capacity (180

mAh/g) than that of pristine nanotubes (156 mAh/g) in the first cycle with almost equal Coulomb efficiencies of 55-58%.

1.3.3.2. Nitrogen functionalized nanotubes

As a neighboring element of carbon in the periodic table, nitrogen has a comparable atomic size with carbon, but its electronegativity (3.04) is larger than that of C (2.55) [96]. Incorporation of N atoms into nanotube lattice has been proven to be a feasible strategy to tailor the electronic properties of CNTs [97-99]. Additionally, Sadek [20] and Chen [13] reported that nitrogen doping on a CNT surface is an efficient alternative method of acidic treatment in order to improve reactivity of nanotubes, because incorporated nitrogen atoms in CNTs can be seen as regular defects which introduce chemically active sites on CNT sidewalls as well as change the chemical behaviour of the nanotubes.

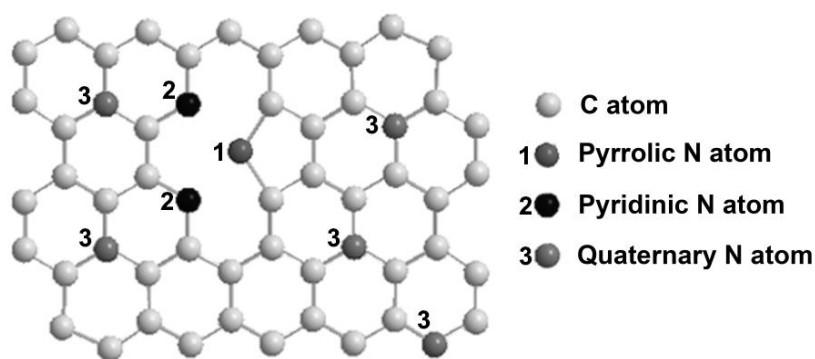


Fig. 1.5: Scheme illustration of types of nitrogen species that can be incorporated into graphitic carbon.

A schematic representation of a nitrogen doped carbon nanotube is presented in Fig. 1.5. Nitrogen can be found in three bonding configurations: pyridinic N, pyrrolic N and graphitic N. Pyridinic and pyrrolic N atoms are located at edge or defect sites. Quaternary N atoms substitute carbon atoms within the graphitic structure, which have the same configuration as graphitic carbon atoms but introduce extra electrons in the delocalized π -system. Ghosh et al. [100] reported that the pyrrolic nitrogen and quaternary nitrogen give rise to additional sub-levels in the unoccupied states near the Fermi level, leading to a higher electrical conductivity of the individual N-CNTs. Because of nitrogen incorporation, N-CNTs are less stable, less graphitic and more disordered than the pristine nanotubes [101].

Recently, N-doped CNTs also show their potential applied as active materials in the area of chemical sensing. According to previous studies, doping N heteroatoms in CNT lattice can efficiently tune its Fermi level [102]. As mentioned above, the electrical behavior of SWCNTs is either metallic or semiconductor depending on their chirality. However, the behavior of MWCNTs is metallic if, at least, one sheet has a metallic chirality [103]. Therefore, most MWCNTs can be considered as metallic nanotubes.

Fig. 1.6(a) presents a schematic view of the band structure of an ideal pristine metallic CNTs, that Fermi level E_F lies between the conduction and valence band (see Fig. 1.6(a)). However, carbon nanotubes are very sensitive to oxygen molecules in surrounding environment and exhibit p-type majority charge carriers under realistic conditions. Because of oxygen molecules adsorption and partial charge transfer from nanotubes to adsorbed oxygen molecules, Fermi level of nanotubes is shifted downwards into the valence band depending on the amount of adsorbates (see Fig. 1.6(b)). When doping CNTs with nitrogen atoms, the liberated electrons of N-CNTs will occupy empty states at the edge of the valence band of the nanotube [13], therefore Fermi energy of the N-doped CNTs will be located higher than Fermi energy of the undoped CNT as depicted schematically in Fig. 1.6(c). The exact position of Fermi level of particular N-CNTs depends on the amount of adsorbed oxygen molecules as well as incorporated nitrogen atoms, leading to either p-type or n-type behavior of N doped CNTs.

CNTs are inevitable to be exposed in air, and oxygen molecule adsorption shifts Fermi level of C CNTs away from its initial position downwards, but doping with N atoms can tune Fermi level and shift it back, close to its initial position as explained above. Therefore, N incorporation in nanotube lattice was predicted to improve the sensitivity of carbon nanotubes compared to pristine ones.

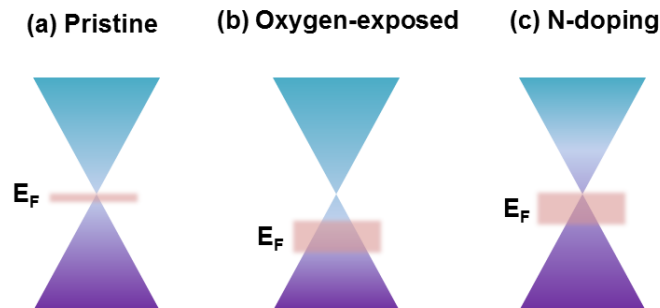


Fig. 1.6: Schematic representations of the band structure and Fermi level of (a) pristine metallic carbon nanotubes in the ideal case, (b) realistic metallic carbon nanotubes in

surrounding gaseous environment, (c) N doped CNTs. Blue triangles stand for the energies in the conduction bands, while purple for the valence bands. The Fermi level is shown by the pink zone as a range of its possible positions. (Depending on the amount of adsorbed oxygen and incorporated dopants, Fermi level can be situated higher or lower within the pink area.)

The high-resolution transmission electron microscopy (HRTEM) image in Fig. 1.7(a) presents the morphology and structure of a pristine multiwalled carbon nanotube, which can be considered as several graphene layers rolled-up in a cylindrical configuration with a straight hollow core inside. Since the electrons in the sp^2 -hybridized orbitals are strongly localized, charge transport in CNTs mainly realized with electrons in the π -bonds [13]. MWCNTs consist of a concentric arrangement of different diameter SWCNTs; the conductivity of each layer of MWCNTs behaves like a SWCNT along the axial direction, but is very poor between the layers (see schematic in Fig. 1.7(a)). Because of relatively large outer diameter as well as the interaction between inner shells, MWCNTs exhibit a weaker 1D character compared to SWCNTs [13].

HRTEM image in Fig. 1.7(b) shows the typical bamboo-like configuration of a nitrogen doped MWCNT: the inner sidewalls of N-MWCNTs are extremely affected by polygonal ends and disorder, while the outer walls are straight and flat. According to the literature [102, 104, 105], N-MWCNTs display a defective structure with more disruptions in the graphitic lattice and more edge plane sites compared to undoped MWCNTs, thus the conductivity of N-MWCNTs is significantly reduced compared to undoped ones.

However, N-MWCNTs are expected to be more sensitive to adsorbed molecules than pristine MWCNTs with a similar diameter when applying as sensing materials. As shown in the HRTEM images in Fig. 1.7, a pristine MWCNT with a diameter of 23.4 nm has 19 flat sidewalls which are available for electron transport, while a 15.8-nm N-MWCNT has only 4 straight and flat outer layers. According to the sp^2 -hybrid structure, defective inner-shells with polygonal (broken) ends behave a poor conductivity, therefore, only flat and straight outer layers of nanotubes can be considered as electron transport channels. This means the conductivity of N-MWCNT mainly depends on its outer layers, thus leading to a weaker intershells interaction as well as a larger change in resistance of N-MWCNTs when surrounding molecules are adsorbed. Additionally, N-doping also introduces more chemically active sites on the CNT sidewall. Therefore, sensing behavior of N-MWCNTs can be enhanced over the undoped MWCNTs [106-108].

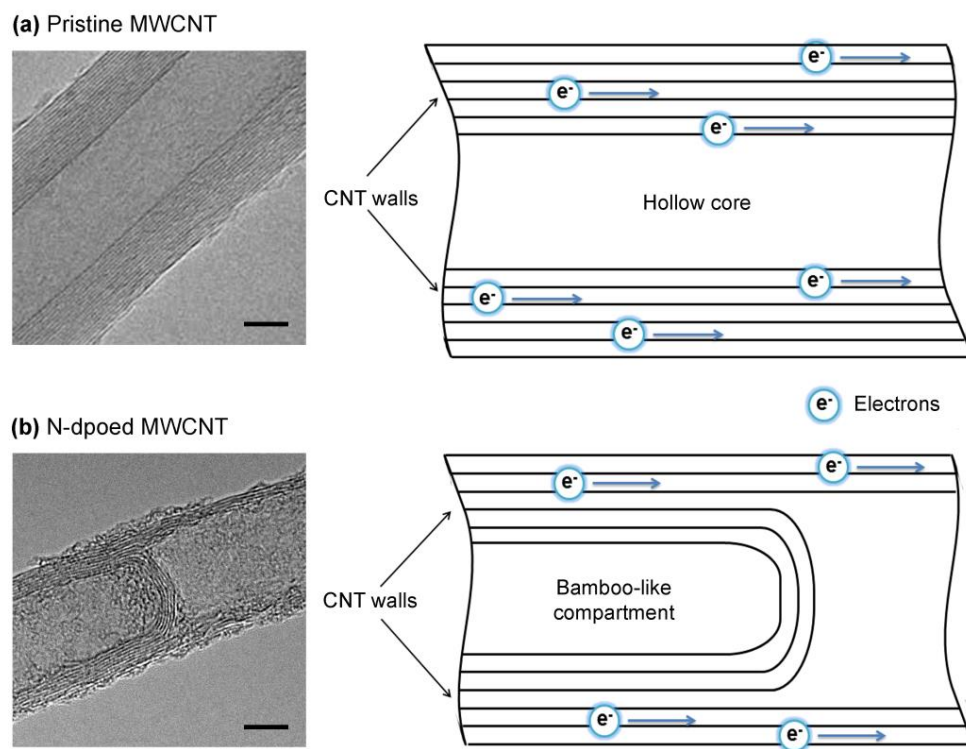


Fig. 1.7: HRTEM images (left) and the schematics of electron transport inside MWCNT (right) of (a) pristine MWCNT (copyright of Nanotech Innovations) and (b) nitrogen doped bamboo-like MWCNT. (The scale of databar in HRTEM images is 5 nm.)

2. Experimental

Present chapter describes the experimental procedure of the preparation of vertically aligned nitrogen doped carbon nanotubes and their integration into chemiresistive devices. This is followed by presentation of the relevance of two different applications, including gas sensing and biosensing. Furthermore, the equipment and characterization techniques are introduced. All the reagents applied in this study were of analytical grade and were used without further purification.

2.1. Processing and equipment for the growth of CNTs

2.1.1. Preparation of samples

Fe/Al₂O₃ metallic-layer was applied as catalysts. Ultra-thin Fe film was deposited after 10 nm thick Al₂O₃ layer built on the 400 nm thick SiO₂ surface of the Si wafer at room temperature using magnetron sputter deposition in a high vacuum chamber (base pressure: 1×10^{-7} mbar; Ar sputter pressure: 1×10^{-3} mbar). No capping layer was used. In the experiments presented in chapter 3, catalysts with three different Fe thicknesses were prepared, which were 0.5, 1.0 and 2.0 nm. After the deposition, the samples were exposed to the atmosphere resulting in natural oxidation of Fe to Fe₂O₃.

Acetonitrile/ethanol mixtures were employed as C/N source for CVD method, which were obtained from Sigma Aldrich. To adjust the concentration of N-containing source, acetonitrile was diluted into ethanol solution prior to use, the concentration of acetonitrile was 100, 50, 30, 20vol%.

2.1.2. CVD setup and process

Thermal CVD equipment was applied for N-MWCNT growth experiments (Fig. 2.1). The experimental setup for N-MWCNT synthesis comprises a quartz tube reactor with a diameter of 2.5 cm horizontally placed in a tunable resistance heating furnace, besides a pressure control and pumping system. The growth of N-MWCNTs was carried out in the center of a tubular quartz tube. Before all experiments, the quartz tube reactor underwent a procedure of evacuation till the pressure of 2 mbar was reached. The samples (catalyst-covered $1\text{cm} \times 1\text{cm}$ pieces of Si wafer) were placed into the middle zone of the quartz tube reactor and heated to predefined high temperatures in vacuum with a controlled rate. When the temperature kept stable, the valve for feedstock was opened to introduce acetonitrile/ethanol gas flowing into the reactor, attributing to the vapor pressures of liquids at ambient temperature. The pressure in the reactor was kept at ~ 100 mbar in the N-MWCNT growth phase by the vacuum pump. Immediately after the reaction, the feedstock was shut off and the reactor was evacuated again to the initial base pressure and

then cooled down naturally. As the results, highly-dense and vertically aligned CNT arrays with varying N concentration grew from the catalyst layer and covered the entire surface of catalyst-coated Si wafer ($1\text{cm} \times 1\text{cm}$), which could be directly contact-transferred to various substrates for characterization or further application in chemical sensors without the need of purifying.

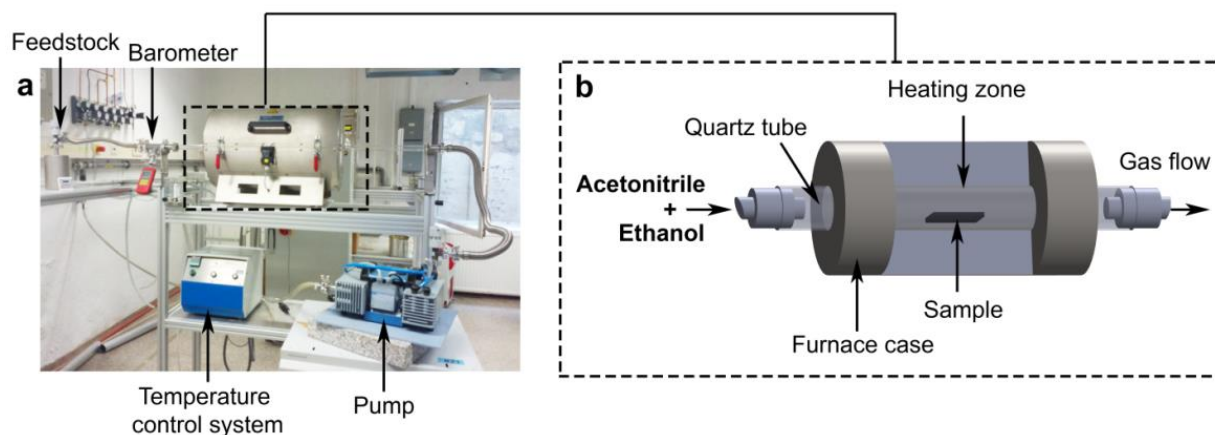


Fig. 2.1: Photographs (a) and schematic diagram (b) of CVD setup for the synthesis of N-MWCNTs.

2.2. CNTs transfer process

After CVD process, the as-grown vertically aligned N-MWCNT samples were transferred onto the surface of various rigid and flexible target substrates, including Si/SiO₂ wafer, glass, quartz and Kapton® polyimide film. P-type Si <100> wafer with a 400 nm-thick oxide layer was purchased from Siebert Wafer GmbH. Glass and quartz substrate with a thickness of 1 mm were obtained from QSIL GmbH, and 100 μm-thick Kapton® polyimide foils were purchased from DuPont.

2.2.1. Cleaning

Cleaning of substrates was always carried out directly before CNT transfer. The target substrate was first cut into small pieces with a size of 1.0×2.0 or 2.0×2.0 cm according to the required sizes of devices, and then cleaned with an ultrasonic washer in an acetone, ethanol and deionized water bath successively for 10 min to carry away dirt particles and contaminants followed by drying with N₂ flow. Additionally, the growth substrate with vertically aligned MWCNTs was only blow-cleaned with nitrogen gun without any chemical treatment.

2.2.2. Surface modify

Before printing, the surface of Si/SiO₂ substrate was chemically modified with octadecyltrichlorosilane (C₁₈H₃₇SiCl₃, ODTS) for the formation of a self-assembled monolayer on a SiO₂ surface, as shown in Fig. 2.2(a). Cleaned substrate was dip-coated into 0.1-1.0% ODTS solution for 2 min to allow the ODTS to uniformly self-assemble on the sample surfaces. Finally, the samples were rinsed with chloroform (CHCl₃) and then dried in air. Chloroform and octadecyltrichlorosilane were obtained from Sigma Aldrich.

2.2.3. Contact printing

The general steps and schematic of direct contact-printing are illustrated in Fig. 2.2(b). The growth (donor) substrate after blowing with N₂ gun was directly pressed onto the surface of cleaned target substrate for more than 30 seconds (step 2 in Fig. 2.2(b)), at the meanwhile, an external pressure generally ranged from 0.5 to 3.0 kPa was applied for keeping an intimate contact at the interface between those two substrates; subsequently, the growth substrate slightly slid along a defined direction with a certain length (< 1 mm) (step 3 in Fig. 2.2(b)); after that, the growth substrate was slightly released and MWCNTs were eventually detached from the growth substrates and anchored on the surface of the target substrates due to the van der Waals interactions (step 4 in Fig. 2.2(b)).

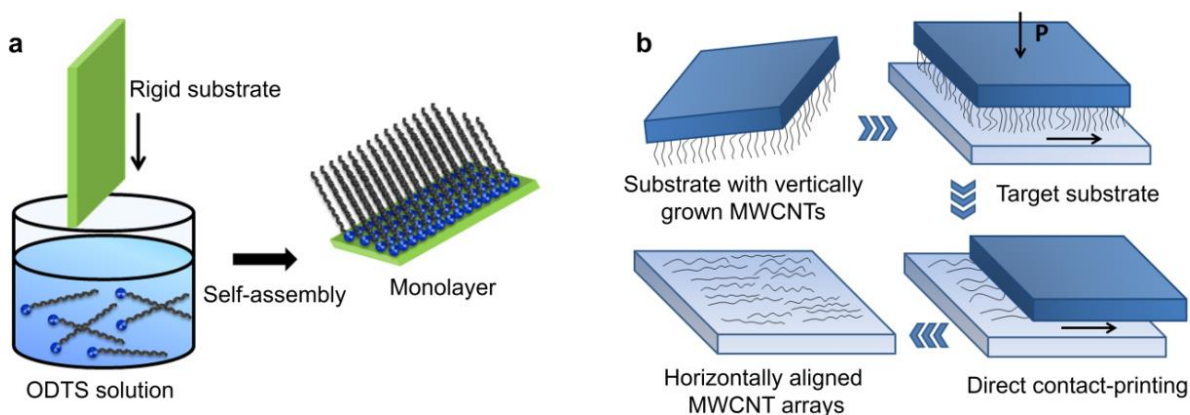


Fig. 2.2: (a) Schematic representation of ODTS modification of a Si/SiO₂ substrate, ODTS molecules are densely packed on the surface of substrate. (b) Schematic of the direct contact-printing transfer process of CVD-grown vertically aligned MWCNTs. (P, pressure).

In this way, the resulting CNTs arrays are oriented horizontally along the overall direction of electron transport between electrodes which will be deposited afterward. The complete transfer process was operated readily at room temperature in open air, and the whole process was performed in 2 min.

2.3. Device fabrication

As shown in Fig. 2.3, two types of sensing devices with different metal electrode patterns were applied in this study, the single device on the chip is prepared for gas sensing (Fig.2.3(a)), and the device matrix shown in Fig.2.3(b) is used for biosensing experiments.

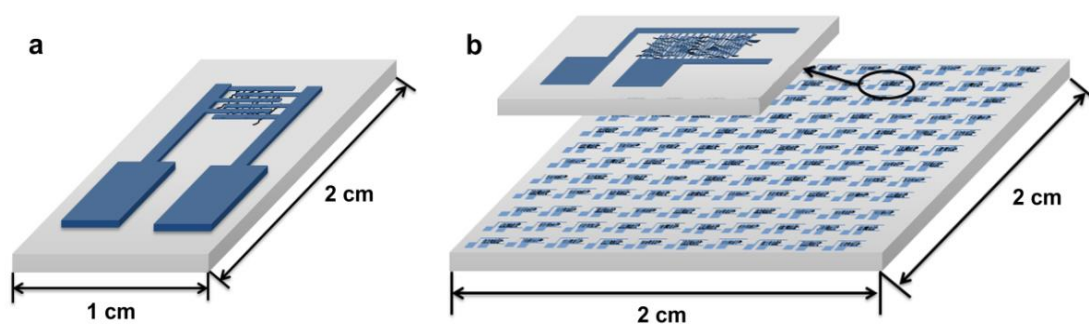


Fig. 2.3: Schematic view of the chemiresistor-type devices in this study: (a) a single gas sensor, (b) biosensor matrix. Cr/Au electrodes were patterned on the surface of substrate with pre-patterned horizontally aligned MWCNT arrays at certain areas.

The chemiresistor-type sensing devices were fabricated using a standard microfabrication procedure. After forming of horizontally aligned N-MWCNTs arrays on the target substrates, Cr/Au (3 nm Cr and 50 nm Au) interdigitated electrode fingers with interspacing of 3 μm were deposited by means of thermal evaporation onto the patterned photoresist mold, and a lift-off technique was used to remove the photoresist. The detailed fabrication process is described as follows.

2.3.1. Photolithography

The flowchart in Fig. 2.4 presents the detailed steps of optical lithography to fabricate interdigitated electrode patterns on rigid and flexible substrates. After direct contact-printing, the substrate was covered with horizontally aligned CNTs at a well-defined position.

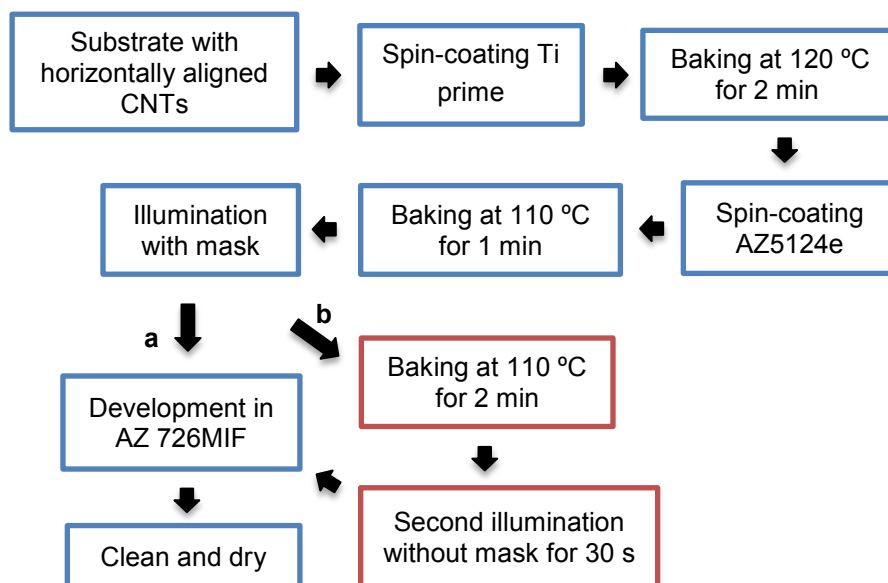


Fig. 2.4: Flow charts of the photolithography to fabricate interdigitated electrode patterns on substrate with horizontally aligned CNTs using (a) positive and (b) negative resists.

Firstly, the substrate was spin-coated a thin layer of TI prime, followed by instantly baking the sample at 120 °C for 2 min. TI prime is a kind of adhesion promoter that can improve the resist adhesion on various substrates including Si and glass. And then, the whole surface of the substrate was covered with photoresist AZ5214e by spin coating, followed by 110 °C baking for 1 min. AZ5214e has the reversal capability only in exposed areas of the resist, which can be activated by heating the sample at the temperature above 110 °C. In this study, AZ5214e was applied as a positive resist for the fabrication of gas sensing devices, while it was reserved and used as a negative resist for fabricating biosensing devices. After coating with photoresist, the samples were illuminated under UV (SÜSS MicroTec) with a mask for 1 second. And then, gas sensing devices can directly undergo development process by immersing the samples in AZ726 MIF for 1 min (see step (a) in Fig. 2.4). However, the biosensing devices need to be baked at 110 °C for 2 min followed by a second illumination without the mask for 30 s to active the reversal capability of the resist (step (b) in Fig. 2.4). Subsequently, the biosensing devices underwent the same development process with gas sensing devices. This is finally followed by rinsing with distilled water for removal of organic contaminants and drying with nitrogen flow.

2.3.2. Thermal evaporation and lift-off process

After photolithography, the well-designed patterns were produced on the substrates. Then, thin metal film (3 nm Cr and 50 nm Au) was deposited by means of thermal evaporation (UNIVEX 300) onto the patterned photoresist mold, as shown in Fig. 2.5. 3-nm Cr was applied to improve the adhesion between gold electrodes and substrate. Afterwards, the samples underwent the lift-off process by immersing in acetone for 15 min and sonication for 1 min to strip the remaining photoresist and unwanted metals. Finally, the electrodes were rinsed with acetone, isopropanol and distilled water thoroughly, and then dried with nitrogen flow. The resultant electrode patterns for gas- and bio-sensing are shown in Fig. 2.3.

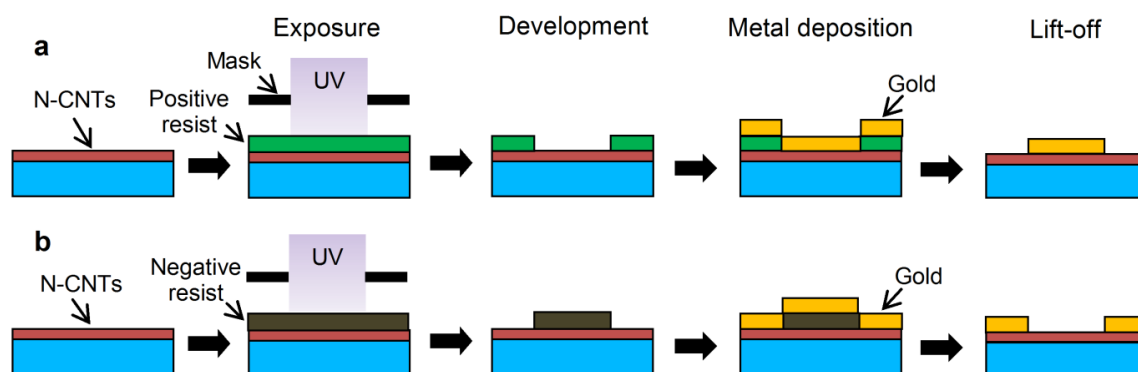


Fig. 2.5: Schematic diagram of the photolithography and metal electrodes deposition process, resist AZ5214e was applied as (a) positive and (b) negative photoresist.

2.3.3. Annealing

All as-fabricated devices were annealed at 200 °C for 15 min in vacuum with the help of my colleagues Dr. V. Khavrus, L. A. Panes-Ruiz and Y. Liu. The annealing process was performed in a CVD furnace, the system was previously heated with a rate of 30 °C/min until 100 °C, followed by a receding heating rate of 5 °C till the temperature is stable at 200 °C. After annealing, the system was cooled down naturally.

2.4. Characterization methods

2.4.1. Scanning electron microscopy (SEM)

Scanning electron microscopy was applied for investigating the morphology of carbon nanotube arrays and interdigitated area of devices, JEOL JSM-6510 and Phillips XL30 ESEM-FEG were applied. Due to a poor electrical conductivity of glass, quartz and Kapton® film, CNTs were not easily observed on these substrates under the SEM. Therefore, low voltage (1-2 kV) was applied for characterization of devices fabricated on non-conducting substrates.

2.4.2. Transmission electron microscopy (TEM)

Transmission electron microscopy (TECNAI F30) performed by Dr. I. Gonzalez was applied to characterize the high-resolution morphology and structure of CNTs. TEM samples were prepared by drop-casting CNT/ethanol dispersion on Cu meshes (S147-3), which were obtained from PLANO GmbH.

High-resolution transmission electron microscopy is an image mode of TEM, which can present structure as small as the unit cell of crystal. HRTEM was applied to observe the atomic structure of carbon nanotubes in this study; we used HRTEM to analyze the diameter, wall-number, defects, closed end as well as catalyst grains of carbon nanotubes.

2.4.3. X-ray photoelectron spectroscopy (XPS)

X-ray photoelectron spectroscopy was performed, which was normally applied to determine the chemical composition of samples. It is widely used for studying the distribution bonding of heteroatom dopants in carbon based nanomaterials. Normally, XPS spectrum contains a primary spectrum, which is a convolution of the final state binding energies of each excited core state as well as a stepped secondary spectrum; therefore, subtraction of the secondary background is very important for analyzing the primary spectrum [109].

To analyze carbon nanotubes, C1s line normally centered at 284.4 is the starting point [109]. When doping with nitrogen atoms into the nanotube lattice, the C1s line will be shifted to higher binding energies with the magnitude 0.1-0.4 eV, [97, 109]. N1s response is very important for identifying distinct components of N-CNTs [109, 110]. In this study, the nitrogen concentration and its bonding configuration of N doped CNTs were characterized with XPS (PHI 5600 spectrometer, equipped with Al monochromatic X-ray at a power of 350 W) performed by Dr. S. Oswald from IFW Dresden.

2.5. Electrical and sensing measurements

The electrical and sensing measurements of the devices were performed with the help of L. A. Panes-Ruiz and V. H. Romay-Lopez.

2.5.1. Electrical characterization

The electrical performances of the gas- and bio-sensing devices were both monitored with a probe station under dry conditions by recording the current vs. voltage (I-V) characteristics. The probe station consists of an optical microscope (Olympus Europe), two micro-positioners with tungsten needles, an electrically contactable sample holder (chuck), and a measuring system Keithley 2604B SourceMeter, as shown in Fig. 2.6(a). The tungsten needles (the inset in Fig. 2.6(a)) were used for applying source-drain (SD) voltages between electrodes of devices and monitoring their relative currents, and the chuck was used for gate voltage and gate current data acquisition.

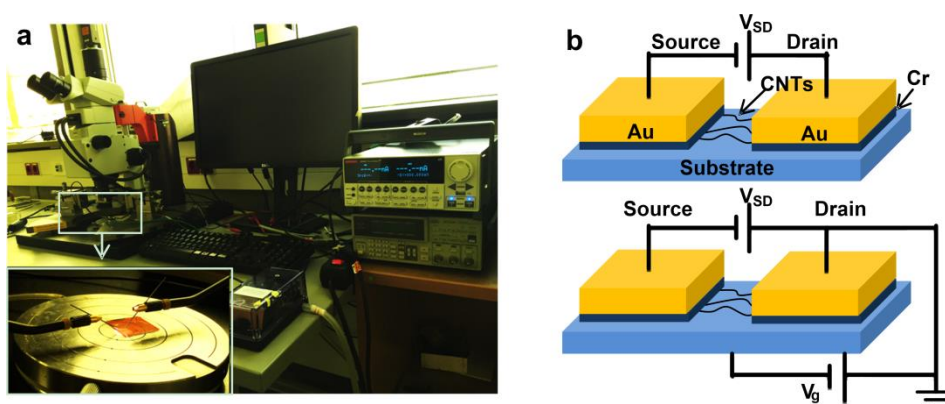


Fig.2.6: (a) An optical photo of probe station for the electrical measurements, the inset is an image of two tungsten needles probing the sensing device. (b) Diagrams for measuring SD I-V curves (top) and transfer characteristics (bottom) of devices.

I-V curves of each device were obtained applying a SD voltage from -2.0 to $+2.0$ V with a fixed back gate voltage V_g of 0 V. All the devices are only used as chemiresistors, but the transfer characteristics (source-to-drain current as a function of the gate voltage) of devices were also investigated to identify current leakage through the back gate (see Fig. 2.6(b)). The transfer characteristics were measured by applying a varying gate voltage from -10 to $+10$ V and keeping a constant SD voltage of 0.5 V.

2.5.2. Biosensing measurement

2.5.2.1. DNA preparation

DNA sequences were purchased from Eurofins Genomics, their base sequences were as follows:

Probe DNA: 5'-CAA ATC TGC ATT GGT TAT CA-3';

Target DNA: 5'-TGA TAA CCA ATG CAG ATT TG-3'.

Before use, the DNA was placed into a thermocycler Mastercycler® Eppendorf probe and heated at 95 °C. Sodium dihydrogen phosphate and disodium hydrogen phosphate purchased from Roth were applied to prepare the phosphate buffer (PB buffer). Afterwards, the probe and target DNA was diluted with PB buffer to a concentration of 20 µM. Additionally, the target DNA solution was further diluted in PB buffer with a varying concentration, which was 0 pM, 2 pM, 20 pM, 200 pM, 2 nM, 20 nM, 200 nM and 2 µM.

2.5.2.2. Functionalization steps

Only biosensing devices need to be chemically functionalized with DNA sequence before sensing application. The biosensing devices were all electrically characterized in the probe station under dry conditions at room temperature before any functionalization treatment. Furthermore, the electrical characterization was also carried out after each step of functionalization, which will not be stated unless otherwise.

At the first step, 200 mM PB buffer was dropped onto the sensor chip to cover the entire channel of electrodes and incubated for 15 minutes at room temperature, followed by rinsing the entire device with deionized water and drying in vacuum at room temperature for 15 minutes. Subsequently, the I-V curve was monitored to assess the effect of buffer on the electrical performance of the devices.

At the second step, the probe DNA was immobilized on CNT sidewalls, which was performed by drop-casting with 100 µL of DNA probe (20 µM) on the surface of the CNT sensor chip at 60 °C until drying in an oven. Afterwards, the chips were immersed in PB buffer 200 mM, washed thoroughly with deionized water and dried in vacuum for 15 minutes. The following electrical characterization can detect if the probe DNA was immobilized on CNT sidewalls successfully.

The third step aims to block the uncovered sites on the CNT sidewalls that DNA probe did not occupy. The probe-functionalized CNT sensors were incubated in a solution of 0.01 % Triton™ X-100 (Aldrich) dissolved in PB buffer 200 mM for 15 minutes at room temperature. Afterwards,

the chips were rinsed with PB buffer 200 mM, followed by rinsing with deionized water and dried in vacuum for 15 min. And I-V measurement can help to assess the influence of Triton™ X-100 on the electrical properties of devices.

2.5.2.3. DNA sensing

The hybridization reaction was carried out by incubating the as-functionalized sensors with DNA target in PB buffer with a varying concentration in sequence, which was 0 pM, 2 pM, 20 pM, 200 pM, 2 nM, 20 nM, 200 nM and 2 μ M.

The chips were firstly incubated with DNA target solution with a defined concentration for 15 minutes at room temperature, followed by rinsing with PB buffer (200 mM) and deionized water. Subsequently, the chips were dried in vacuum at room temperature for 15 minutes. And then, the devices were characterized electrically in the probes station. After the electrical characterization, the next concentration of DNA target was added to the chips, followed by the same hybridization procedure as mentioned above.

2.5.3. Gas sensing experiment

The gas measurement system was developed by Dr. C. Schmädicke, and the detailed description can be found in her doctoral thesis [111]. As shown in Fig. 2.7, the gas measuring apparatus comprises four subsystems: a gas delivery system to control the gas composition inside the measurement chamber, a gas exposure chamber for a specific attachment of the samples, the read-out electronics to determine the resistivity of the sensors, and a temperature control [111]. In this study, ammonia (NH_3) and nitrogen monoxide (NO) were performed as the analytic gases, and pure N_2 was applied as a carrier gas. All experiments were carried out at room temperature.

Before exposure experiments, the MFC 1 (Fig. 2.7) for the analytic gases was purged with pure N_2 for 20 min to avoid contamination. Then the devices were placed inside the sensing exposure chamber, followed by establishing a constant flow of 2 L/min of N_2 . Meanwhile, a constant voltage of 0.1 V was applied between two electrodes and a relative current signal was monitored per second. After the stable signal was captured, the analytic gas flow was introduced in the exposure chamber. The concentration of analytic gas can be controlled by adjusting the flow rate as well as diluting with pure N_2 .

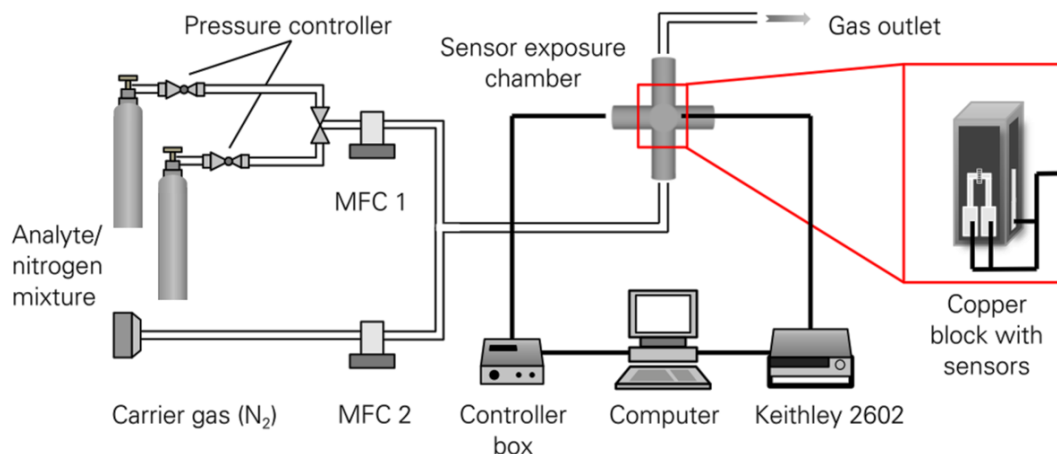


Fig. 2.7: Schematic configuration of the gas measurement system with a small volume gas chamber equipped with read-out electronics for the sensor measurements [111].

A typical cycle of exposure experiment includes three steps: first, a clean N₂ flow was introduced into the sensing exposure chamber as a background; and then analytic gas diluted in N₂ was injected into the chamber and register a sensing signal; finally, a clean N₂ flow was introduced again for sensor recovery [112]. To test one device, multiple exposure cycles were performed under varying concentrations of analytic gas by continuously repeating the same test several times.

3. Synthesis and characterization of vertically aligned N-MWCNT arrays

In this chapter, a review of various preparation techniques of nitrogen doped CNTs will be introduced, and then chemical vapor deposition method was applied to synthesize vertically aligned nitrogen doped carbon nanotube arrays on Si/SiO₂ substrate. The morphology and structure of the N-MWCNTs were examined using SEM and TEM, and XPS were used to assess quantitatively the compositional and structural properties of the N-CNTs. The nitrogen doping level and the types of N substitutes incorporated in the CNTs was tailored in a controlled manner by varying the N-source concentration. Additionally, the influence of catalyst, reaction time and temperature on the chemical surface properties and morphology of N-CNTs were also studied and discussed.

3.1. Overview of synthesis method

Inserting a heteroatom into the backbone of a carbon nanotube, the symmetry of the nanotube is modified and the structure and properties are altered [101, 113]. Stephen et al. [114] firstly reported the incorporation of nitrogen and boron atoms into CNT matrix by means of arc-discharge procedures. Since then, the synthesis of N-CNTs has been extensively investigated over the last decade [99]. There are two main approaches commonly employed for doping nitrogen into CNTs, including “in situ” doping and post-treatment. The “in situ” doping involves the direct incorporation of N heteroatoms into CNT matrix during the synthesis process, and the post treatment is post-synthesis doping of an “as-synthesized” carbon material with a nitrogen source.

3.1.1. “In situ” doping method

Several typical “in situ” doping techniques can be employed to synthesize nitrogen-doped carbon nanotubes, which are similar to those used to synthesize pure carbon nanotubes: (i) high-temperature synthesis methods like arc-discharge [115-117]; (ii) low-temperature synthesis methods such as chemical vapor deposition (CVD) [101, 118, 119].

3.1.1.1. Arc-discharge

Stephan et al. [114] firstly synthesized nitrogen containing multiwall CNTs by means of arc-discharge in 1994. In 2004, Glerup [116] directly synthesized N-CNTs through arc-discharge method using nitrogen-rich organic and inorganic precursors. In their experiments, nitrogen-rich precursor melamine was introduced in the anode rods and the doping levels of N-SWCNTs

bundles could reach up to 1at%. The advantage of arc-charge method is that extremely high temperature would lead to highly crystalline nanostructures with very little disorder. [114] However, the main disadvantage of this method is relatively little control over the alignment of the nanotubes [37].

3.1.1.2. Chemical vapor deposition

CVD is the most common and straightforward approach used to synthesize N-CNTs. In 1997 Yudasaka [120] first reported N-MWCNTs synthesized by CVD using Ni phthalocyanine as a precursor. Since then, a wide range of N-containing precursors have been used to incorporate N atoms into C matrix with success, including acetonitrile, ethylene diamine, dimethylformamide, imidazole, Fe-phthalocyanine, benzylamine, etc. [96, 121-125]

Up to now, different kinds of CVD methods have been developed for synthesis of N-CNTs, such as catalytic CVD, plasma-enhance CVD (PECVD), aerosol-assisted CVD (AACVD), oxygen-assisted CVD, etc. Catalytic CVD is a standard growth method for vertical or parallel N-CNT arrays, Mo [126] synthesized aligned N-CNT arrays through chemical vapor deposition using ferrocene as the catalyst precursor. PECVD is a particularly attractive method, because the high-energy plasma environment enables low-temperature growth and high CNT alignment [127]. Lee et al. [127] generated vertically aligned N-CNT arrays with 52 μm length by means of PECVD within 1 min. In AACVD method, the precursors are transported to the substrate by means of a liquid/gas aerosol, AACVD has a higher deposition rate and a lower overall cost than the conventional CVD method, which also offers better capability and flexibility for the fabrication of multicomponent compounds [128]. Koós [118] reported the production of nitrogen-doped SWCNTs using AACVD. For the purpose of removal of undesired amorphous carbon contamination, oxygen-assisted CVD approaches were developed. Oxygen-containing compounds like water (H_2O) [129], ethanol (CH_3OH) [130], O_2 [131] and carbon monoxide (CO) [132] have been introduced into the precursors, which would improve the catalysts activity, inhibit undesired contamination by amorphous carbon, and promote highly efficient CNT growth.

Compared with arc-discharge methods, CVD is a simple and low-cost technique for synthesizing carbon nanotubes at a lower temperature and ambient pressure [133]. CVD-grown CNTs process inferior crystallinity compared with arc- and laser-grown CNTs, but it would offer higher yield and purity [133]. Besides, CVD methods are versatile that allows CNTs growth in various forms (powder or film, aligned or entangled, straight or coiled), which also offer better control of growth parameters, such as time, temperature, gas flow rate, etc. [133] Through adjusting the synthesis parameters like combination of precursors, pyrolysis temperatures, CVD enable to

control the nitrogen content and binding type [96, 101, 122, 134], that was in particular utilized in current work.

However, most of the CVD synthesized N doped CNTs are multi-walled with a typical bamboo-like morphology and relatively large diameters [134]. Nitrogen doping of SWCNTs is relatively difficult and only recently some groups have reported to succeed in CVD procedure. Ibrahim et al. [134] synthesized N-SWCNTs in 2010 with a nitrogen content up to 2 at% via CVD at 950 °C, using different ratios of acetonitrile/ethanol as a feedstock. Koós et al. [118] reported N-SWCNTs with a nitrogen content of ca. 1 at% which were synthesized in 2012 by using ethanol/benzylamine as N/C source via AACVD between 950 and 1100 °C.

3.1.2. Post treatment method

N-CNTs have also been prepared by various post-synthesis methods including thermal treatment [135], low energy N_2^+ ion implantation [92], and N_2 plasma treatment [136].

3.1.2.1. Thermal treatment

Nagaiah et.al [135] reported N-CNTs with a N content from 2.9 to 6% was prepared through thermal treatment. In their experiments, CNTs were first thermally treated at 800 °C to remove impurities, and then oxidized via a HNO_3 vapor treatment at 200 °C for 48 h to introduce a large amount of oxygen species on the CNT surface. In order to introduce N-containing functional groups, the oxidized CNTs were then treated at elevated temperatures under a NH_3 atmosphere.

3.1.2.2. Low energy N_2^+ ion implantation

Xu et al. [92] reported N-MWCNTs with a N doping concentration ranging from 1.5% to 11.3% which were synthesized by 300 eV N_2^+ ion implantation. In the approach, CNTs were exposed to N_2^+ ion beam originating from a cold cathode ion source, followed by thermal annealing. According to their study, the N content increased with the amount of N_2^+ ions sent to the carbon nanotubes, while decreased when the annealing temperature was increased [92].

3.1.2.3. N_2 plasma treatment

Gohel et al. [136] reported N-MWCNTs prepared via exposing the MWCNT film to 10 min of N_2 plasma treatment in a Denton radio frequency magnetron sputtering machine set at 100 W power and 2 mTorr pressure. This approach could introduce N into MWCNTs, but shortened the length of nanotubes as well as reduced the nanotube density.

Table 3.1 lists current nitrogen doping methods and corresponding doping concentration in the structure of CNTs, which demonstrates that “in-situ” and post-synthesis methods both can incorporate N into CNTs. It is apparent that a higher concentration of N doping is still difficult to be achieved, because the presence of nitrogen decreases the yield of CNTs [118] and a high N concentration leads to a significant structural deformation of the nanotubes and hence terminates growth of crystalline CNTs [137].

Among all those methods, “in-situ” methods are more preferable, because which avoid complex post treatment in toxic gas NH_3 at a high temperature (800-1200 °C) [135, 138]. Moreover, high temperature treatment often causes structural degradation and morphological defects of carbon nanotubes, which would further affect electronic properties of nanotubes [139]. However, nitrogen doping of SWCNTs is still relatively difficult for both arc-discharge and CVD methods; therefore, post-treatment is often applied as an alternative for preparing N-SWCNTs.

Table 3.1: The comparison of N-doping methods and N concentration on CNT structures.

Methods	Precursors	Catalyst	N content %	Ref.
Arc-discharge	N_2	-	0–10	[114]
PECVD	CH_4/N_2	Fe	15–17	[140]
PECVD	NH_3	Nanopatterned catalyst array	0–8	[127]
Aerosol CVD	Ethanol/benzylamine	Ferrocene	1	[118]
Aerosol CVD	Acetonitrile/ Tetrahydrofuran	[Fe(III)(acetylacetonate) ₃]	20	[141]
oxygen-assisted CVD	Acetonitrile/ethanol	Ferrocene	2	[134]
CVD	Pyridine/pyrimidine	Ferrocene	1–3	[142]
CVD	$\text{CH}_4/\text{NH}_3/\text{Ar}$ $\text{CH}_4/\text{pyridine}/\text{Ar}$	$\text{Mo}_{0.1}\text{Fe}_{0.9}\text{Mg}_{13}\text{O}$	1	[143]
Thermal treatment	NH_3	-	2.9–6	[135]
Thermal treatment	NH_3	Fe	2–4	[144]
N_2^+ ion implantation	N_2	-	1.5–11.3	[92]
N_2^+ ion implantation	N_2	-	-	[145]
N_2 plasma treatment	N_2	-	-	[136]

Note: -, not mentioned; PECVD, plasma enhancement CVD.

3.2. Results and discussion

In this study, vertically aligned nitrogen doped carbon nanotubes were synthesized by oxygen-assisted chemical vapor deposition on a Si/SiO₂ substrate. Metallic-layer system of Fe/Al₂O₃ layer was applied as a catalyst; the mixture of ethanol/acetonitrile was employed as C/N source. Previous literature reported that N doping concentration inside the N-MWCNT structure can be controlled through varying the amount of N-containing source [97, 134, 146]. In this study, the concentration of acetonitrile was varied from 0 to 100% (20, 30, 50, 100vol%) in ethanol while keeping the total volume of solution constant (100 mL). The detailed synthesis process is presented in chapter 2.

The growth mechanism of carbon nanotubes remains elusive, vapor-liquid-solid (VLS) mechanism is often assumed [147-149]. In the VLS model, gaseous carbon and nitrogen source first decomposes on the surface of the melting nanocatalyst and forms a carbide, and then carbon and nitrogen atoms dissolve in melting catalyst particles and diffuse to its surface, where they aggregate to form a cap, which finally leads to the growth of CNT from the surface of the nanoparticle [149]. So far, there are two general cases of CNT growth, including “tip-growth” and “base-growth” model (Fig. 3.1(a)). In the “tip-growth” model, the catalyst-substrate interaction is weak, when hydrocarbon dissociates on the top surface of the metal particles, carbon diffuses down through the metal, then CNT precipitates out across the metal bottom and pushes the whole metal particle of the substrate [150]. In the “base-growth” model, the catalyst-substrate interaction is strong, CNT precipitation fails to push the metal particle up, leading to precipitation emerging out from the metal’s apex [150]. Terrones [151] proposed a mechanism for the growth of bamboo-shaped N-CNTs, which is also based on the formation of graphitic layers on the catalyst nanoparticle. At the high temperatures used, Fe atoms cluster to form particles, and C and N containing reactants decompose at the meanwhile, the interaction between the Fe clusters and the C/N fragments lead to the formation of the N-MWCNTs [152].

In this study, N-MWCNTs were synthesized with CVD method via decomposing the mixture of acetonitrile/ethanol at high temperature and using Fe/Al₂O₃ metallic-layer as a catalyst. As shown in HRTEM images in Fig. 3.1(b), the morphological structure of the N-MWCNTs was significantly altered through nitrogen doping, leading to the formation of bamboo-like structures. According to a previous report [99, 153, 154], this is because the presence of N atoms in the C/N graphite-like layer lead to stresses in the surface, and this is released by a “pulsed” effect in which the C/N surface layer detaches from the Fe. This process is repeated over and over again leading to the compartmentalized bamboo shape. According to the “pulsed” effect, it can be observed in Fig. 3.1(b) that the wall thickness increases by the joint of the compartment layers, but the outer diameter remains about the same for the entire tube, which is coincident with

previous research reported by Lee [155]. HRTEM image in Fig. 3.1(c) reveals no encapsulated catalytic particles existed in the closed tip of the bamboo-like structure of nanotubes; the tip of nanotubes is typically encapsulated with layers of graphene, indicating our N-MWCNTs is produced by a “base-growth” model.

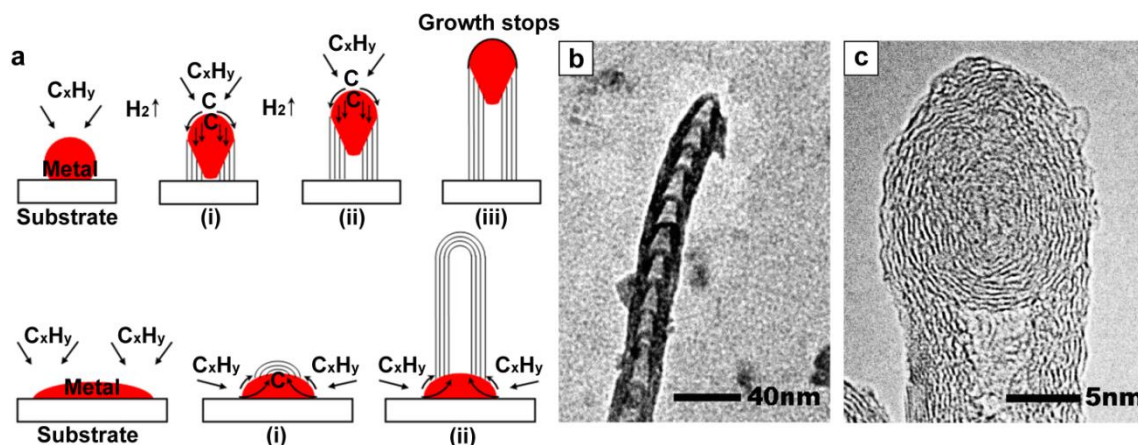


Fig. 3.1: (a) Widely-accepted growth mechanisms for CNTs: (top) tip-growth model, (down) base-growth model [150]. (b) TEM image of a bamboo-like nitrogen doped carbon nanotube. (c) Magnified HRTEM image of the tip of a nanotube.

Although CVD-based growth mechanism has still not been completely understood, plenty of investigations have already indicated that the physicochemical properties of N-MWCNTs can be controlled through CVD method by varying different synthesis parameters, i.e. catalyst, reaction temperature and duration, nitrogen or carbon precursors [152, 156, 157]. Changing even one experimental parameter will lead to a significant influence on the morphology and physicochemical properties of the N-MWCNTs. In further discussion, the growth of highly dense and vertically aligned N-MWCNT arrays was optimized and studied from the aspect of the catalyst-layer thickness, growth rate, temperature as well as varying concentration of N/C source.

3.2.1. Catalyst

Previous studies show that catalysts play a key role in the type of nanotubes produced, such as the number of walls, the diameter, and the graphitization [99, 152, 158]. Catalyst material for CNT synthesis requires strong metal-support interactions, a high surface area and large pore volume at high temperature [158]. There are many types of catalysts that can be used for CNT synthesis, including Fe, Ni, Co, Zn and Cu [152, 159], but the most frequently used are Fe, Ni

and Co, because of obtaining higher yields of both doped and undoped CNTs [160, 161]. However, normally supported catalysts used for CNTs growth are too small to characterize by microscopy, leading to difficulties in controlling the size of the catalytic nanoparticles [45].

Herein, we used Fe/Al₂O₃ metallic-layer system with ultrathin Fe film as a supported catalyst to synthesize N-MWCNTs, the thickness of Fe film (0.5, 1 and 2 nm) can be accurately controlled through magnetron sputter deposition [162, 163]. The results were shown in Fig. 3.2. Fig. 3.2(a,b) demonstrate that nanotubes can be synthesized from 0.5 and 1 nm-Fe layer. Moreover, it is apparent that the surface density and yield of N-MWCNTs grown from 1.0 nm-Fe layer (Fig. 3.2(b)) were significantly increased compared with that from 0.5 nm (Fig. 3.2(a)). The inset in Fig. 3.2(b) presents a morphology of excellent vertical alignment of the N-CNT bundles in arrays, high-dense N-MWCNT arrays tightly stick together side by side due to van der Waals forces, indicating a better catalytic behavior of 1.0 nm Fe layer. In Fig. 3.2(c), 2 nm-Fe film aggregated into large deactivated particles and no nanotube precipitated out across the Fe particles, indicating no catalytic effect of 2 nm-Fe film. As shown in Fig. 3.2(c), the particles present relatively larger diameter compared to the nanotubes in Fig. 3.2(a,b), which may attribute to tightly warped amorphous carbon on the surface of metal particles. It also can be seen that no amorphous carbon and contaminates existed in those SEM images, revealing that changing the thickness of Fe layer did not have a significant influence on the purity of the sample.

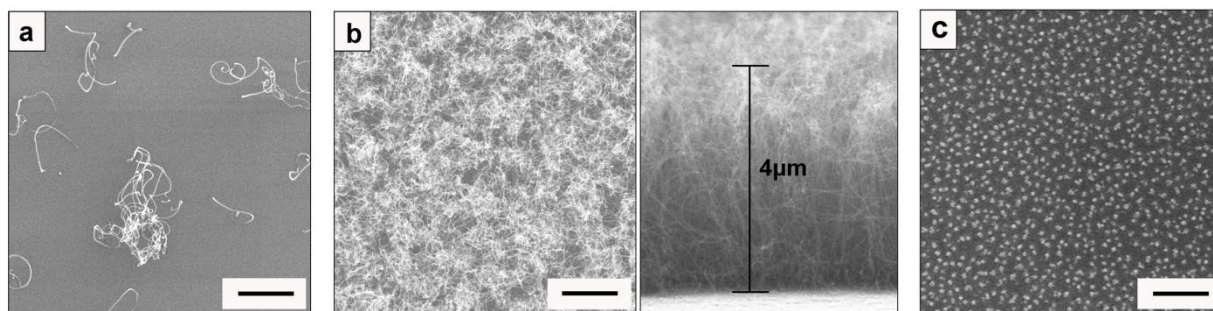


Fig. 3.2: SEM images of N-CNTs grown from (a) 0.5, (b) 1.0, and (c) 2.0 nm Fe multilayer system. (d) The comparison of diameter and length of the N-MWCNTs grown from 0.5 and 1.0 nm Fe multilayer system. (Data bar: 1 μm, precursor: pure acetonitrile, reaction temperature: 885 °C.)

The result indicates that the yield and density of nanotubes were very sensitive to the variation of Fe-layer thickness. This phenomenon can be explained by the CNT growth mechanism. During

the temperature rise, the sputtered Fe layer was gradually separating and agglomerating to form separated nanosized Fe particles under the effect of Fe/SiO₂ interface energy. These Fe particles acted as catalysts in the subsequent N-NWCNT growth. Therefore, the size and density of the Fe particles remarkably influenced the morphology and density of the synthesized N-MWCNT. The 0.5 nm Fe-layer cannot form uniform and dense distributed nanoparticles; as a result, low density and curly N-MWCNT grew under this condition. 1.0 nm Fe-layer reflected higher catalytic efficiency for N-MWCNT, which was selected for the optimization of the N-doped vertically-aligned MWCNT arrays unless otherwise specified.

3.2.2. Growth rate and duration

CNT growth rate is one of the central issues for CNT synthesis, which are necessarily required to achieve highly efficient synthesis. According to Geohegan et al. [164], average growth rates reported for vertically aligned arrays of multiwall carbon nanotubes synthesized via CVD range from 0.4 to 50 $\mu\text{m}/\text{min}$, with lengths typically terminating around 50-200 μm . Because CNT growth is a very complex process, the growth rate of CNTs is related to many parameters, like catalyst lifetime, carbon feedstock, reaction temperature, etc. [165]

To investigate the growth rate and reaction duration, vertically aligned N-MWCNTs arrays were all synthesized by decomposing pure acetonitrile at the same temperature with a single variable of reaction duration, which was varied from 1 to 15 min. The SEM images in Fig. 3.3 present the morphology of the as-synthesized N-MWCNTs from the top and side view (insets).

In the first image of Fig. 3.3(a), nothing could be observed on the substrate surface, indicating carbon nanotubes didn't start to grow in the initial 1 min. During this period, Fe atoms may have already clustered to particles, but this could not be seen under SEM due to extremely small size. The next SEM image shows that deactivated catalyst particles with a large diameter and a few randomly-distributed nanotubes were formed as the reaction duration extending to 3 min. This demonstrates that hydrocarbon had decomposed and diffused through the metal particles, but the CNT precipitation didn't complete in 3 min, leading to lots of large-sized deactivated catalyst particles.

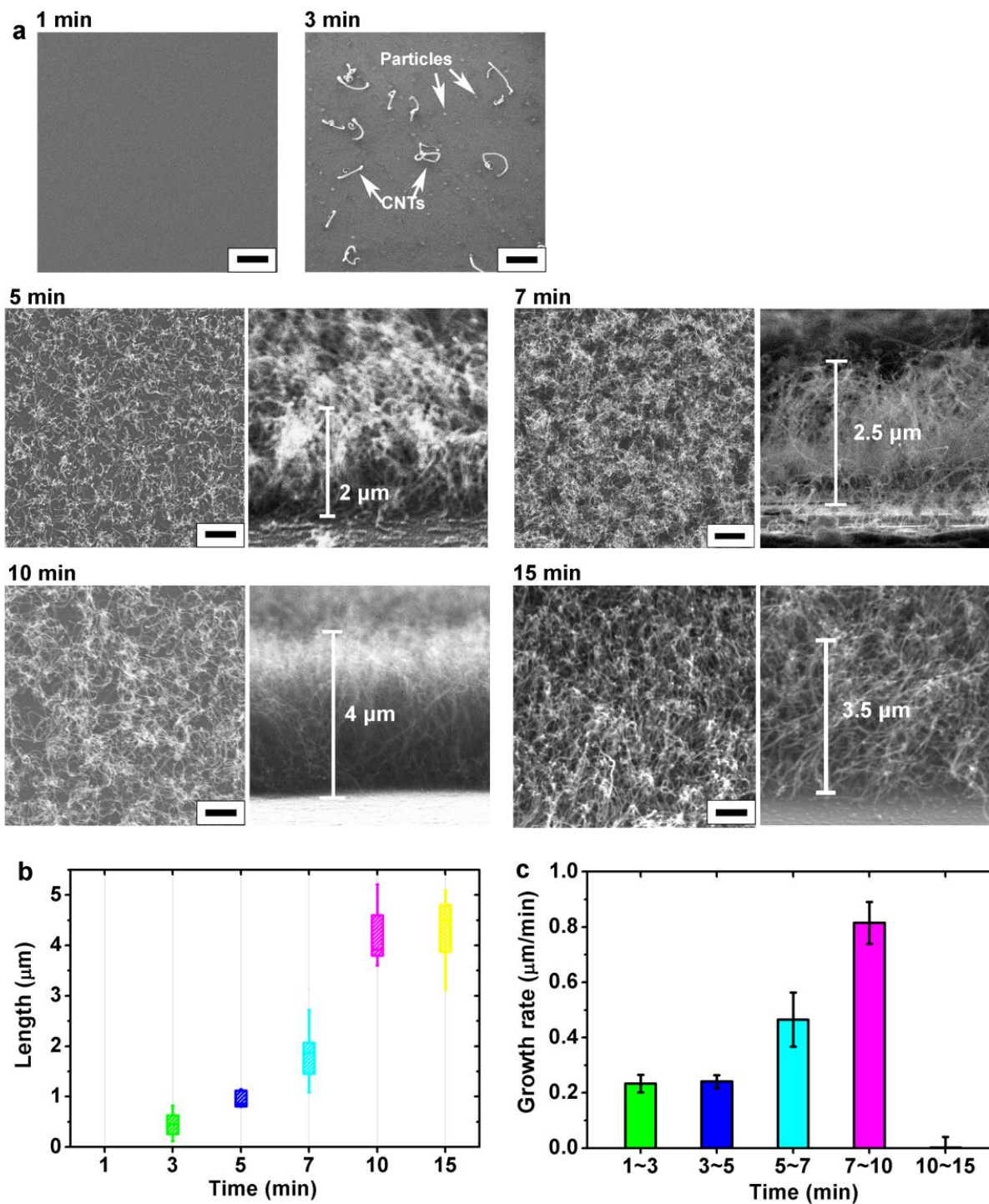


Fig. 3.3: (a) SEM micrograph of the N-MWCNTs grown via CVD with duration of: 1, 3, 5, 7, 10 and 15 min. The (b) length and (c) growth rate of N-MWCNTs plotted as a function of reaction duration ranging from 0 to 15 min.

Vertically aligned N-MWCNT arrays began to grow after the reaction duration extended up to 5 min, and the length of CNT arrays increased with time. Fig. 3.3(b) shows the mean length of N-CNTs increased from 0.5 to 4.3 μm , when the reaction duration was prolonged from 3 to 10 min. As shown in Fig. 3.3(c), the growth rate of nanotubes also presented an upward trend during this period, and which reached the highest point of $\sim 0.8 \mu\text{m}/\text{min}$ during 7-10 min. However, the nanotubes stop growing after reaction lasting for 10 min, indicating a relative short catalyst lifetime. This is a common problem for CNT growth named catalyst poisoning, which could occur by encapsulating catalyst particles with amorphous carbon which blocks access of the growth species to the catalyst surface [166].

Although the catalytic mechanism remains elusive, many previous publications have reported on prolonging the catalyst lifetime. Hata et al. [129] reported that a small content of water vapor could significantly prolong the catalyst lifetime in their water-assisted ethylene based CVD. Zhong et al. [166] developed a sandwich-like $\text{Al}_2\text{O}_3/\text{Fe}/\text{Al}_2\text{O}_3$ catalyst system for the growth of 0.5 cm SWCNTs at a growth rate of $\sim 2.6 \mu\text{m}/\text{min}$ for 32 h growth time. Bronikowski et al. [167] reported that CNTs can be grown for a longer time at lower temperatures, and they synthesized MWCNTs at 600 $^\circ\text{C}$ with a growth rate of $\sim 0.64 \mu\text{m}/\text{min}$ for 26 h. In this study, 4 μm -CNT arrays are already long enough for the fabrication of CNT based nanodevices, which are applied for bridging the interdigitated electrodes. In this case, there is no need to prolong the catalyst lifetime, and the reaction duration is kept at 10 min in the further study.

One thing we need to point is that the length of CNT arrays we measured here is not the real length of nanotubes, because defective nitrogen doped multiwalled nanotubes are much curlier than pristine CNTs. Therefore, we only calculated and discussed approximate lengths of vertical nanotube bundles in this study.

3.2.3. Precursor composition and growth temperature

Since the physicochemical properties of N-CNTs are significantly dependent on the level and type of doping nitrogen, a controlled way of inserting N into the structure of CNT during synthesis is desired [168]. The nitrogen content in N-CNTs mainly depends on the solubility of nitrogen in the catalyst nanoparticle during synthesis and the proportion of the nitrogen-containing compound in the reaction mixture [104, 134, 169, 170]. Some works have already shown that the percentage of nitrogen substitute in N-CNTs can be varied by changing the synthesis temperature [152, 156]. Recently, the type and concentration of feedstock were evaluated to affect nitrogen incorporation in CNT structure [171]. A varying proportion of the N-containing compound has been employed to control the N doping content in N-CNTs [122], which was also capable to adjust the length and diameter of the bamboo shaped nanotubes. Koós et al. [172] synthesized N-CNTs by using the mixture of benzylamine and toluene, the length and

diameter of the nanotubes decrease with nitrogen concentration while bamboo-shaped nanotubes increases. Ayala et al. [146] reported that single and multiwalled N-CNTs can be selectively grown by modulating the concentration of acetonitrile in ethanol solution. While the influence of reaction atmosphere composition on the morphology of the nanotube has been investigated [146], the effect on the N doping concentration as well as the forms of N incorporation in N-CNTs structure has not been clarified.

Herein, we report a systematic study of N-MWCNTs synthesized with a wide range of varying concentration of N containing reactant acetonitrile (20-100 vol%) in ethanol to evaluate the effect of the concentration of N source on the structure, N-doping concentration and N incorporation types of N-MWCNTs. Ethanol was applied as carbon source to dilute acetonitrile, because (i) they are both common feedstocks employed for N-doped CNT synthesis; (ii) ethanol contains oxygen in its chemical structure, which improves the catalysts activity and inhibits undesired contamination by amorphous carbon; (iii) they have similar molecular weight; (iv) most especially these two solvents have close values of vapor pressure (as shown in Fig. 3.4(a) and appendix A), that they achieve a relatively close mean evaporation saturation at ambient temperatures [146].

It is well known that reaction temperature plays an important role in the growth of carbon nanotubes. We tested the growth of N-MWCNTs in the range of 700-940 °C, because the optimal reaction temperature is closely related to the ratio of acetonitrile/ethanol in the solution. There was no N-CNT formation observed at the reaction temperature below 720 °C. Analyzing the morphological characteristics of the resulting materials synthesized in a pure acetonitrile reaction atmosphere, it was found that well-aligned N-MWCNT arrays were always formed around 860 °C, which is consistent with the result reported by Ayala [146], who synthesized N-MWCNTs by decomposing pure acetonitrile from 750 to 900 °C.

To control the N doping concentration in N-MWCNTs, different proportions of carbon source ethanol was added to dilute N source acetonitrile. In this study, the relative percentage of acetonitrile in precursors is 100, 50, 30, 20vol%, as listed in Table 3.2. As introducing ethanol into acetonitrile as feedstocks, the synthesis temperature of nanotubes increased by 60 °C, approximately. Therefore, the synthesis temperature of carbon nanotubes from pure acetonitrile is of 840 °C, while that of nanotubes grown from acetonitrile/ethanol compound is of 900 °C.

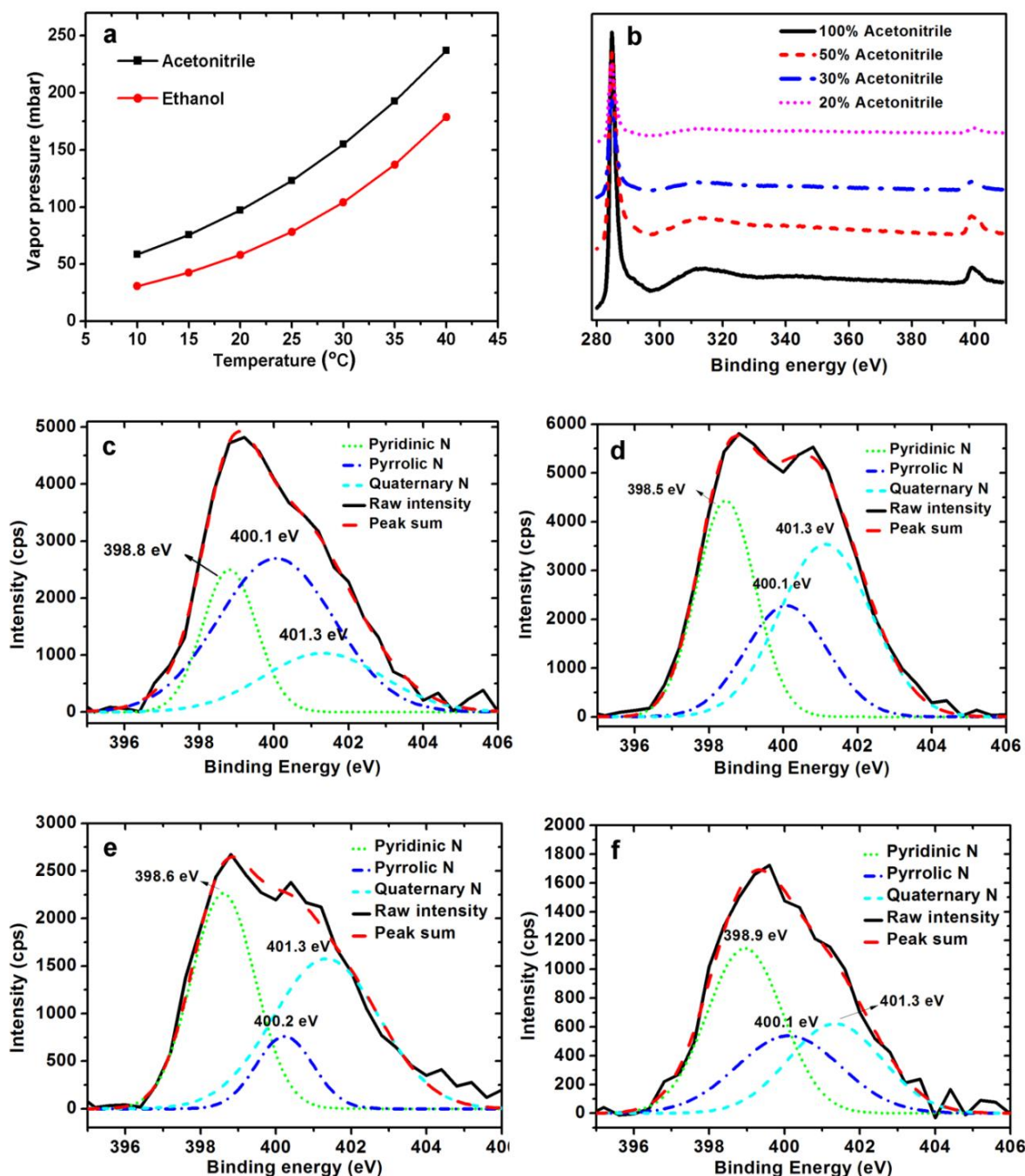


Fig. 3.4: (a) Vapor pressure of acetonitrile and ethanol at ambient temperatures, which was calculated through Antoine equation as shown in appendix A. (b) XPS C1s and N1s spectra of N-CNTs synthesized by using varying concentrations of acetonitrile in ethanol as feedstocks. N1s spectra showing different types of nitrogen incorporated in N-MWCNTs synthesized from (c) 100, (d) 50, (e) 30, and (f) 20vol% acetonitrile in ethanol.

XPS measurements were carried out to estimate the doping nitrogen content and bonding situation in the structure of nanotubes. Fig. 3.4(b) exhibits predominant narrow graphitic C1s peaks at ~284.8 eV along with the N1s peaks between 398.8 and 400.8 eV of four samples prepared with different N-containing feedstocks concentration. The total concentration of nitrogen atoms on the surface of carbon nanotubes was estimated XPS, which varied from 5.0 to 8.3%.

Table 3.2: Element concentration and concentration of pyridinic, quaternary and pyrrolic N (at%) in N-MWCNTs synthesized with 20%, 30%, 50% and 100% acetonitrile fraction.

CH₃CN	20%	30%	50%	100%
Total C	89.8	89.4	88.7	90.1
Total O	4.7	3.3	3.6	4.8
Total N	5.5	7.3	8.3	5.0
<i>Pyridinic N</i>	2.4	3	2.8	1.2
<i>Quaternary N</i>	1.6	3.5	3.5	1.1
<i>Pyrrolic N</i>	1.5	0.9	2.0	2.8
N/C ratio	6.1	8.2	9.3	5.6

The dependence of the nitrogen content in CNTs on the percentage of acetonitrile is presented in Table 3.2. It can be observed that the change in the N-doping content is associated directly with the proportion of N source acetonitrile in the feedstock. The total nitrogen content in nanotubes increases with the growth of acetonitrile concentration in the feedstock from 20% to 50%. Adding 50% acetonitrile dopes 8.3% of nitrogen into the carbon nanotubes. Acetonitrile contains *ca.* 34% nitrogen, higher amount of which in the feedstock should theoretically lead to higher N doping content, but the N content of N-CNT synthesized from pure acetonitrile show a lower concentration of N incorporation in practice, this may be explained that N incorporating in carbon nanotubes may be not favored at lower temperatures. A similar result was reported by Bepete et al. [171], that N doping concentration of N-CNTs produced by CVD was 0.36% at 850 °C and which increased to 0.49% at 900 °C.

The XPS N 1s spectra 398.8 and 400.8 eV of samples can be interpreted as pyridinic, pyrrolic and graphitic nitrogen, as spectra of samples produced from decreasing percentage of acetonitrile shown in Fig. 3.4. The dominated peak located at 398.5 corresponds to pyridinic nitrogen, and the peaks at 400.1 and 401.4 eV are attributed to the pyrrolic and quaternary nitrogen, respectively. The concentration of various types of nitrogen sites in carbon nanotube structures

was determined by integrating corresponding XPS peaks, and the results are listed in Table 3.2. It is found that the concentrations of various nitrogen sites are increased with the total amount of N doping in nanotube structure. The concentration of quaternary nitrogen shows a more apparent growth compared with that of pyridinic and especially pyrrolic nitrogen. Chizari et al. [152] reported that the Fe catalyst led to the formation of N-CNTs with a higher amount of quaternary nitrogen compared with Co, Ni or Cu catalysts. However, the sample produced from pure acetonitrile presents an apparent high value of pyrrolic nitrogen (2.8at%), which may be explained that lower temperature is more effective for the formation of pyrrolic N. This trend is in accordance with the result by Sharifi et al. [27], who performed a similar study but at a lower temperatures, that nitrogen incorporation at high temperatures (800 °C) mainly takes place by pyridinic and quaternary N forms, whereas at a lower temperature (700 °C) the two main defects types are instead pyridinic and pyrrolic. This may be because C atoms at higher temperatures have a higher diffusion rate, leading to the formation of the more stable graphitic nitrogen defect type [27].

It is well known that nitrogen atoms have an effect on the structure of CNT walls, which normally present a compartmentalized bamboo structure [109]. Fig. 3.5 presents the TEM images of N-MWCNTs with varying N-incorporation concentration, which confirmed the formation of bamboo structure in a multiwall nanotube with N doping: the inner part of the nanotube is not hollow but contains bamboo-like compartments. According to Zhang and Nxumalo [99, 173], doping with N leads to more disorder in a CNT through an increase in the number of defects created. Sumpter et al. [174, 175] studied the growth of N-CNTs by means of experiment and density-functional theory (DFT) calculations; they found the curvature of N-CNTs can be largely affected while nitrogen atoms stabilizing neighboring pentagons in the CNT. The distribution of diameter, sidewall-number, and compartment distance were calculated from HRTEM images in Fig. 3.5 and presented in Fig. 3.6.

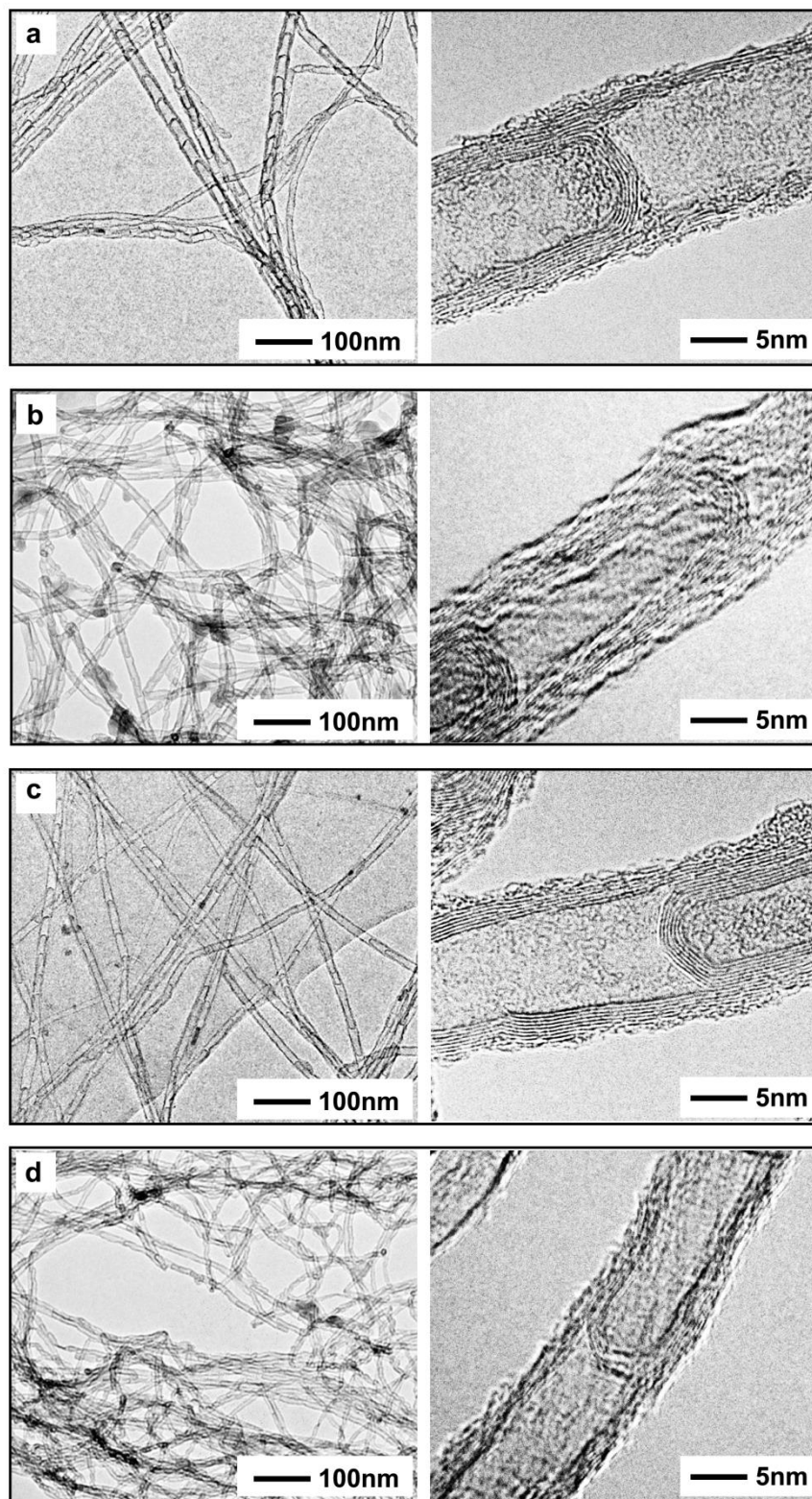


Fig. 3.5: Low- (left) and high-magnification (right) TEM images showing bamboo-like N-MWCNTs with N doping concentration of (a) 8.3, (b) 7.3, (c) 5.5 and (d) 5.0at%.

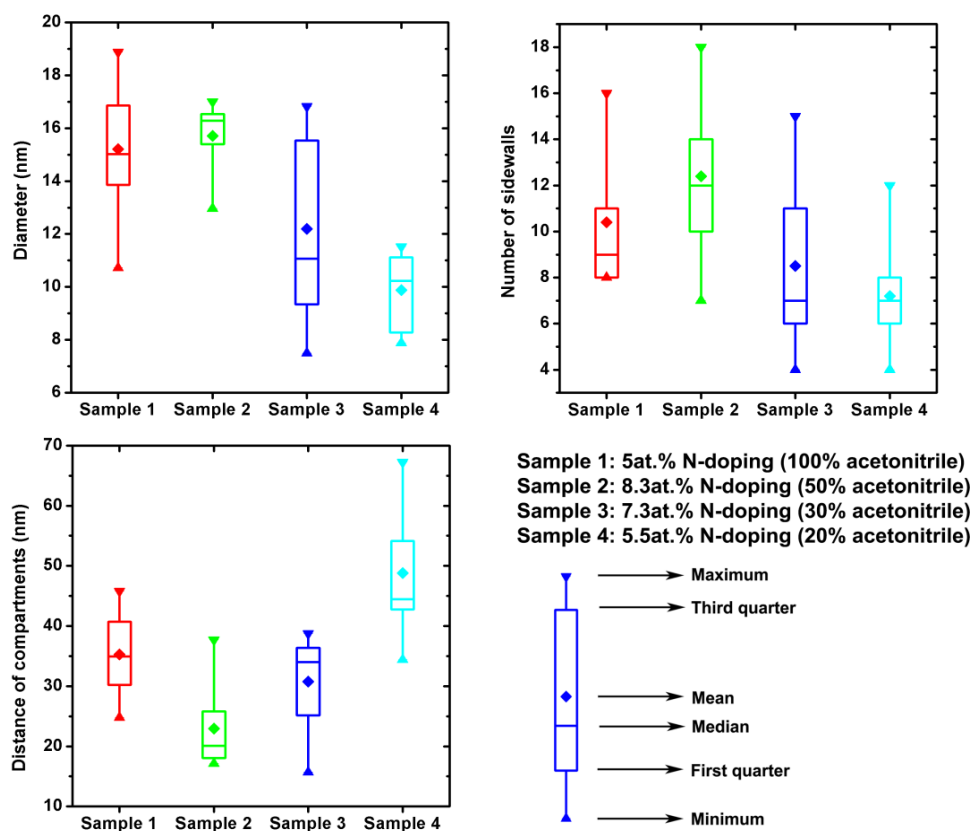


Fig. 3.6: Statistic distribution of (a) diameter, (b) number of sidewalls and (c) distance of bamboo-like compartments of CVD-grown nitrogen doped multiwalled MWCNTs with a varying N concentration from 5 to 8.3%. The growth temperature of sample 1 is 850 °C, while that of sample 2-4 is 900 °C.

As shown in Fig. 3.6(a), both mean diameter and diameter distribution of N-CNTs grown at the same temperature decrease with the increasing of N concentration. The mean diameter of nanotubes with a higher N concentration (8.3%) is 15.7 nm, which decreased to 9.9 nm as the N-doping concentration dropping to 5.5%. According to the statistics in Fig. 3.6(b), the number of outer walls in N-CNTs also decreased with N incorporation. A similar result was reported by Nxumalo et al. [101], they observed that the increase in the concentration of nitrogen containing hydrocarbons during the synthesis of N-MWCNTs results in an increase in the average outer diameter. However, carbon nanotubes with a lower N concentration of 5% grown from pure acetonitrile but still present a larger diameter. This difference may attribute to its lower growth temperature (60 °C) compared with other samples. According to Aksak et al. [176], they also observed the average diameter of the CVD-grown carbon nanotubes decreased continually from 20.4 nm to 10.5 nm as increasing the growth temperature from 850 to 925 °C. As mentioned

before, N incorporation in nanotube lattice increases defects and unusual polygonal ends of nanotubes, and we confirmed that higher N concentration will bring more disorder and bamboo-like compartments inside N-CNTs. The distance between bamboo-like compartments was calculated from TEM images, which continuously increased from 23.0 to 48.8 nm as the doping concentration decreased (see in Fig. 3.5(c)), a similar trend is also reported by Nxumalo [101].

Based on extensive characterization (SEM, TEM, and XPS) of our as-grown N-doped CNTs, the results of synthesis of N-MWCNTs can be summarized as follows:

- (i) The N-CNTs are multiwalled; the diameter of nanotubes ranges between 7 and 19 nm depending on the growth temperature as well as the content of N incorporation in the N-CNTs structure.
- (ii) Grown N-MWCNTs are vertically aligned, the length of the N-MWCNTs is increased with the reaction duration, and the CNTs stop to grow after 10 min with the mean array length of $\sim 4 \mu\text{m}$.
- (iii) The TEM images reveal that the N-MWCNTs are not all straight, because of nitrogen atoms stabilizing neighboring pentagons in the CNT.
- (iv) XPS measurements present the N-doping concentration of N-CNTs varied from 5 to 8.3at%, and the dominant N incorporation forms are quaternary and pyridinic N.
- (v) SEM and TEM images also show the CVD-grown carbon nanotubes are quite clean without contaminants of amorphous carbon on their surface.

3.3. Conclusion

Herein, vertically aligned nitrogen-doped carbon nanotubes were synthesized on the Si/SiO₂ substrate via chemical vapor deposition method by using the mixture of acetonitrile/ethanol as the feedstock. TEM observations indicated that the nanotubes are multiwalled and have compartmentalized bamboo structures. The diameter of nanotubes ranges from 7 to 19 nm depending on varying the N-source concentration; the length of the vertical MWCNT arrays is around 4 μm . To improve the yield and length of MWCNT arrays, the thickness of catalyst layer, synthesis duration, and growth temperature were optimized. It was also found that the optimal growth temperature of N-MWCNTs increased while ethanol was introduced into the precursor.

XPS analysis demonstrated the presence of quantifiable amounts of nitrogen in CNT walls. The effect of varying the N-source concentration on the production of N-doped CNTs was studied, the study revealed that the N concentration in the N-MWCNT structure could be varied from 5 to 8.3at%, and the highest N content was achieved by using 1:1 acetonitrile/ethanol as a feedstock. The three forms of N incorporation in CNT matrix (pyridinic, pyrrolic and quaternary) can also

3. Synthesis and characterization of vertically aligned N-MWCNT arrays

be controlled through adjusting N-source concentration, and the dominating N incorporation forms in CNT are pyridinic and quaternary N because of high reaction temperature.

4. Horizontal alignment of CNT on surfaces

Conventional nanomaterials synthesized through high-temperature chemical vapor deposition usually could not be utilized directly for fabricating nanoelectronic devices. A typical approach to fabricate CNTs based electronic devices is first to transfer CNTs onto a target substrate, and then to deposit electrical connections using standard microfabrication technology like photolithography [177]. Therefore, effective transferring nanomaterials onto various target substrates plays an important role in nanodevice fabrication in order to avoid harsh synthesis and fabrication steps, thus greatly reduces the complexity of fabrication and integration of nanomaterials.

In this work, we mainly focus on tackling the challenge of controllably transferring vertically aligned CVD grown MWCNTs onto various substrates through a quite simple and rapid step. The method of “direct contact printing” was applied for a scalable and repeatable transfer and positioning of highly dense and aligned MWCNT arrays onto a wide range of substrates, including flexible sheets. The morphology of those printed parallel MWCNT-arrays has been characterized by means of scanning electron microscopy.

4.1. Overview of CNTs transfer

As mentioned above, most CNT-based devices can be fabricated using transferred CNTs followed by standard microfabrication processes. However, it is still a challenge for practical implementation of scalable and effective CNT transfer [177, 178], owing to small diameters and large van der Waals interactions between CNTs. In recent publications, several approaches, which are generally summed up into wet and dry methods, were reported to transfer CNTs networks or CNTs films onto a target substrate for various applications (Fig. 4.1).

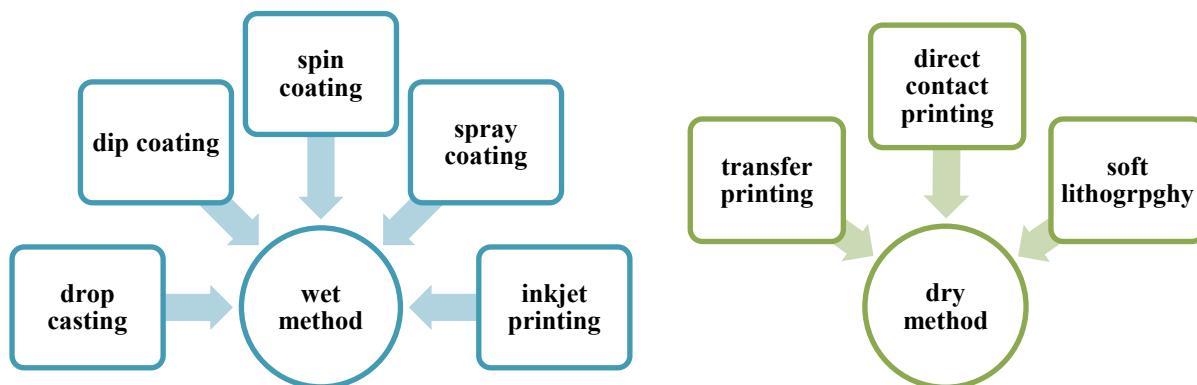


Fig. 4.1: A relationship diagram of wet and dry transfer methods.

4.1.1. Wet methods

The wet methods consist of dispersing CNTs in a liquid and then patterning from the liquid phase [179]. Multiple wet approaches have been used for depositing nanowires or carbon nanotubes in the recent study [179], such as drop casting [180], spin coating [181, 182], spray coating [182, 183], dip coating [179, 181] and inkjet printing [184-186]. The wet method is characterized as an attractive option for simply obtaining randomly networks or thin films of CNTs on various types of substrates, such as flexible and other planar substrates [181-190]. However, there still are a variety of existing problems for transferring and patterning CNTs through a liquid phase. To get into wet methods more deeply, the most common approaches will be introduced in this chapter in detail.

4.1.1.1. Drop casting

Drop casting is one of the most common ways to transfer nanostructures by depositing consecutive drops of their dispersed suspension onto the surface of the target substrate. Drop casting can be applied to transfer various nanostructures, such as SWCNTs, MWCNTs, graphene, and nanowires, etc. This method is quite simple and easy to operate and can be adapted for both rigid and flexible substrates. Pu et al. [180] reported drop-casting graphene on both polyethylene terephthalate and flame retardant woven glass reinforced epoxy resin substrates through a quite easy approach.

During drop casting process, a well-known phenomenon denoted as the “coffee ring” effect was reported by Deegan and co-workers [191, 192], which occurs as a droplet of aqueous colloidal suspension drying on a wettable substrate [186]. This phenomenon also happens when drop-casting CNTs from their suspensions [193]. When CNTs suspension is dropped onto a substrate, suspended CNTs tend to move towards the edge of the droplet during the solvent evaporation, because evaporation rate is the highest at the edge [186]. The “coffee ring” effect causes inhomogeneous deposition of CNTs that a higher density of nanotubes distributes at the edges compared with the center. To limit the “coffee ring” effect, various methods, including heating the substrate and treating the substrate surface, are applied for obtaining a uniform distributed CNTs networks and films, but which is still difficult to be fully avoided [193].

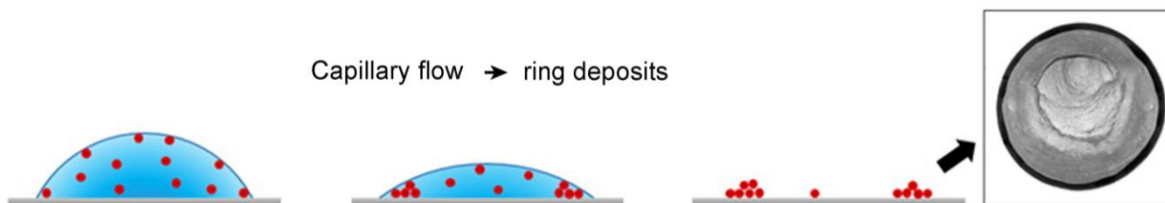


Fig. 4.2: Schematic and brightfield microscope image of the “coffee ring” effect, that deposits formed from evaporating drops containing particles [194].

4.1.1.2. Spray coating

Spray coating is a simple deposition technique for the formation of randomly aligned CNT network or film, which consists of spraying solution of nanomaterials onto various substrates through a nozzle [183]. Spray coating allowed for the rapid production of thin films in large areas on a variety of substrates, even on high topography substrates [178]. Zhang et al. [195] utilized spray coating to deposit CNTs onto carbon fiber prepreps for network formation.

Like drop coating, spray coating also faces the “coffee ring” effects, which could be avoided through heating or adapting the distance between the sample surface and the nozzle [196]. Compared with conventional drop casting, spray coating method can deposit more minute droplets, which require shorter evaporation time, thus leads to the limitation of “coffee ring” effects. Therefore, spray coating has more potential to generate a dense and homogeneous coating of a large area with good quality and reproducibility of the patterns [196].

4.1.1.3. Spin coating

Spin coating is the process of evenly coating a spinning substrate with a solution, which is widely used for photoresist coating in microfabrication and recently have been reported to deposit uniform a thin film of various nanostructures with a nanoscale thickness [181]. Jo et al. [197] reported a dense network of SWCNTs fabricated by spin coating method when oligothiophene-terminated poly(ethylene glycol) was used as a non-ionic and amphiphilic surfactant.

The advantage of spin coating is deposition of very uniform films of nanostructures quickly and easily, besides, the thickness can be determined by spinning speed, acceleration and solidifying condition [181]. However, the use of the spin coating is limited to structures without high topography. Like drop casting, the spin coating also faces the “coffee ring” effect during the

evaporation process, therefore, baking is always applied after spin coating in the area of microfabrication.

4.1.1.4. Dip coating

Dip coating is a simple and popular way of depositing a thin film, through dipping a substrate into a coating solution and then withdrawing from the solution at a controlled speed [181]. Mirri [179] et al. produced thin conductive films based on CNTs by dip coating. The film thickness through dip coating can be controlled by adapting the withdrawal speed as well as the solution concentration. It was reported that faster withdrawal speed and higher CNT concentration resulting in thicker films, because a faster withdrawal speed pulls more fluid up onto the substrate before flowing back down into the solution [179, 181]. However, to produce high-quality and uniform coatings with dip coating, more precise control of withdrawing speed and the super clean environment is required.

4.1.1.5. Ink-jet printing

Recently, ink-jet printing has drawn significant attention for deposition of nanostructures, owing to its high efficiency, utilization and resolution [184, 198]. Compared with other traditional wet methods, ink-jet printing is more suitable for industrial-scale production [184]. Kwon et al. [187] reported a homogeneous conducting film based on MWCNT deposited on paper by using a commercial ink-jet printer. Taishi et al. [184] fabricated SWCNT thin film transistors on plastic substrates using the ink-jet printing method. Huang et al. [199] also reported that ink-jet printing processes were used to print various graphene-based patterns on diverse flexible substrates, including paper, Polyethylene terephthalate (PET) and polyimide foils.

To print high quality patterns, it is essential to produce good quality CNT ink, which requires a low surface tension and viscosity to possess proper fluidic characteristics [193]. Therefore, the inks currently employed are normally based on volatile solutions containing nanostructures [198]. However, the inks contained volatile organic solvents and toxic materials are prone to introducing defects or impurities on the substrate [198]. Due to the high surface area to volume ratio of CNTs, large van der Waals forces between carbon nanotubes lead to agglomeration [193], the tangled and coiled bundles of which can easily block the small nozzle of an ink cartridge in ink-jet printer [187]. Since the development of commercially available and bioactive CNT ink is a big challenge, the potential application of ink-jet printing is still limited in the area of CNT device fabrication [198].

In summary, wet methods hold many advantages for depositing and patterning CNTs, which not only allow a rapid printing process at low cost, but also requires no post processing steps or

prefabrication of templates [193]. All these advantages make wet approach conducive to industrial and commercial production, especially spray and dip coating, which is suitable for scale up and can be adapted to high-throughput coating processes [179].

However, transferring CNTs through a liquid phase is inevitable to apply CNT dispersions. As is known, CNTs are subject to relatively large van der Waals forces because of high aspect ratio, which makes them stick together and form large bundles [196, 200]. Besides, CNTs are quite difficult to disperse in a liquid, therefore, wet methods rely on the use of dispersants and sonication to assist the dispersion of individual nanotubes inside the suspension [179, 196]. Dispersants used in carbon nanotube suspensions adsorb strongly on the surface of CNTs and are very difficult to remove, thus form a physical barrier around the carbon nanotubes and affect the electrical properties of CNT-based device [179, 193]. Sonication stabilizes CNTs dispersion, but which also can shorten carbon nanotubes and cause defects [193]. Defects negatively affect the inherent conductivity of the carbon nanotubes; and shortening CNTs leads to decreasing conductivity of CNT networks, because which not only reduces the probability of forming long electron pathways but also increases the amount of CNT-CNT junctions per unit area [179, 201, 202]. Additional, “coffee ring” effect significantly hinders the formation of uniform patterns during the evaporation process of wet method. Although some modified wet methods, especially spray coating or ink-jet printing, have been applied to diminish the effect, which remains an unavoidable problem. Therefore, aligned individual CNTs arrays with a controllable orientation are difficult to transfer and pattern through this approach.

4.1.2. Dry methods

As an emerging way for nanostructures transferring, dry methods don't require dispersants and sonication during the entire process, thus allowing for better contact between carbon nanotubes.

4.1.2.1. Soft lithography

Soft lithography is a non-photolithographic technique for microfabrication that uses an elastomeric stamp (e.g. poly-dimethylsiloxane, PDMS) to transfer patterns to a target substrate [203, 204]. Recently, soft lithography began to be used combining with wet methods for inking rubber stamps with various nanostructures, and then which was transfer printed onto different types of target substrate [189]. Meitl et al. [189] combined drop casting and soft lithography together to transfer collections of individual SWCNTs onto a wide range of substrates, including plastic sheets.

Soft lithography holds a variety of advantages, like quite simple, inexpensive and accessible, which does not need protected laboratory environment, complex laboratory facilities and high-

energy radiation [203]. Moreover, soft lithography method offers high resolution, which can be used to transfer high-quality patterns with lateral dimensions from ~ 30 to 500 nm [203]. The common stamp material PDMS is homogeneous, chemically inert and biocompatible [196], which can be used over 100 times without noticeable degradation in performance [203, 205]. Therefore, soft lithography has expanded rapidly over the last ten years [204].

4.1.2.2. Transfer printing

A traditional fabrication approach for nanodevice is first to place nanomaterials on a target substrate and then to add electrical connections. But transfer printing is a quite new and specific method which can directly transfer components or monolithic as-fabricated CNT devices onto various target substrates, including both rigid and flexible substrates [177, 178, 206].

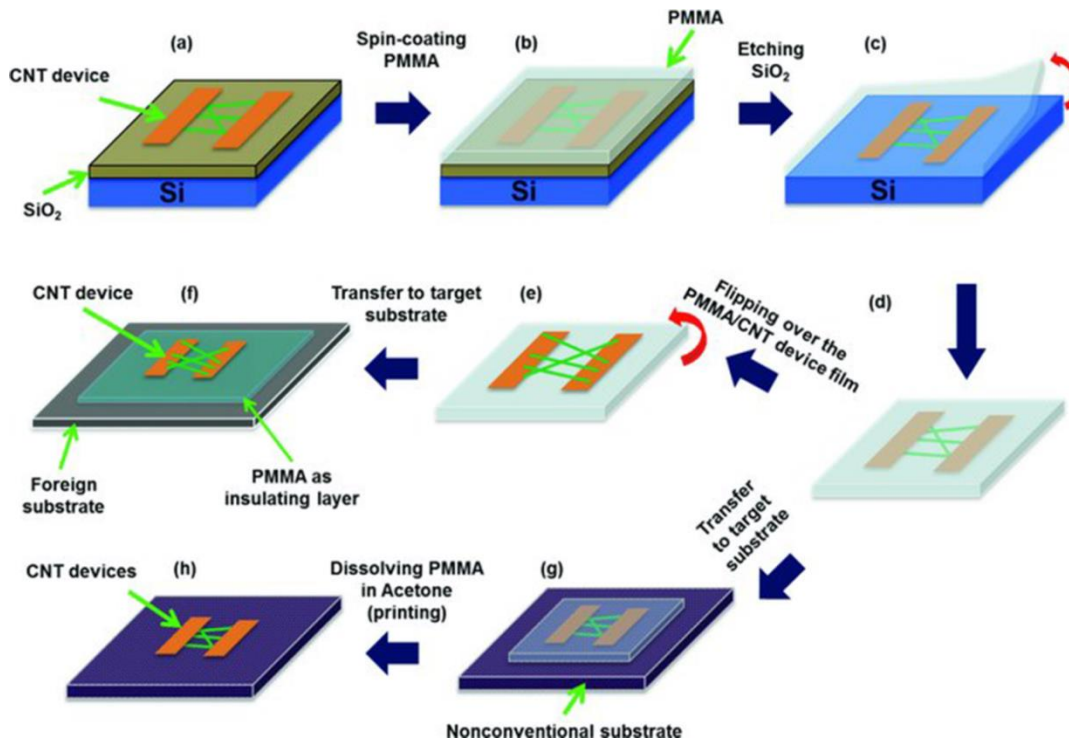


Fig. 4.3: Transfer-printing process flows for CNT devices onto non-conventional substrates reported by Thanh [177]: (a) the CNT devices are pre-fabricated on a Si/SiO₂ substrate, (b) PMMA is spin-coated on the device, (c) SiO₂ is etched, (d) and the PMMA/CNT-device film floats in the water bath, (e, f) the PMMA/CNT-device film is flipped over and placed on a foreign substrate, (g, h) PMMA/CNT-device film is printed on a non-conventional substrate followed with dissolution of PMMA.

Thanh et al. [177] reported a printing approach of complete transferring as-fabricated CNT devices from SiO₂ substrate onto various non-conventional substrates, as shown in Fig. 4.3. PMMA was applied as a carrier substrate and firstly spin-coated on CNT devices. Secondly, a sacrificial SiO₂ layer was etched away via submerging the whole structure in a buffered oxide etch (BOE) solution. Then the PMMA/CNT-device film was released and floated freely on the surface of the BOE bath. The target substrate could be placed underneath the floating PMMA-CNT devices in the water bath and lifted up. The PMMA/CNT-device film can be either used as a stand-alone device or transfer-print it onto a new substrate.

Due to the integration of fabrication process of CNT device, transfer printing method is more difficult and complicated compared with simple wet methods as well as soft lithography. Although transfer printing provides an emerging approach to generate complex three-dimensional structures, which requires the use of sacrificial resists or etching procedures [178, 207, 208]. For many nanomaterials, like Si or metal oxide nanowires, functionalized or doped CNTs, their structures can be destroyed by this type of printing process and thus degrade of their electrical properties. In addition, transfer printing process also strongly relies on the surface chemistry of substrate material, which also limits its application.

4.1.2.3. Direct contact printing

Direct contact printing is an efficient strategy for directly transferring and patterning nanostructures from their growth substrate to different types of target substrates. An appropriate contact between the surface of the growth and target substrate is the key to its success [203], therefore, an external pressure is necessary to be applied to provide intimate contact at the interface between the growth and target substrates [209].

Direct contact printing allows the horizontally aligned CNT arrays to be created and patterned, but good alignment partially relies on the synthesis of high-quality vertically aligned CNTs arrays grown on the surface of the growth substrate. As the recent development of nanotechnology, the synthesis of controlled and uniform assembly of CNTs was comparatively developed. Therefore, direct transfer printing CNTs from their growth substrate is rapidly becoming important in CNT electronics applications [209]. Kim et al. [210] transferred vertically aligned CNTs from a chemical etching anodic aluminum oxide surface to Pt coated Si substrate via direct contact printing method. Fan et al. [211] reported wafer-scale assembly of highly ordered arrays of semiconducting nanowires were directly contact-printed onto complex structural configurations on SiO₂ substrates.

The primary benefit of contact printing in comparison to other established processes for transfer, is that the process is performed completely in the dry state [208]. Due to no requirement of

chemical and physical treatment as well as sonication and vacuum processing, direct contact printing method minimizes the risk of contamination or process-induced damage [183]. Compared with soft lithography and transfer printing technology, this process is simpler, quicker, less destructive, scalable to large areas, and able to successfully assemble highly aligned and dense CNT parallel arrays [211]. Moreover, direct contact printing also offers low temperature processing, wide compatibility with various substrates, availability of no-mask patterning and no requirement of the extra clean experimental environment [183].

4.2. Results and discussion

In this study, direct contact printing approach was applied for transferring and patterning horizontally highly-aligned multiwall CNTs onto the surface of various rigid and flexible target substrates, including Si/SiO₂, quartz, glass and Kapton® polyimide. After transfer process, for the fabrication of electronic chemiresistive devices, metal interdigitated electrodes were deposited across to the alignment of CNTs and served as low-resistance leads.

The “ink” for the direct contact printing consists of a dense “forest” of vertically aligned N-MWCNTs with the height of ~4 μm, which were synthesized by chemical vapor deposition on Si/SiO₂ substrates. No requirement of super clean experimental environment or expensive equipment, the complete transfer process was operated readily at room temperature in open air. The whole procedure of our direct contact transfer process was detailed described in section 2.2.3.

Up to now, knowledge about CNT alignment observed on the large-scale is very limited [212, 213], the main issue is a difficulty to observe nanostructures at a micrometer scale [186]. SEM is a useful technique, which requires minimal sample preparation and provides versatile information of nanostructures garnered from different detectors. However, one drawback of SEM is that the samples are required to be conductive solids. Insulating substrates like glass, quartz, and polyimide foils are extremely difficult to be characterized by SEM. Due to these reasons, Si/SiO₂ is predominantly applied as the target substrate in this chapter exclusively for analyzing the morphology and distribution of CNTs if there is no specific mention. Other insulated substrates, like glass and polyimide foil, also were characterized by SEM after metal interdigitated electrodes are patterned on top.

To compare the difference between drop casting and direct contact printing, a growth substrate with a high-quality alignment of CVD grew MWCNTs shown in Fig. 4.4(a), was cut into two identical pieces, one was drop-casted (after dispersing in 1% SDS water solution) onto the Si/SiO₂ target substrate (see Fig. 4.4(b)), and the other was directly transferred through contact printing approach (Fig. 4.4(c)).

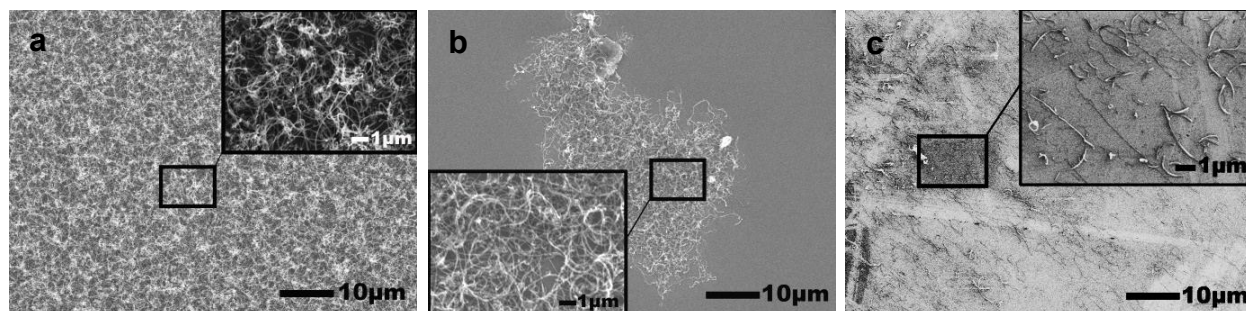


Fig. 4.4: Comparison of morphologies of nanotubes (a) before and after the transfer process through (b) drop casting and (c) direct contact printing methods. (a) Scanning electron micrographs of close-packed arrays of N-MWCNTs on a large region of Si/SiO₂ growth substrate. (b) SEM images of inhomogeneous network of N-MWCNTs transferred on Si/SiO₂ target substrate through drop casting N-MWCNTs/SDS dispersion. (c) SEM image of regular array assembly of isolated N-MWCNTs located on a large area of Si/SiO₂ target substrate which was transferred from the growth substrate through direct contact printing with an external pressure of ~3 kPa.

Fig. 4.4(b) and its insert show highly random and inhomogeneous network of highly entangled MWCNTs through drop casting. This non-uniform distribution often happens by using drop casting method, because suspended CNTs tend to agglomerate during the evaporation of a solvent. In addition, relatively large particles of impurities were also observed in Fig. 4.4(b), which may be introduced during the chemical treatment process of CNTs for assisting the dispersion of individual nanotubes inside the suspension. Once transferred CNTs are well-deposited on the target substrates, it is scarcely possible to remove those impurities from the surface. However, transferred CNT arrays for the purpose of integrating with electronic devices are required to be clean and undamaged for obtaining good electronic properties [189]. Therefore, all wet transfer methods, like drop casting, dip coating, and spray coating, have high requests for the extremely clean experimental environment because foreign instances are quite easy to be brought.

In Fig. 4.4(c), uniform and highly dense parallel arrays of N-MWCNTs were transferred and assembled over the entire area of the target substrate after the contact with the growth substrate. During this printing process, a pressure of 3 kPa was exerted at the interface for maintaining an intimate contact between the growth and target substrates. The higher magnification image in the inset of Fig. 4.4(c) shows that the lengths of those isolated and aligned nanotubes are mainly larger than 3 μm (the interspacing distance of interdigitated electrodes), as expected, which

means most these patterned nanotubes can directly bridge two electrodes of our chemiresistive devices for gas- and bio-sensing. Above all, direct contact printing of CVD-grown MWCNTs outperforms solution-deposited CNTs because of their highly uniform and aligned formation over a large surface area.

During the contact printing, vertically aligned MWCNT structures were “toppled” over while making an intimate contact between the interface of the growth and target substrate by exerting an additional pressure on the interface. Schematic diagram of this process is presented in Fig. 4.5 (a). Some carbon nanotubes were released from the growth substrate and anchored on the surface of the target substrates by the van der Waals interactions (see Fig. 4.5(d)), while the rest of nanotubes were left on the growth substrate (Fig. 4.5 (c)); which probably attributes to relatively strong interaction between the bottom of MWCNT and the growth surface. From the mechanism of direct contact printing, it can be summarized that the surface density of as-grown CNT arrays and the mechanical link due to pressure play an important role for the scalable and repeatable formation of highly aligned horizontal N-MWCNT arrays with controlled surface coverage.

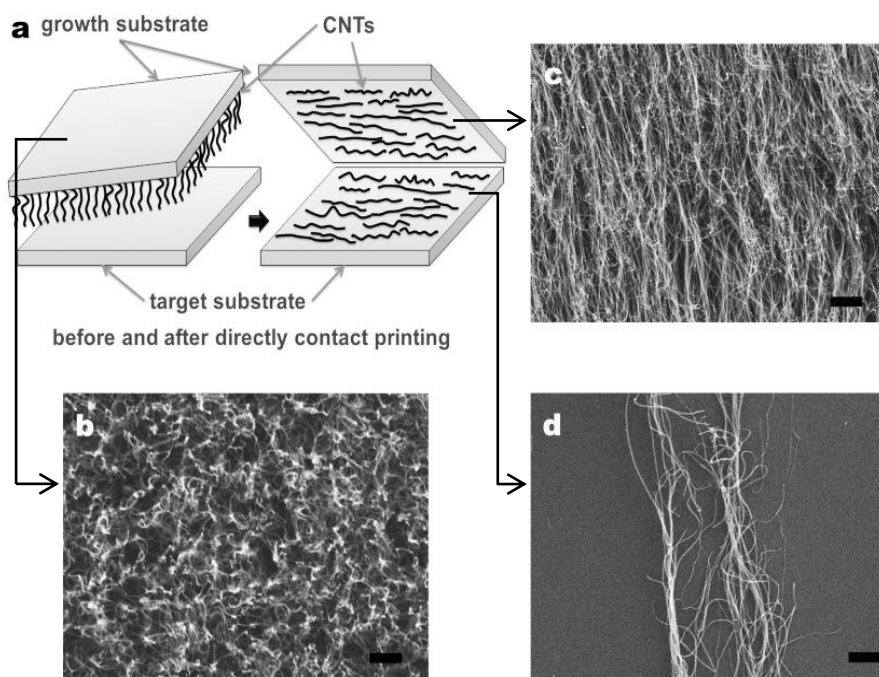


Fig. 4.5: (a) Schematic presentation of the direct contact printing process of CVD grown MWCNTs. (b, c) SEM image of N-MWCNTs synthesized from pure acetonitrile grown on a Si/SiO₂ substrate before (b) and after (c) contact-printing process. (d) SEM image of the alignment of N-MWCNTs transferred onto Si/SiO₂ target substrate.

The external pressure applied during contact-printing process is 2 kPa. (The scale of data-bar is 1 μm .)

4.2.1. Stability and scalability

In order to fully utilize those CNTs remaining on the growth substrate after the first transfer, we reused the growth substrates. The maximum feasible reutilization times of a growth substrate for direct contact printing were studied: an as-grown growth substrate (Fig. 4.6(a)) was utilized for direct contact printing for eight times under the same experimental condition, and the morphology of transferred CNTs is presented in Fig. 4.6(c). It can be seen that direct contact printing presents a good reproducibility over experiments. However, the amount of transferred MWCNTs and mean nanotube's length decreases with the number of reutilization time of the growth substrate. As shown in fig, 4.6(b), the mean length of transferred N-MWCNT arrays decreased from 6 to 2.5 μm , approximately. After reutilizing the growth substrate over 5 times, the uniformity of the MWCNT arrays on the growth substrate was diminished successively, thus leads to the lower transfer efficiency; and the shortening of CNTs probably be attributed to over-intimate contact and repeating mechanical friction of the interface between the growth and target substrate. For this reason, growth substrates were reused not more than 5 times in later experiments for guaranteeing sufficient length of transferred nanotubes which can directly bridge two metallic microelectrodes.

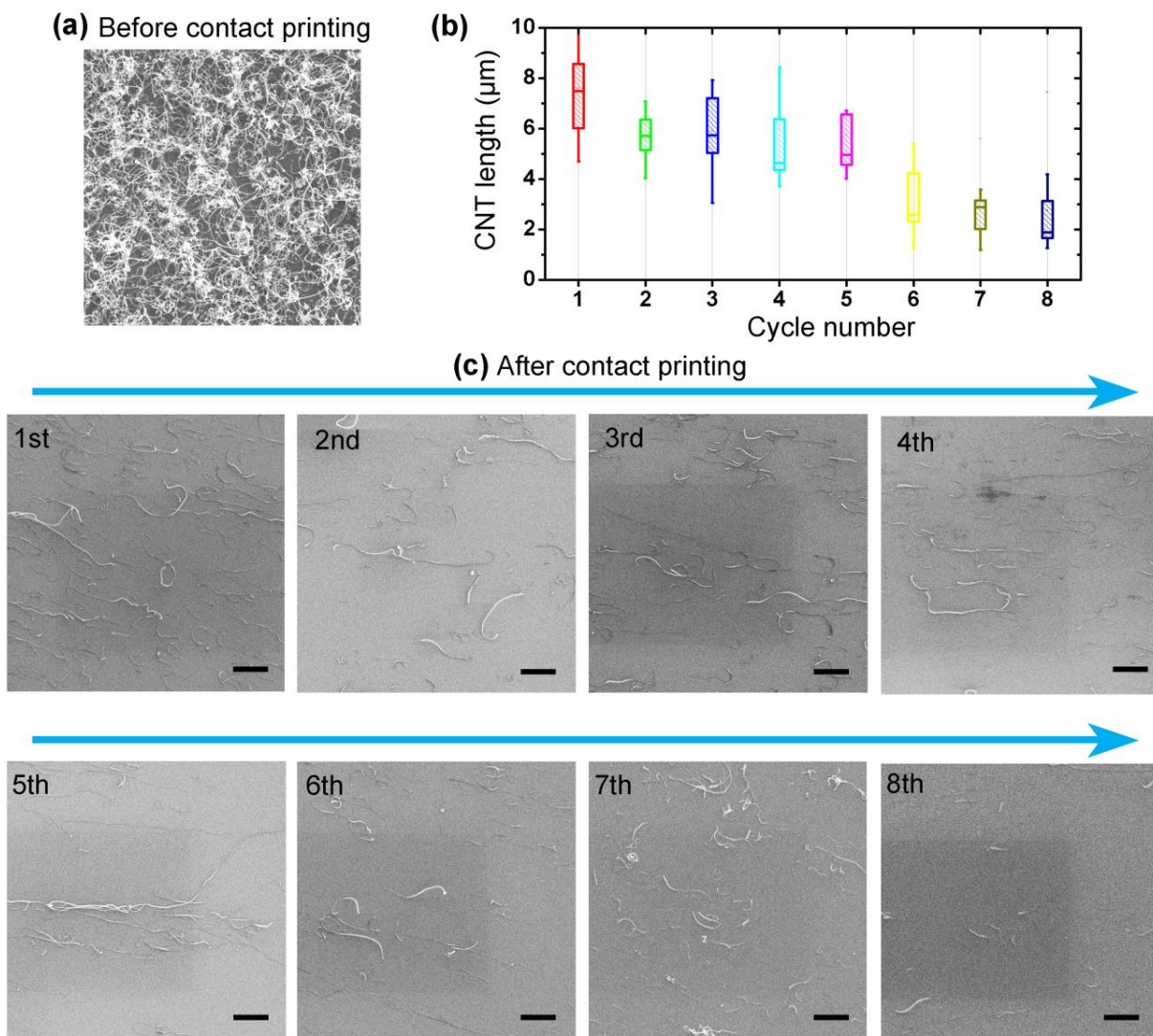


Fig. 4.6: (a) Top view (SEM image) of N-MWCNTs synthesized from pure acetonitrile grown on a Si/SiO₂ substrate before contact-printing process. (b) The length distribution of transferred N-MWCNTs on target substrate Si/SiO₂ plotted as a function of cycle numbers. (c) SEM images of horizontally aligned N-MWCNTs on Si/SiO₂ target substrate, which were repeatedly transferred from a same MWCNT sample for 1-8 times. (The scale of data-bar is 2 μm .)

4.2.1.1. The influence of external pressure

To study the influence of external pressure at the interface between the growth and target substrate on the effect of contact printing process, a growth substrate with highly dense N-MWCNT arrays was cut into four pieces. Different external pressures varying from 0.5 to 3.0

kPa were applied for keeping intimate contacts at the interface between the growth and target substrates. Fig. 4.7 shows the alignment of those transferred N-MWCNTs: isolated nanotubes, aligned arrays as well as thin films of CNTs were patterned respectively with the direct contact printing method with an increasing external pressure. In Fig. 4.7(a), an isolated carbon nanotube contact-transferred onto the target substrate at the lowest external pressure of ~ 0.5 kPa is shown. Fig. 4.7(b) exhibits parallel CNT arrays consisting of individual CNTs or small CNT bundles assembled on the substrate at an increasing pressure of ~ 1.0 kPa and oriented predominantly along the printing direction. As the external pressure further was increased above 2.0 kPa, printed CNT bundles were connected together to form thin, uniform and well-aligned MWCNT films on the Si/SiO₂ target substrate, as shown in Fig. 4.7(c,d). According to Fig. 4.7, it is clearly demonstrated that the surface density of directly contact-printed CNTs can be varied from a few tubes per square micron to a multilayer CNT film through adjusting the pressure exerted at the interface between the growth and target substrates.

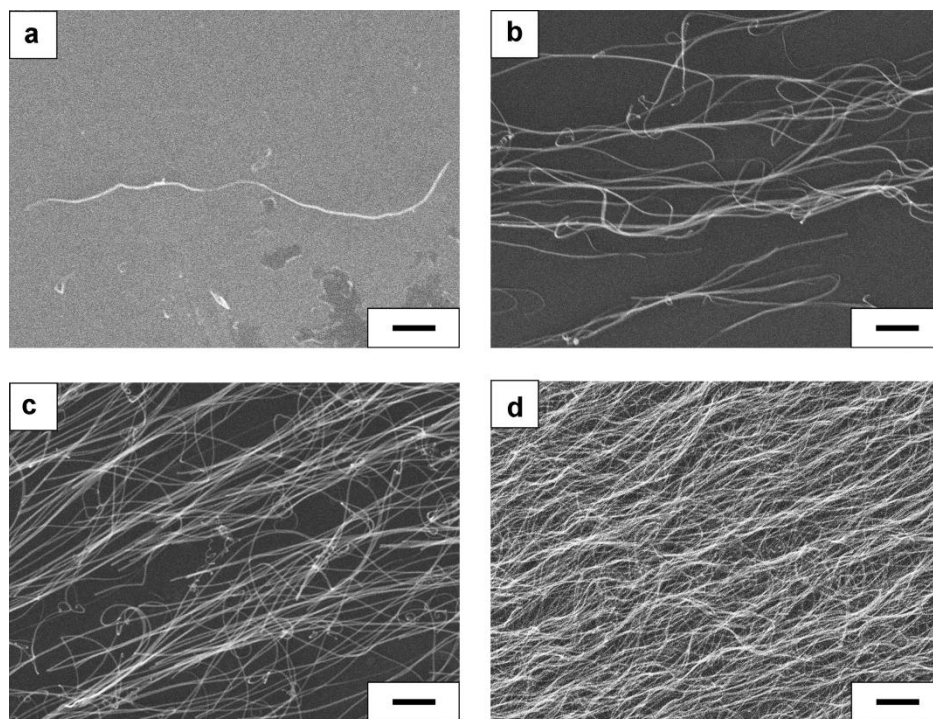


Fig. 4.7: SEM images of transferred N-MWCMT arrays onto Si/SiO₂ target substrates via direct contact printing with different pressure of (a) 0.5, (b) 1.0, (c) 2.0, and (d) 3.0 kPa exerted on the interface between the growth and the target substrates. (The scale of data-bar is 1 μm .)

4.2.1.2. The influence of surface density

It is well-accepted that CVD method is quite a sensitive way of synthesis of CNTs in which the surface density of CNTs is determined by a variety of parameters, such as chemical composition, reaction temperature, geometrical features of the catalyst particles and other [214]. Through this specific character of CVD synthesis, the density of as-grown vertical CNT arrays can be optimized to improve the scalability of the contact-printing process. SEM images in Fig. 4.8(a-c) present the morphology of CVD grown N-MWCNT arrays with a varying surface density grown on the substrate. The arrays are composed of thousands of carbon nanotubes, which are difficult to quantify. In order to quantitatively characterize the surface density of as-grown CNT arrays, a “pixel comparison” approach by Dr. H. Yang was introduced to calculate the coverage of surface through comparing the number of black and white pixel in the high-contrast SEM image of nanotubes. Because of a much higher conductivity of CNTs compared with Si/SiO₂ substrate, carbon nanotubes are always presented more bright (almost white) than their background in SEM images. Therefore, the coverage of nanotube can be represented by the coverage of white pixel in high-contrast SEM images. According to this “pixel comparison” method, the surface coverage of nanotubes in SEM images from Fig. 4.8(a-c) is ~24.8 % in (a), ~17.3% in (b) and ~1.6% in (c), respectively, which shows an obvious downward trend. During the transfer process, the same pressure was exerted at the interface of the growth and target substrates to investigate the influence of coverage of nanotubes on the direct contact printing. The scanning electron micrographs of transferred CNTs are presented in Fig. 4.8 (d-f). The coverage of nanotubes in Fig. 4.9 (d-f) was also obtained through “pixel comparison” approach, which gives ~0.9, ~0.8, and ~0.2%, successively. It clearly indicates that a lower coverage of surface at growth substrate leads to a lower amount of resulting CNTs after the direct contract printing.

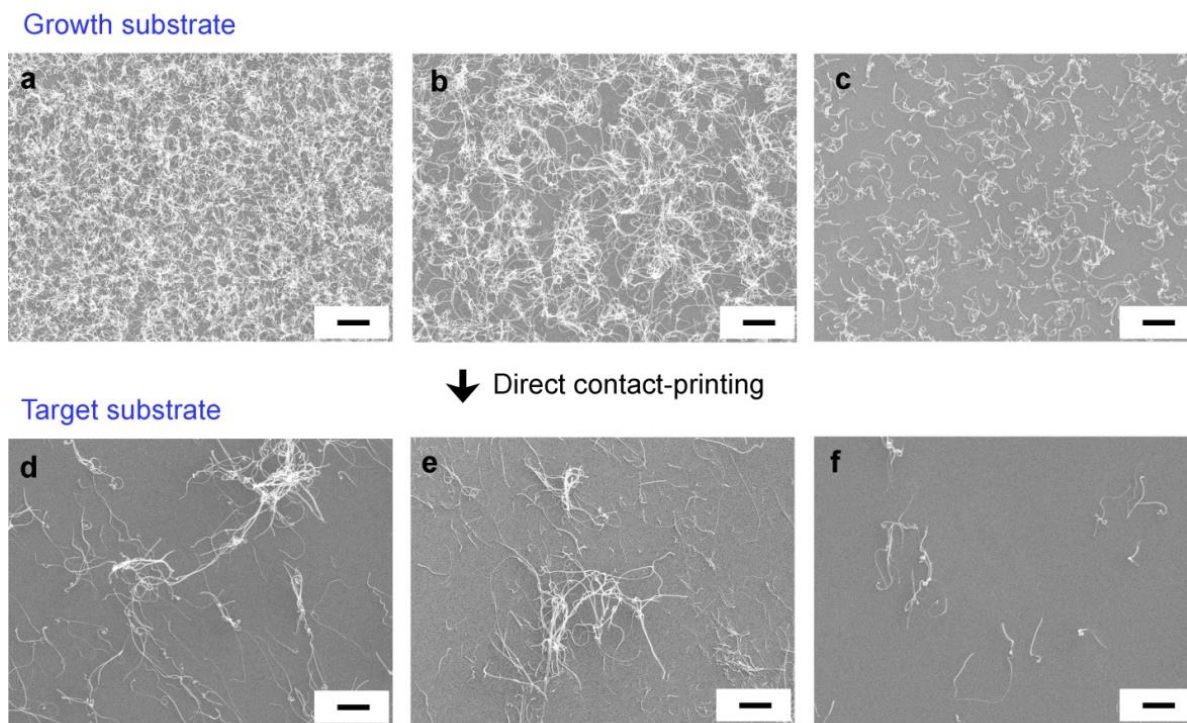


Fig. 4.8: (a-c) SEM images of vertical N-MWCNTs grown on the Si/SiO₂ substrates via CVD method which have various coverage of nanotubes: (a) 24.8%, (b) 17.3% and (c) 1.6%, respectively. (d-f) SEM images of resulting horizontal N-MWCNTs transferred from the growth substrate (a-c) to the target Si/SiO₂ substrates, the coverage of surface in (d-f) is 0.9%, 0.8% and 0.2%, respectively. (The scale of the data-bar is 2 μm.)

Above all, direct contact-printing approach shows high stability and reproducibility, which allows a good density control and nanotube alignment. However, SEM images shown above also indicate that it is difficult to improve the surface coverage of transferred MWCNTs on the target substrate, small bundles often forms due to agglomerating when contact printing is performed, which may attribute to poor interactions between Si/SiO₂ and nanotubes. Thus, surface modification of target substrate was applied to improve the interactions between nanotubes and target substrates.

4.2.2. Chemical functionalization of target substrates

The direct contact printing for vertically aligned N-MWCNT films described here is based on the principle that van der Waals interaction between vertically grown nanotube films and the target

substrate is greater than the van der Waals interaction and bonding strength of the nanotubes to the growth substrate [208]. Therefore, this printing method is strongly influenced by adhesion energies between different substrates [207, 215]. Hines et al. [207] described the physical insight of this adhesion strength with Dupré equation:

$$E_A^{AB} = \gamma_A + \gamma_B - \gamma_{AB} \quad (4.1)$$

Where E_A^{AB} is the interfacial binding energy between materials A and B, $\gamma_{A(B)}$ is the surface free energy of A (B), and γ_{AB} is the interfacial free energy [207, 216]. According to this equation, transfer of material A from substrate B to substrate C requires:

$$E_A^{AC} > E_A^{AB} \quad (4.2)$$

During this process, two materials which both have either strong dispersive (oleophilic) or strong polar (hydrophilic) components are likely to adhere well [207]. Therefore, specific chemical treatments on the target substrates strongly influence the direct contact printing of carbon nanostructures. Pint et al. [208] reported that surface roughness (commercially available polymers with microscale roughness) and surface potential influence CNT transfer process. Fan et al. [211] also reported that chemical modification of $-NH_2$ terminated monolayers on the surface of Si/SiO₂ substrates can improve the density of transferred nanowires.

In our study, octadecyltrichlorosilane (C₁₈H₃₇SiCl₃) (ODTS) was applied to chemically modify the surface of target substrate Si/SiO₂. ODTS is an amphiphilic molecule consisting of a long-chain alkyl group (-C₁₈H₃₇) and a polar head group (-SiCl₃), which is widely used to chemically modified various oxide substrates [217]. During the treatment process, ODTS formed a self-assembled monolayer on a SiO₂ surface and the alkane chains changed the property of the SiO₂ dielectric layer from hydrophilic to hydrophobic character [217]. Contact angles of target substrate before and after ODTS modification were presented in Fig. 4.9, measured by dropping casting a water droplet with a volume of 10 μ L on as-prepared and ODTS-treated target substrate Si/SiO₂, respectively. The contact angle increased from 34.6° to 79.1° after ODTS chemical treatment, indicating the formation of ODTS self-assembled monolayer has changed the property of Si/SiO₂ surface from hydrophilic to hydrophobic state.

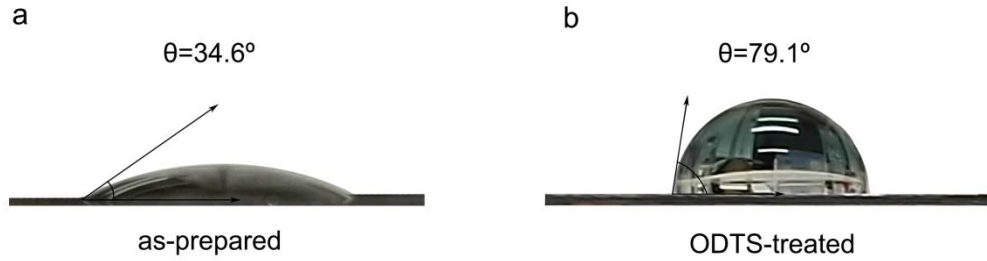


Fig. 4.9: Water contact angles of target substrate Si/SiO₂ (a) before and (b) after ODTS surface modification (The volume of the droplet is 10 μ L).

The contact angles and surface free energies of the SiO₂ after ODTS surface treatments were also reported by Lim et al. [217] and listed in Table 4.1. According to Lim, ODTS-treated SiO₂ substrate exhibited smaller surface free energy, indicating hydrophobic states. As described above, two materials which both have either strong hydrophobic or hydrophilic components are likely to adhere well during the contact-printing process. The SiO₂ surface can be characterized as polar (hydrophilic), whereas ODTS-treated SiO₂ surface can be characterized as dispersive. When ODTS was introduced onto a Si/SiO₂ surface, the hydrophilic head was absorbed onto SiO₂ layer, while its hydrophobic tail can be adsorbed at the surface of touching carbon nanotubes, which improves the adhesion strength of nanotubes to the Si/SiO₂ surface.

Table 4.1: Contact angle and surface free energy for SiO₂ substrates before and after ODTS surface treatment reported by Lim [217].

Surface treatment	Contact angle			Surface free energy (mJ/m ²)
	D.I. water	Glycerol	Di-iodomethane	
as-prepared	35.72°	22.44°	25.19°	61.37
ODTS-treated	78.98°	81.14°	43.92°	28.05

To study the role of ODTS surface modification of the target substrate on direct contact printing, a growth substrate was cut into two pieces and used for direct contact printing under the same experimental conditions. SEM was applied to compare the morphology of horizontal MWCNT printed on the non-treated or ODTS-treated Si/SiO₂ substrate, as shown in Fig. 4.10.

Without ODTS coating, the target substrate in Fig. 4.10(a) presents randomly aligned individual nanotubes with a very low surface density. However, the surface coverage of printed CNTs in Fig. 4.10(b) was significantly increased after chemical modification of the surface of target substrate with ODTS, indicating improved adhesion strength of nanotubes on Si/SiO₂ surface. However, ODTS treatment also can influence the electronic performance of CNTs, as shown in Fig. 4.10(b). The SEM contrast of CNTs was significantly decreased due to the formation of ODTS self-assembled monolayer, which may be suggested that ODTS molecules absorb on the surface of CNTs and form a physical barrier around the carbon nanotubes, leading to a relative decrease in conductivity of nanotubes.

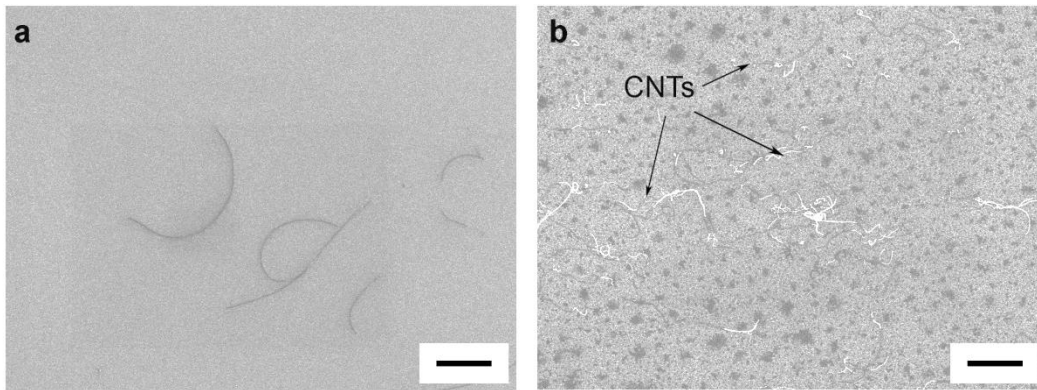


Fig. 4.10: SEM image of N-MWCNTs directly contact-printed at 5 kPa on the surface of Si/SiO₂ substrate without (a) or with (b) ODTS treatment. (The scale of the data-bar is 5 μm .)

In the field of electronics, Si/SiO₂ is a common material for a device substrate, because it consists of an insulating layer covering the conducting layer, which can be used for back-gated FET. However, carbon nanotubes adhered weakly to SiO₂, and an external pressure is required for the efficient direct contact printing. Chemical treatment with ODTS can modify the hydrophilic nature of SiO₂, but it also influences the electronic properties of nanotubes. In addition, insulating SiO₂ layer on Si wafer can easily be scratched during contact printing process because of close contact with growth substrate, which causes serious leakage in fabricated devices. Therefore, other insulating substrates, such as quartz, glass and polyimide foil were applied as target substrates for transferring and integrating CNTs into electronic devices (chemiresistor-type sensors) in this study.

4.2.3. Other insulated target substrates

In this study, insulating substrates were found to be appropriate for the use as support substrates for the fabrication of CNT-based chemiresistor bio- and gas- sensors, which requires no gate electrodes. However, one key drawback of insulating substrates is that carbon nanotubes deposited on them are extremely difficult to observe in SEM. To solve this problem, these substrates were characterized by SEM after the deposition of metal interdigitated electrodes onto the CNT-printed substrates, which improved the conductivity of the whole system. The interdigitated electrodes consist of ~ 3 nm Cr layer at the SiO_2 surface and ~ 50 nm Au layer on top, which were deposited through photolithography and thermal evaporation method. The detail of the fabrication process can be found in chapter 2.

4.2.3.1. Quartz

Quartz was first applied for the replacement of Si/ SiO_2 , because it has similar surface chemistry to the thin SiO_2 layer on Si/ SiO_2 wafers. Moreover, CNT-based devices fabricated on quartz are fully transparent that holds the potential to apply them in transparent circuits and transparent displays.

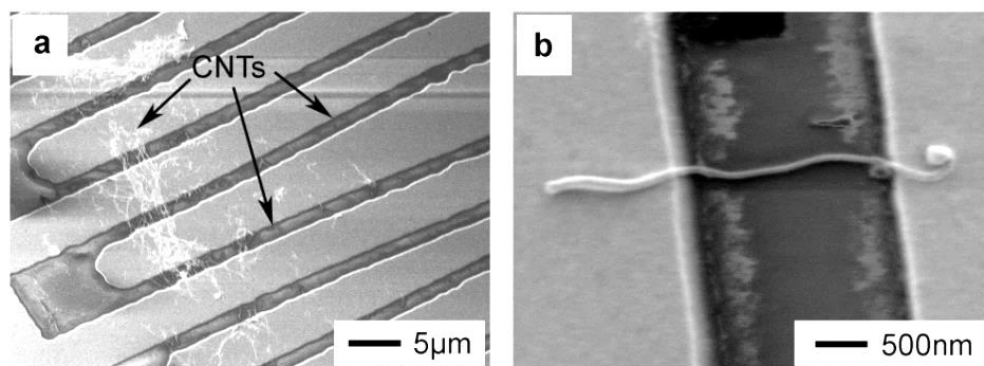


Fig. 4.11: SEM images of (a) regular array assembly of N-MWCNTs and (b) a single N-MWCNT printed on the quartz substrate partially covered by deposited Cr/Au (3nm/50nm) interdigitated electrodes with an interspacing distance of ~ 3 μm .

The SEM images of the aligned N-MWCNT contact-printed on a quartz substrate are shown in Fig. 4.11. It is demonstrated that the adhesion of nanotubes on target substrate is strong enough to sustain the sonication and other chemical treatments during microfabrication process for

depositing interdigitated electrodes. Lower magnification SEM characterization of Fig. 4.11(a) presents the alignment of the MWCNT bundles in the arrays perpendicular to the interdigitated electrodes. Fig. 4.11(b) shows a higher magnification image of an individual carbon nanotube bridging two metal electrodes, and the ends of which were covered by the Cr/Au layer. As shown in Fig. 4.11, the surface density of nanotubes can be varied from a single nanotube to CNT bundles by altering the nanotube surface on growth substrates as well as external pressure during mechanical contact between the growth and target substrate.

4.2.3.2. Glass

Compared with quartz, the glass substrate is cheaper and also transparent. Replacing quartz with glass primarily aimed at reducing the cost of device fabrication. Fig. 4.12(a) shows the SEM image of a large coverage of highly dense and uniform N-MWCNTs alignment printed on the surface of glass substrate. The higher magnification image in Fig. 4.12(b) shows two electrodes with an interspacing distance of 3 μm are bridged by MWCNT arrays. Due to high surface density, some nanotubes in Fig. 4.12 are in contact with other nanotubes, while some nanotubes are completely isolated without having a contact with any other CNT.

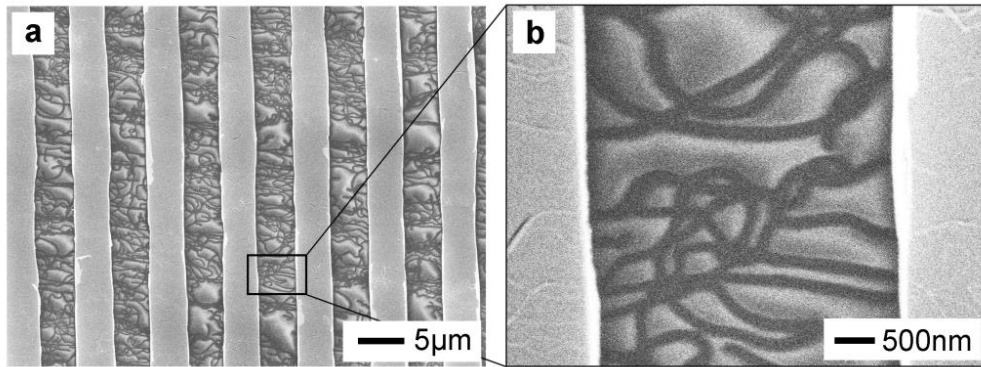


Fig. 4.12: (a) SEM image of a large region of uniformly printed N-MWCNTs arrays coated with Cr/Au (3nm/50nm) interdigitated electrodes (interspacing distance of 3 μm) on a glass substrate. (b) Higher magnification SEM image of N-MWCNT arrays bridging two neighboring interdigitated electrodes.

4.2.3.3. Polyimide film

Recently, an interest in electronic devices on flexible substrates arose extremely owing to higher mechanical robustness, which can apply in the areas of wearable, hand-held and portable consumer electronics [198, 206]. Among a different variety of active sensing materials, CNTs are very suitable for flexible electronic devices because of their high conductivity and current carrying capacity, as well as excellent mechanical properties and structural stability [200, 218]. In our work, Kapton® polyimide film was applied as the target substrate for the fabrication of flexible CNT-based chemiresistor-type sensor devices.

Not like SiO₂ surface which is characterized as polar, organic surface like Kapton® polyimide film can be characterized as dispersive [207]. It has reported that CNTs have stronger adhesion to materials with dispersive surfaces than with polar substrate [207]. In this case, a less mechanical pressure is required to exert at the interface between the growth and target substrates.

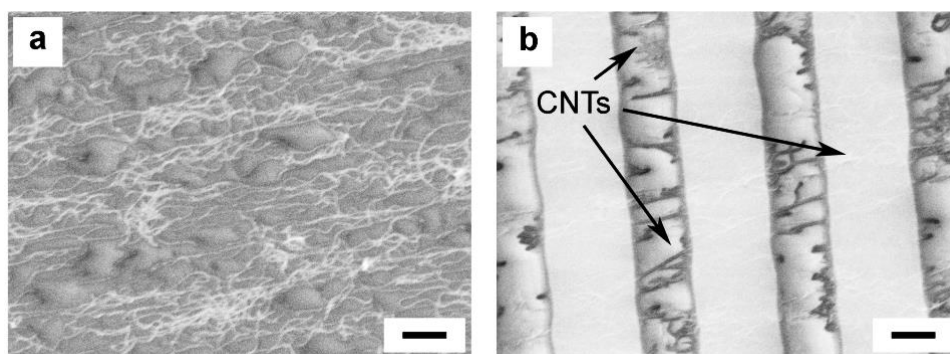


Fig. 4.13: SEM images of N-MWCNTs arrays printed on polyimide films (a) without or (b) with the coverage of Cr/Au (3nm/50nm) interdigitated electrodes.

As shown in Fig. 4.13(a), excellently aligned and dense N-MWCNT arrays were contact-printed onto the polyimide film, and they can be nicely seen without depositing metal interdigitated electrodes. Fig. 4.13(b) presents the SEM image of those highly dense and uniform parallel N-MWCNTs arrays, which were covered by Cr/Au interdigitated electrodes with an interspacing of 3 μm . The N-MWCNT arrays consist of uniformly distributed individual N-MWCNTs with a well-defined direction. Ishikawa et al. [206] reported that the use of massively aligned CNTs enabled the flexible devices to exhibit high performance in contrast to random CNTs networks,

including higher mobility, lower power consumption, higher switching speed and better mechanical flexibility.

4.3. Conclusion

In this chapter, “direct contact printing” method was developed, which can scalably transfer uniform and highly dense parallel arrays of CNTs onto various target substrates, including flexible sheets. The surface density of printed MWCNTs can be varied from few tubes per square micron to multilayer of the MWCNTs film by optimizing the surface density of as-grown MWCNTs as well as mechanical linking due to external pressure and surface functionalization. To improve interaction between nanotubes and target substrates, ODS chemical treatment was applied to form a self-assembled monolayer on the surface of oxide substrate, which alters the properties of substrate from hydrophilic to hydrophobic state and improves the adhesion of nanotubes on target substrates.

By using contact printing method, we have transferred well-aligned MWCNT arrays onto both rigid and flexible substrates with a large coverage, such as Si/SiO₂, quartz, glass and Kapton® polyimide foils. Without a requirement of CNT functionalization or sonication, contact printing method can be achieved completely in a dry condition under room temperature, which offers the possibility of fabricating reliable and stable CNT based electronics.

5. Performance of N-MWCNTs based biosensor

Avian influenza virus, especially H5N1 has become nowadays a very dangerous pathogen threatening not only for poultry. Highly pathogenic AIV H5N1 can infect people and can be transmitted from human to human that can have disastrous implications for public health [219, 220]. High-sensitive and rapid detection of H5N1 infection would allow early antiviral therapy and control the outbreaks [221-223]. However, the most commonly used detection techniques are laborious, time-consuming, or require specialized laboratory facilities and well-trained technical personnel, which greatly limit their application in clinical tests [224-226].

Herein we developed a label-free chemiresistor DNA sensor based on N-MWCNTs for highly sensitive and fast detection of AIV subtype H5N1 DNA sequences at room temperature. Our CNT chemiresistor DNA sensor is not only low-cost and highly sensitive, but also flexible that can be easily integrated into portable devices.

In this chapter, avian influenza virus itself and a review of its detection methods will be briefly introduced; the chemiresistor CNT-based DNA sensor developed by us will be introduced; the CNT functionalization with probe DNA as well as the sensing performance of the sensor in detecting the DNA sequence of AIV H5N1 virus from 0 pM to 2 μ M will be discussed in detail; additionally, the repeatability and selectivity of the DNA sensors will be studied.

5.1. Overview of AIV detection

5.1.1. Avian influenza virus

The avian influenza viruses are members of the Orthomyxoviridae family of RNA viruses, which are characterized by a segmented genome of single-stranded negative-sense ribonucleic acid (RNA) located within an enveloped virus particle [227, 228]. Influenza viruses are grouped into A, B, or C type genera, each genus of the viruses is further subdivided by serotype based upon the envelope glycoproteins possessing either haemagglutinin (HA) or neuraminidase (NA) activity [229-234]. To date, 15 HA (H1-H15) and 9 NA (N1-N9) subtypes of influenza A viruses have been identified [233-235].

The severe form of avian influenza virus termed highly pathogenic (HPAIV) is one of the most feared diseases, due to extremely high flock mortality (nearly up to 100%) [236]. The most well-known example is the HPAIV subtype H5N1 viruses emerged in Hong Kong in 1996, and since then it has spread to over 16 countries across Asia, Europe and Africa [220, 232, 237]. According to WHO [238], a total of 858 human cases of H5N1 have been confirmed since 2003, which caused 453 deaths. This significant and continued spread of H5N1 virus has focused

global attention, high-sensitive and rapid detection AIV detection and diagnostic strategies are urgently needed for early antiviral therapy and control the outbreaks [221-223].

Diagnosis of avian influenza virus can be accomplished in two approaches: either through direct detection of the virus itself, or through indirect detection of antibodies specific for the virus [239, 240]. While conventional laboratory methods used for AIV detection continued to be widely applied, such as “gold standard” identification; new and emerging technologies like direct DNA detection are rapidly being adopted [224, 240]. This chapter will offer a short overview of both traditional and emerging AIV detection methods in recent years.

5.1.2. Direct detection techniques

Direct detection includes conventional culture of infectious virus, as well as the use of more rapid and cost-effective technologies that allow detection of specific viral antigens through immunospecific assays or viral-specific nucleic acids [240, 241]. The most well-known traditional method is “gold standard” identification.

5.1.2.1. Historic “gold standard” identification

The “gold standard” for AIV identification is virus culture in embryonated chicken eggs, followed by a positive result in a HA assay, and subsequent verification of AIV in HA-positive samples by use of a more specific assay, such as polymerase chain reaction (PCR) analysis of genomic viral RNA [234, 240, 242, 243]. The workflow of “gold standard” is shown in Fig. 5.1, which can be divided into three main parts: (i) sample collection and processing, (ii) virus culture and (iii) identification of virus. The last identification parts can be further subdivided into classical methods like HA assay and hemagglutination-inhibition (HI) test as well as molecular methods such as PCR-base technique.

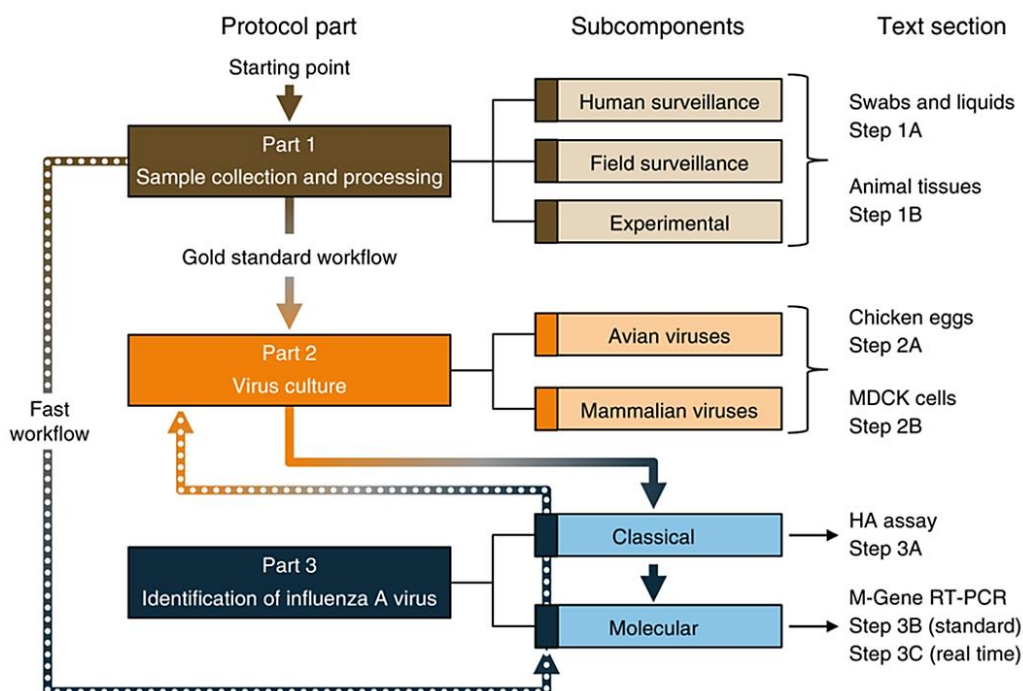


Fig. 5.1: AIV isolation, culture and identification protocol flowchart [242].

1. Virus culture

Virus culture in embryonated chicken eggs can help to detect the infectious virus [244]. The virus is inoculated into the chorioallantoic sac and onto chorioallantoic membrane then incubated for periods of time ranging from 24 to 48 h for high pathogenic AIV virus isolates, and up to 21 days through two or three blind passages for some low pathogenic AIV virus isolates [244].

2. HA and HI assay

A widely used HA and HI assay for the detection of AIV was originally developed by Hirst [245] and Francis [246], which is based on the ability of the viral HA protein to hemagglutinate red blood cells [242, 247]. HA and HI test are relatively inexpensive methods that only use standard laboratory equipment and can be completed within several hours [247, 248]. However, when working with uncharacterized viruses or antibody subtypes, they require extensive laboratory support for the production and optimization of the library of reference reagents for standardizations [247].

3. PCR-based technique

PCR techniques have been developed by Saiki et al. [249] in 1985, which is a diagnosis of virus infection through sensitive detection of specific viral nucleic acids [250]. Since the 1990s, PCR is gradually becoming an alternative approach to directly analyze specific sample material rapidly and sensitively [242, 250]. Up to now, different kinds of PCR techniques have been developed for detection of AIV, including reverse transcription PCR (RT-PCR), real-time PCR and light upon extension PCR [230, 234, 251, 252]. Both standard RT-PCR and real time RT-PCR approaches for detection of influenza virus are widely deployed due to their high sensitivity [230, 240, 243, 252]. Moreover, due to no requirement of subsequent gel electrophoresis and imaging steps, RT-PCR is more practical for large numbers of samples [242].

The significant advantage of PCR-based techniques is a rapid detection normally in the range of hours, but which requires careful primer design and accurate temperature control to obtain sensitivities [224, 250]. The main drawback of the PCR-based method is that it may cause transcription errors during the amplification process as well as report false negative results in cases in which viral RNA copy numbers are below the threshold for detection [224, 242, 250]. Besides, PCR-based techniques may not be stable as applying with nonspecific stains, degrading nucleases, and cellular debris existing in clinical samples [253].

The advantage of “gold standard” identification is highly sensitive, and which also produces a virus isolates that can be used for identification of unknown virus subtypes or further analysis [240, 242]. However, the “gold standard” is time consuming, labor intensive, it requires specialized laboratory facilities and well-trained technical personnel, which may not be feasible when rapid results are required or when hundreds of samples need to be assessed [223, 244, 251]. Moreover, this approach may fail to identify AIV when a viral material is present in samples but the infectious virus is not because no virus will be amplified [242].

5.1.2.2. DNA detection

Advances in genomics over the past decades has made the mainstream techniques of AIV detection to transit from protein and culture-based techniques to nucleic acid testing assays [251]. The PCR-based technique is most commonly used so far, but it also holds many disadvantages as mentioned above. Therefore, direct DNA detection, especially hybridization of complementary DNA chains is preferable for recognition and monitoring of sequences belonging to AIV infectious diseases and has expanded exponentially in recent years [254, 255]. The benefit of direct DNA detection is not only because of its high sensitivity, but also of easy integration with other devices, which makes it a promising candidate for the development of an integrated, high-throughput and compact AIV biosensor [255-258].

There are plenty of methods for DNA sensing; traditional methods are based mainly on radio labeled system or optical detection using fluorochrome tagging, quantum dots or enhanced absorption of light by oligonucleotide modified gold nanoparticles [259, 260]. These indirect quantification methods require complex procedures and expensive instruments, which greatly limit their clinical application. To solve this problem, many emerging “label-free” approaches are adopted, which promise to offer high sensitivity, selectivity, and low-cost for the point-of-care detection of DNA hybridization, such as electrochemical detection, 1D nanostructure-based field-effect transistor/chemiresistor, etc. [24, 261-264]

1. Electrochemical DNA sensor

The electrochemical biosensors widely applied so far are based on the three-electrode system, which comprises a working, reference, and counter electrode. For the working electrodes, commonly used glassy carbon electrode (GCE) surface is modified by various nanostructures, such as graphene and carbon nanotubes [3]. These electrochemical biosensors are advantageous because of their high sensitivity and can be applied to detect specific binding of DNA [24].

2. FET/chemiresistor DNA sensor

FET/chemiresistor DNA sensors have been developed in recent years, which are very attractive because of their high sensitivity, minimized size and simple structure [258, 265-267]. Recently, there has been an increase in the application of one-dimensional nanostructures such as silicon nanowires [256, 268], conducting polymer nanowires [265, 269] and carbon nanotubes [31, 261, 270] as transducing elements because of miniaturization and low power consumption.

Fig. 5.2 depicts the configurations of FET/chemiresistor biosensors for electrical measurement in 1D nanostructures bridging two metal electrodes used as source (S) and drain (D). 1D nanostructure serves as the transducer which translates DNA hybridization events into a directly detectable electrical signal [6]. Compared to three-electrode electrochemical methods, this two-terminal FET/chemiresistor DNA sensors involve much simpler chemistry and easier setup. Fig. 5.2(a) shows the configuration of a chemiresistor-type biosensor, which has the simplest structure; its DNA-detection principle is based on the change in resistance as a response to the binding of target DNA sequence on the active nanostructures [6, 271]. By configuring a back gate under insulating layers such as SiO_2 and Si_3N_4 , the semiconducting 1D nanostructure can be made as back-gated field-effect transistors (Fig. 5.2(b)) [6]. Fig. 5.2(c) presents a schematic of ion-gated FET, not like chemiresistor and back-gated FET biosensors normally operated in air, which has been developed for operating in a liquid environment. In ion-gated FET, the gate electrode works as a reference electrode in contact with the solution.

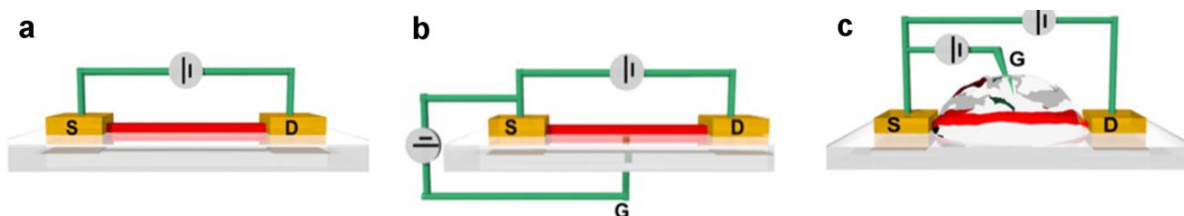


Fig. 5.2: Schematic diagram of electrical detection of biosensors reported by Chartuprayoon et al. [6]: (a) chemiresistor, (b) back-gated chemical field effect transistor, and (c) ion-gated field effect transistor.

With the development of nanotechnology, FET/chemiresistor biosensor is becoming more preferable than electrochemistry method, not only attributed to their low production costs and excellent sensitivity, but also because which can be directly incorporated into electronic circuits that holds a great potential for their integration with “lab-on-a-chip” microanalysis systems [6, 11, 256, 272-274]. Moreover, FET/chemiresistor biosensors are capable to perform direct quantitative measurements with no requirement of complicated external signal processing units [11]. However, the application of FET/chemiresistor biosensor has not been widely applied in clinic diagnostics yet because nanofabrication still has not be standardized [24].

5.1.3. Indirect detection techniques

Indirect detection techniques are also widely applied detection methods through detecting antibodies specific for the virus, including enzyme-linked immunosorbent assay (ELISA), electrochemical immunosensors and aptamer-based diagnostics.

5.1.3.1. ELISA

ELISA is a popular and commercially available analytic biochemistry assay, which has been widely used for the detection of serum antibody for more than a decade [275, 276]. In ELISA, an amount of antigen is firstly affixed to a surface; and then a specific antibody is applied which can bind to the antigen, this antibody is covalently conjugated to an enzyme; finally, a solution of the colorimetric enzymatic substrate is added, leading to a color change in the substrate [277]. ELISA is a rapid technique for the detection of AIV, but which lacks sensitivity, specificity, and can have high false positive rates [241, 244].

5.1.3.2. Electrochemical immunosensors

Different from the direct electrochemical biosensors, electrochemical immunosensors use antigens/antibodies as bio-recognition ligands for virus detection [278]. Huang et al. [278]

reported a sandwich-type electrochemical immunosensor by using silver nanoparticle-graphene as trace labels to quantitatively detect antigens of avian influenza virus H7 with a working range of $6 \times 10^{-3} \sim 16$ ng/mL. Miodek et al. [279] applied electrochemical immunosensor based on polypyrrole and ferrocenyl group as a redox marker for detection of PB1-F2 protein of influenza A virus from 5 to 1.5 mM.

5.1.3.3. Aptamer-based diagnostics

Aptamers, termed “chemical antibodies”, are artificial nucleic acid ligands in vitro based on systematic evolution of ligands by exponential enrichment [280]. Aptamers can bind to a wide range of target molecules, ranging from large molecules such as protein to small molecules like ATP, dyes, amino acids, etc., which have been investigated as an alternative of bio-recognition ligands in recent [281]. Wang et al. [281] applied DNA aptamers specifically binding to hemagglutinin proteins with concentrations varying from 2 to 40 $\mu\text{g/ml}$. Brockman et al. [282] reported a quartz crystal microbalance aptasensor to detect AIV H5N1 virus with a detection limit of 1 hemagglutinin units (HAU) and a detection time of 1 h.

As described above, there are many conventional laboratory methods as well as emerging DNA sensing methods, which can be applied to for detection and identification of AIV. Most commonly used detection techniques are still time-consuming, which require specialized laboratory facilities that greatly limits their application in clinical tests [222, 223, 283]. Among all methods described above, direct DNA hybridization biosensing holds plenty of advantages, including high sensitivity, label-free detection and easy integration with other portable devices [255-258].

Herein we report on the development of stable chemiresistor-type sensors based on nitrogen-doped MWCNTs for highly sensitive and rapid label-free detection of AIV H5N1 virus. Our sensor fabrication technology overcomes the difficulty of integration of CNTs into devices; relatively long horizontally aligned nanotubes directly connect neighboring interdigitated metallic electrodes, which can be fabricated on both rigid and flexible substrates.

5.2. Functionalization

The sensing mechanism of chemiresistor DNA sensors suggested previously by Star et al. [31] attributes the electrical conductance change to the electron doping by DNA hybridization on the CNT sidewall [270]. To detect the target DNA (DNA T) sequence, functionalization of CNTs with probe DNA is required. There are two common modification ways to bind CNT with probe DNA, characterized as covalent and non-covalent functionalization.

5.2.1. Covalent functionalization of carbon nanotubes

In covalent attachment process, carbon nanotubes are firstly acid-oxidized to form carboxylic acid groups on their surface; and then, the carboxylic acid groups are activated by N-ethyl-N'-(3-dimethylaminopropyl)carbodiimide hydrochloride (EDAC) and N-hydroxysuccinimide (NHS) [284]. The active carboxylic acid groups can bind with amino-modified DNA or proteins by undergoing nucleophilic substitution reaction [284].

However, acid-oxidation of carbon nanotubes is a tedious and time consuming process, which requires refluxing the reaction mixture in concentrated HNO₃ or acid mixture for over 10 h [285]. Moreover, oxidative treatment by using strong acid may also introduce defects into CNT lattice or even damage the structure of nanotubes, which has inferior effects on the electronic properties of nanotubes.

In this case, we adopt non-covalent functionalization way in this study to immobilized probe DNA on CNTs' sidewall.

5.2.2. Non-Covalent functionalization of carbon nanotubes

Single-stranded DNA (ssDNA) molecules are capable to non-covalently immobilized to the CNT sidewalls by allowing the ssDNA to wrap around individual CNTs via π -stacking interactions between the heterocyclic rings of the nucleotides and CNT structure [31, 286, 287]. Our sensing principle is based on the vibration in conductance of CNT device (inverse of resistance) attribute to the hybridization between complementary DNA T strands and the immobilized ssDNA on CNT sidewalls [287].

In Figure 5.3(a) device preparation and working principle of our chemiresistor-type DNA sensor are schematically presented. The first step depicts device fabrication when CNTs are placed between metallic electrodes. In the second step (functionalization), probe ssDNA molecules were non-covalently attached to the CNTs via π - π interaction between a honeycomb-like structure of nanotube sidewalls and the heterocyclic rings of the nucleotides [286]. The attachment of DNA probe to CNTs led to a dramatic increase of the device resistance, which is measured after rinsing and drying the device using the probe station (Figure 5.3 (c)). In the third step, Triton™ X-100 (Fig. 5.3(b)) was applied to block the uncovered sites on the CNT sidewalls that DNA probe did not occupy. Triton™ X-100 is a nonionic surfactant containing an aliphatic chain and a hydrophilic polyethylene glycol group (n=9-10) [31, 71], which can bind to nanotubes because of π -stacking interactions [71]. This was done to avoid non-specific binding of DNA target to CNT sidewalls in a similar way like DNA probe. A minor change of device resistance was associated with covering of CNTs with Triton™ X-100, measured in a dry condition. When a

target DNA solution was drop-casted in the DNA sensing experiment, step four, the target ssDNA molecules were hybridized with their complementary probe ssDNA molecules removing them from the surface of CNTs as the helical shape of resulting dsDNA is not optimal for π - π stacking type interaction. This effect was manifested by a decrease of device resistance (measured again after rinsing and drying) towards initial resistance value. This decrease of resistance depends on the concentration of DNA target in solution, namely, the higher concentration is the more DNA probe molecules are detached from the CNT sidewalls during 15 min of incubation. Repeating step 4 several times with increasing DNA target concentrations it was possible to determine the range of concentrations for which our sensing device can be used. It is worth noticing that for concentrations higher than the one at which complete detachment of DNA probe is achieved, no reliable sensing is possible. This is a specific feature of the sensing principle realized in presented sensing devices.

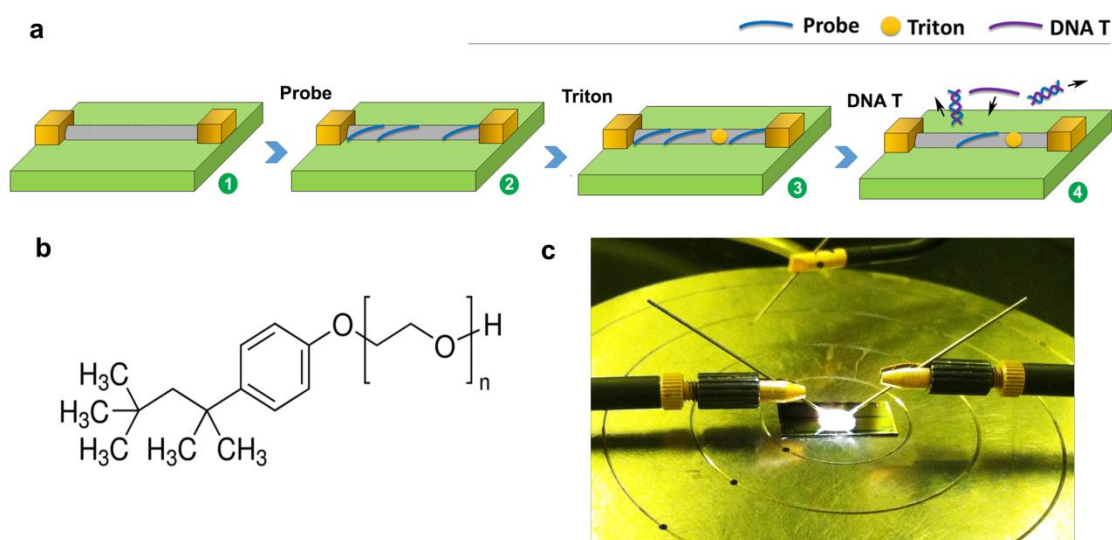


Fig. 5.3: (a) Schematic illustration of the CNT based chemiresistor-type DNA sensor functionalization and sensing steps. (b) Chemical structure of Triton™ X-100 [288]. (c) Image of the probe station during electronic characterization of a sensing device.

5.3. Results and discussion

5.3.1. CNT characterization and device layout

The chemiresistor-type sensors were fabricated using a standard microfabrication procedure, which has been described in section 2.3. After forming of horizontally aligned CNTs arrays on the target substrates, Cr/Au (3 nm Cr and 50 nm Au) interdigitated electrode fingers with an interspacing of 3 μm were deposited. Before use, all these as-fabricated devices were annealed at 200 $^{\circ}\text{C}$ for 15 min in vacuum for improving their electrical performance. Fig. 5.4 demonstrates that our CNT-based biosensor arrays can be fabricated on both rigid and flexible substrates, which are quartz, glass and Kapton® polyimide foil (from left to right).

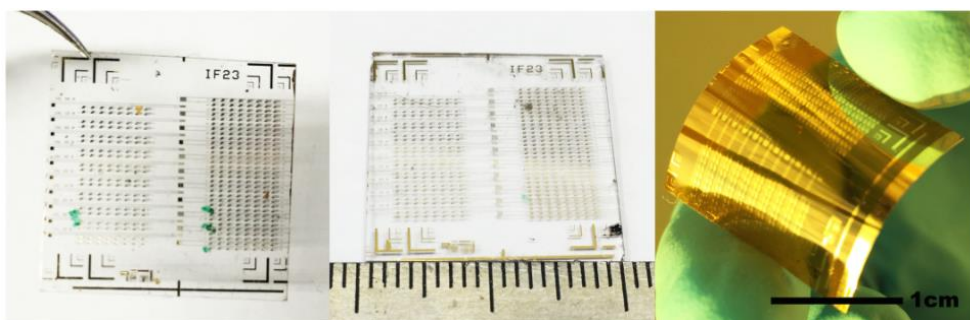


Fig. 5.4: Optical images of CNT chemiresistor biosensor chips each containing 400 sensing devices fabricated on various substrates (from left to right: quartz, glass and Kapton® polyimide film).

Cr/Au interdigitated electrodes were placed in the direction perpendicular to the alignment direction of N-MWCNT arrays so that nanotubes bridged the electrodes and acted as conducting channels. Figure 5.5 shows the channel region of the N-MWCNT based chemiresistor devices on quartz, glass and Kapton® polyimide films, respectively. In the inset in Fig. 5.5(a), horizontally aligned long N-MWCNTs are visible in the areas between the electrodes as shadows on the quartz substrate, showing nanotubes remain ordered after the whole fabrication process. It is apparent that N-MWCNTs were partially agglomerated in some areas due to excessive density. Some nanotubes were linked and overlapped with the neighboring tubes, hence forming a netlike structure. In the inset of Fig. 5.5(b), individual N-doped nanotubes are also visible as shadows between interdigitated electrodes. The surface density of N-MWCNTs in Fig. 5.5(b) is much lower than that in Fig. 5.5(a), leading to an individual distribution of nanotubes. As shown in the inset of Fig. 5.5(c), highly dense and uniform parallel array of individual N-MWCNTs with a

well-defined direction was covered by Cr/Au interdigitated electrodes on Kapton® substrate. Each nanotube is not in a contact with others and is long enough to bridge two electrodes as a conducting channel. As detailedly discussed in section 4.2.3, CNTs show a stronger adhesion to materials with dispersive surfaces, such as Kapton® polyimide film [207]. Therefore, it is possible to position uniform distributed and well aligned individual CNTs with contact printing onto a large area Kapton® substrate.

SEM images in Fig. 5.5 demonstrate that our synthesized N-MWCNTs are long enough to bridge neighboring interdigitated electrodes. According to Tortorich et al. [193], the length of carbon nanotubes plays a major role in the conductivity between two electrodes. Hecht et al. [202] demonstrated that the conductivity of a single-walled carbon nanotube network increases as the length of the carbon nanotubes increases. Through optimizing contact printing process, high-dense and uniform array of individual N-MWCNTs can be obtained on both rigid and flexible substrate. Compared with random nanotube network, well-aligned carbon nanotubes directly bridging source and drain electrodes are expected to offer better performance, because electrical current should not go through many nanotube-nanotube junctions [206]. Moreover, no dispersant or surfactant was applied for transferring and positioning of CNT arrays in this study, therefore, the conductivity of CNT based devices are not affected through inhibiting contact between nanotubes [179, 201, 202].

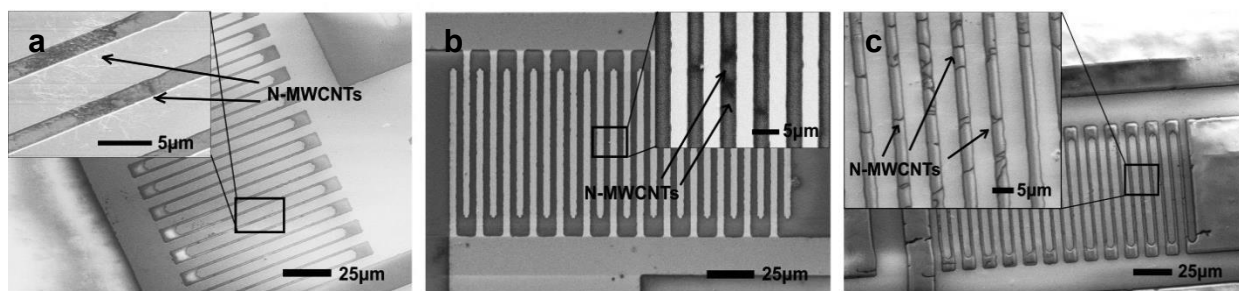


Fig. 5.5: Low-voltage SEM images of N-MWCNT based chemiresistor sensor device on (a) quartz, (b) glass, (c) Kapton® substrate; the higher magnified images in the insets show horizontally aligned N-MWCNT arrays bridging Cr/Au interdigitated electrodes. (The interspacing distance of the electrodes is of 3 μm .)

5.3.2. Functionalization and electrical characterization

The electrical characterization consisted of the I-V curves of the chemiresistor devices as shown in Fig. 5.6. It is known, that a single intrinsic MWCNT with a large tube diameter is metallic [187]. As shown in Fig. 5.6(a), the I-V curve before and after annealing do not show a linear behavior, the slopes of the I-V curves increase with the voltage between interdigitated electrodes. This can be explained by the lower density of states close to the Fermi level of CNTs, the energy bands of nanotubes accumulate with increasing of voltage, leading to a higher slope of I-V curves [289]. If zoom in the center part of I-V curves (see right panel in Fig. 5.6(a)), it is apparent that I-V curves still have certain slopes, demonstrating that the N-MWCNTs showed a metallic behavior in our experiments.

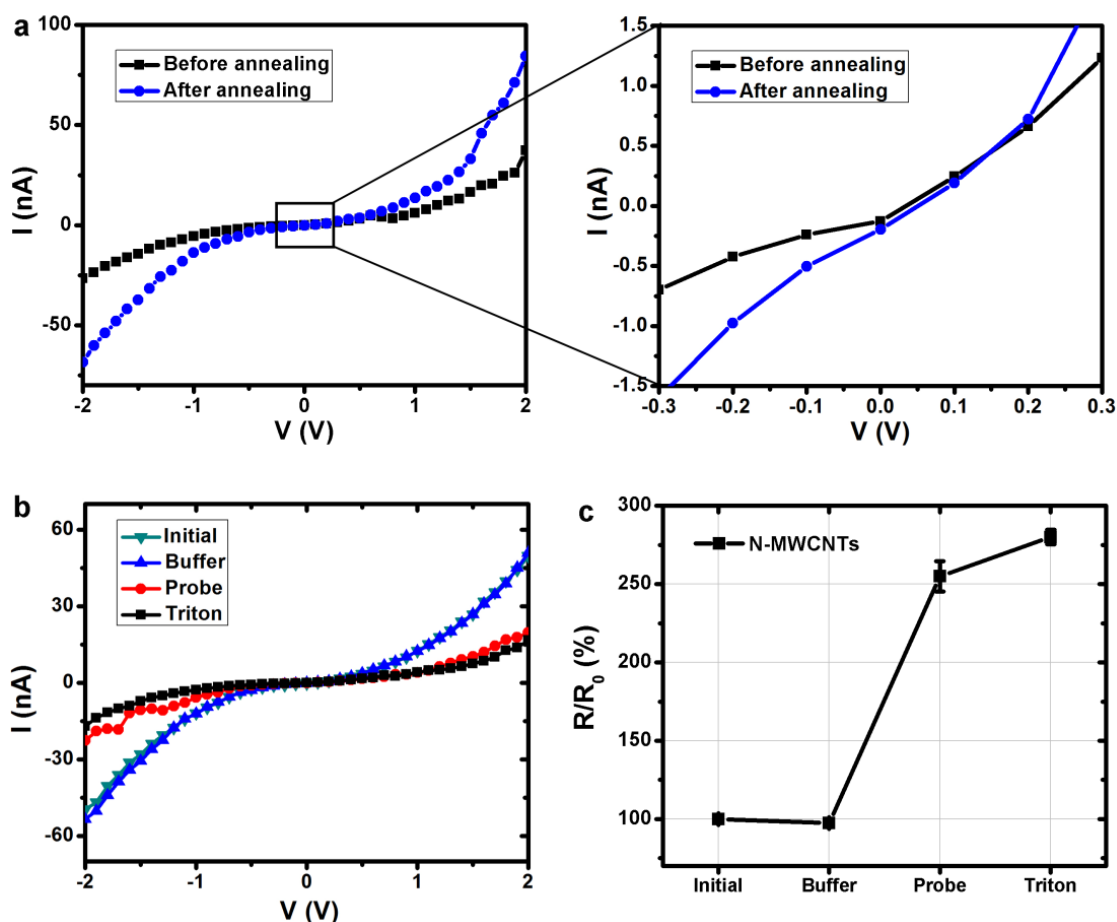


Fig. 5.6: (a) Typical I-V curves of N-MWCNT (N concentration of $\sim 8.3\%$) based chemiresistor DNA sensor before and after annealing in vacuum at $200\text{ }^\circ\text{C}$. (b) I-V curves of N-MWCNT based chemiresistor DNA sensor before and after functionalization steps. (c)

Resistance of the device before and after the functionalization experiments measured at voltage $V = 2.0\text{ V}$ for every step.

Annealing CNT devices in vacuum at high temperature can stabilize the contact between metal electrode and CNTs. It can be observed in Fig. 5.6(a) that the total current in the device increased after annealing in vacuum at $200\text{ }^\circ\text{C}$. The value of the resistance of the devices at 2.0 V decreased from 53.7 to $23.7\text{ }\mu\Omega$ after annealing.

Fig. 5.6(b) presents a typical I-V response of N-MWCNT based chemiresistor biosensors to each CNT functionalization step. In Fig. 5.6(c), the resistances of our sensor at $V = 2.0\text{ V}$ to each functionalization step are presented. The resistance at “Initial” step corresponds to the newly fabricated device before any functionalization (step 1 in Fig. 5.3(a)), which is of $40.1\text{ M}\Omega$. The initial values of device resistance varied from device to device and depend on the number of nanotubes bridging the electrodes (conducting channels) in each device as well as the electronic properties of active material. In order to estimate the influence of pure buffer on CNTs the devices were immersed into the buffer for 15 min, rinsed and dried. The measured resistance is marked “Buffer”. It is apparent that buffer had no effect on N-MWCNTs. When probe DNA was used for functionalization (step 2 in Fig. 5.3(a)), a significant increase of the resistance of N-MWCNT sensors was observed. The resistance of N-MWCNT sensors increased by 161%, exhibiting a strong influence of absorbed probe DNA molecules on carbon nanotube electronic structure. After that, the blocking of non-functionalized free areas of CNT sidewalls was performed with Triton™ X-100 (step 3 in Fig. 5.3(a)), which did not lead to significant changes in device resistances since 4-(1,1,3,3-Tetramethylbutyl)phenyl-polyethylene glycol are neutral organic molecules and they could not noticeably affect conductance of nanotubes.

5.3.3. Quantitative detection of target DNA

After treatment with Triton™ X-100, the sensors were prepared for DNA T sensing experiments. The sensing experiments (step 4 in Fig. 5.3(a)) were performed for all devices repeatedly with successively increasing concentrations of 0 pM , 2 pM , 20 pM , 200 pM and 2 nM . Fig. 5.7(a) shows the I-V characteristics of the functionalized N-MWCNT based DNA sensor after incubation it for 15 min each time in the solution of target DNA molecules with increasing concentrations ranging from 0 pM to 2 nM . Figure 5.7(b) shows the sensing response of N-MWCNT-based device to different concentrations as the ratio R/R_0 of the resistance after incubation with DNA T solution of given concentration to that with 0 pM concentration (in order to compare the sensing response of different devices with different initial resistances).

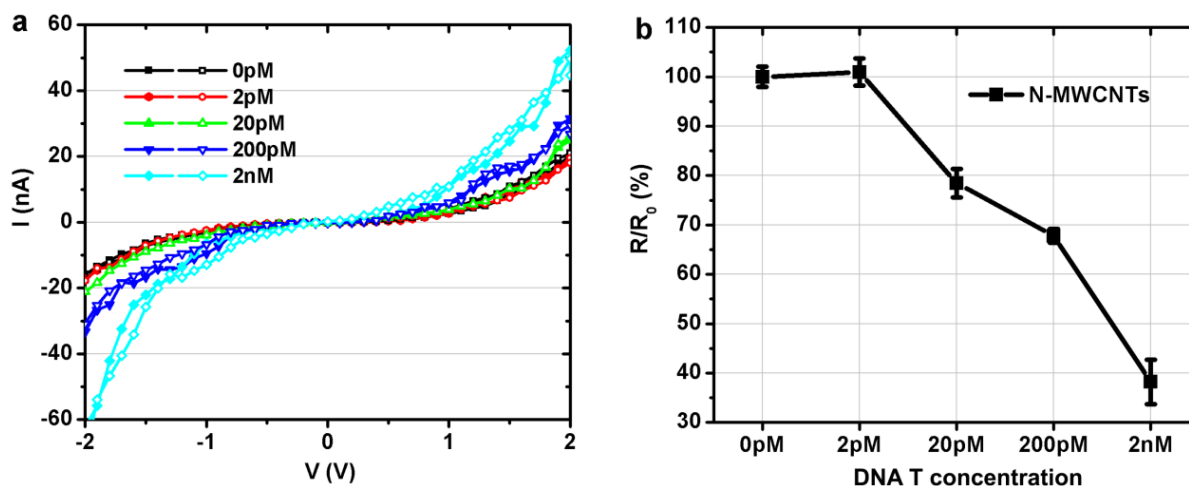


Fig. 5.7: (a) I-V curves and (b) resistance change (R/R_0) of N-MWCNT based DNA sensors (N concentration of 8.3at%) as the response to processing with increasing concentrations of DNA T from 0 pM to 2 nM ($V = 2.0$ V).

As shown in Fig. 5.7(b), it is apparent that there is no noticeable change of resistance for 2 pM DNA T. However, starting with a concentration of 20 pM, a significant decrease of device resistance was observed. As discussed above, such resistance reduction can be explained by the hybridization of complementary target DNA molecules with the probe DNA molecules and detachment of the latter from carbon nanotube sidewalls. The resistance change maintained a continuous downward trend in repeated sensing experiments with increasing of DNA T concentration up to 2 nM. Further increase of concentration and repeating the experiment with the same device led to an unreliable sensing response as two competing processes influenced the device resistance, namely detachment of DNA probe after hybridization with DNA target and attachment of access DNA T to the free places of CNT sidewalls left after removing DNA probe. As explained above, N-MWCNTs had metallic behavior, and no Schottky barrier was formed at CNT/lead interface. Therefore, the sensing response presented in Fig. 5.7(b) as well as the increase of the resistance after functionalization with DNA probe in Fig. 5.6(d) was solely based on the modulation of electronic states in N-MWCNTs as conducting channels by attachment or detachment of DNA probe molecules.

Chemiresistor DNA sensors based on nanostructured materials were demonstrated recently. A similar approach of measuring resistance change in dry condition was demonstrated recently in devices based on Si-NW [256]. There, the lowest reliably detected concentration was 40 pM of AIV H1N1 short DNA target sequences (for 30 min of incubation).

5.3.4. The influence of doping concentration on sensing behavior

To test the repeatability and compare the sensing performance and of our N-MWCNT based chemiresistor DNA sensor with different doping levels, a number of sensing devices based on N-MWCNTs with different amount of nitrogen as a dopant (N/C ratio varied from 6.1 to 9.3% according to XPS data) were fabricated and tested. No noticeable difference in sensing performance of these devices with respect to N doping level was found: different sensors show a similar decrease of relative resistance after exposure to DNA T as can be seen in Figure 5.8. The resistance of all devices starts to decline at a concentration of 20 pM and kept a systematic downwards trend with increasing DNA T concentration up to 200 pM. N-MWCNTs with higher N concentration (9.3% N/C ratio) present a more significant drop in resistance, indicating higher sensitivity. Normalized response S ($(|R - R_0|/R_0)\%$) was calculated, the highest sensitivity could reach 25% at 20 ppm of target DNA molecules. At concentration of 2 nM the effect of the attachment of DNA T to the empty places left on CNT sidewalls after previous sensing experiment with a lower concentration start to compete with effects from detachment of the rest of DNA probe that leads to a backwards trend (seen for N-MWCNTs with 6.1 % of N/C ratio). This means sensing at higher concentrations of DNA T, N-MWCNT-based sensor with the lowest N concentration was unreliable. Still, at lower concentrations of DNA T where the competing effect is absent or negligible, the decrease of relative resistance caused by hybridization of DNA T and DNA probe and the consequent detachment of the latter from CNT sidewalls is discernible for all sensors.

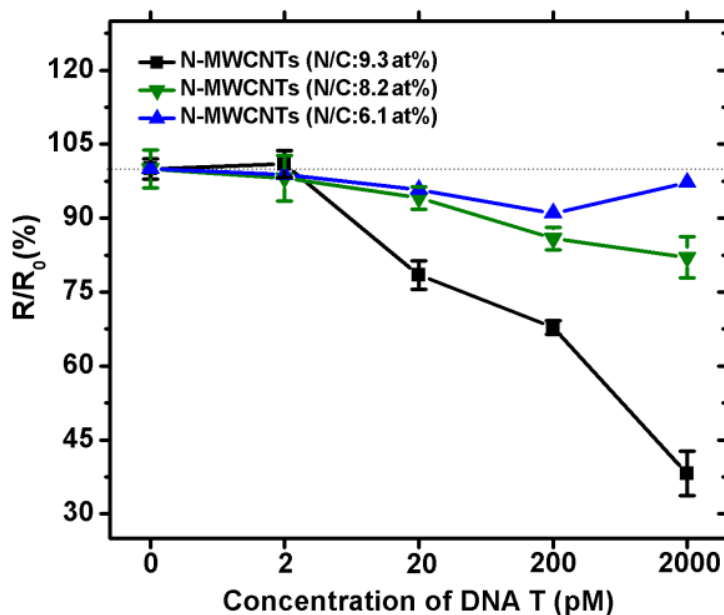


Fig. 5.8: Comparison of sensing responses of sensors based on N-doped MWCNTs with N/C ratio of 9.3 (square), 8.2 (down-triangle) and 6.1% (up-triangle). All sensors show similar downwards trend of resistance change R/R_0 for concentrations up to 200 pM. Increase of R/R_0 at 2 nM is attributed to the competing effect described in the text. Lines connecting points are used to guide an eye. ($V = 2.0 V$)

5.3.5. Selectivity

The selectivity of sensors to AIV H5N1 subtypes DNA sequences was assessed by testing sensing the response of devices functionalized with H5N1 DNA probe to H1N1 DNA target, a non-complementary sequence. The complete data on functionalization of N-MWCNT-based sensor with H5N1 DNA probe as well as sensing response to H1N1 DNA T with concentrations up to 2 μM are presented in Fig. 5.9. Error bars are calculated as the standard deviation for three measurements for each point, which are too small to be seen on the scale of the diagram. The sensor shows no noticeable resistance reduction (no sensing response) for all concentrations of H1N1 DNA T. These data confirm selectivity of our sensors to the H5N1 DNA T, which are complementary to DNA probe: DNA probe cannot be removed from the sidewalls of CNTs if hybridization with DNA T is not taking place, which is the case when non-complementary H1N1 DNA T is used.

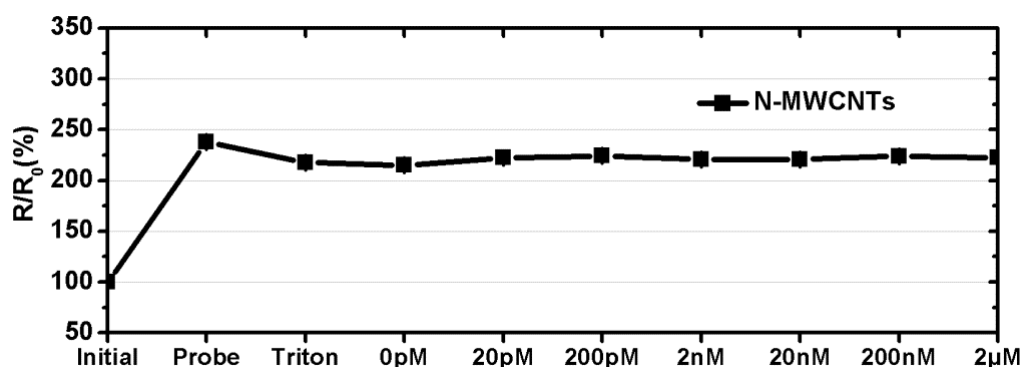


Fig. 5.9: Functionalization steps and sensing response of N-MWCNT-based chemiresistive sensor to non-complementary H1N1 DNA T. Lines connecting points are used to guide an eye.

AIV H5N1 virus exists in the blood as well as in nose or throat swabs of infected individuals, and the viral load in blood could be up to 10^5 copies per ml and in throat/nose swabs 10^8 copies per ml [290]. For detecting AIV H5N1, RNA must be extracted from the virus firstly, and then a reverse transcription to DNA should be performed. The concentration of 10^8 virus copies per mL corresponds to 0.2 pM, being recalculated as the concentration of DNA single-stranded sequences. However, the final concentration of the analyte can be still increased by reducing the volume since only a little droplet of the DNA solution (less than 0.1 μ L) is needed for sensing with our N-MWCNT-based sensors (20 to 200 pM), which can cover the whole area of interdigitated microelectrodes. Therefore, the amount of H5N1 DNA in a real sample is sufficient for the detection using proposed sensors without the need of amplification of DNA copies.

Further, it should be taken into account that real samples contain proteins typical to serum like immunoglobulin, serum albumin, transferrin, fibrinogen, and lysozyme, etc. However, previous reports showed for human α -thrombin hybridization DNA sensors, the presence of proteins may partially reduce the sensitivity with respect to the pure buffer solution but does not show any interference with the analyte assay [291, 292].

Table 5.1: Comparison of detection range of different sensors for AIV viruses.

Detection method	DNA	Sensing materials	Range	Ref.
Voltammetric detection	AIV H5N1	HS-ssDNA Probe modified gold electrodes	10–100 pM	[293]
Electrochemistry based on an ion barrier switch-off	AIV H5N1	Redox-active monolayers	1–10 pM	[294]
Voltammetric detection	AIV H5N1	Amino-ssDNA probe modified gold electrodes	10–100 fM	[295]
Electrochemistry	AIV H5N1	Probe modified single gold electrode	20–100 nM	[296]
Electrochemical impedance spectroscopy	AIV H1N1	Tubular nanomembrane	20 aM–20 pM	[254]
FET	AIV H1N1	Si nanowire	40–102 pM	[256]

Chemiresistor	AIV H5N1	N-MWCNT	20–2000 pM	This work
---------------	----------	---------	------------	-----------

Sensors for the detection of AIV single-stranded DNA based on different principles were demonstrated in recent years. The detection ranges are summarized in Table 5.1 and compared to the results of this work. As can be seen from this comparison, CNT-based chemiresistor-type sensors proposed here have a sensitivity, which is comparable to the majority of listed, however a poorer sensitivity compared to the sensor reported in ref. [295] and [254].

Chemiresistive DNA sensors based on carbon nanotubes were also demonstrated recently. Singh et al. [297] presented SWCNT-based sensor for the detection of human rheumatic heart disease based on hybridization of the target *S. pyogenes* single stranded genomic DNA (ssG-DNA) to its complementary 24-mer single-stranded DNA probe, and the estimated lowest detection limit was 22 pM. In their work, pristine SWCNTs (a mixture of metallic and semiconducting SWCNTs) were placed between gold electrodes and functionalized with covalently attached DNA probe sequences. The detection was based on the attachment of DNA T sequences on DNA probe, and the measurements were performed in a liquid medium. In our case, the measurements were done under dry condition, and the detection principle was based on the detachment of non-covalently bound DNA probe after hybridization with DNA T sequences. Such an approach has an advantage with respect to the detection in liquids in a simplified device fabrication since no microfluidic channels and no isolation of metallic leads were needed.

5.4. Conclusion

In this study, a flexible, highly sensitive, and label-free CNT based chemiresistor DNA sensors were developed for detecting DNA of AIV subtype H5N1. Compared to optical and other electrochemical methods, our CNT-based DNA sensors involve much simpler chemistry and easier setup, which can be fabricated on both rigid and flexible substrates.

N-MWCNTs with different N-doping concentrations functionalized with probe DNA served as active conductor channels, which translate DNA hybridization into a directly detectable electrical signal. According to our results, the complementary DNA T can be effectively detected with our biosensor for a concentration as low as 20 pM in just 15 min. Through comparing the sensing behavior of N-MWCNTs with different doping concentration, the N-MWCNT sensor with the highest N-doping concentration of 8.3at% (9.3% of N/C ratio) shows the highest sensitivity of 25% at 20 ppm. The detection limit of our sensor meets the requirement for detecting H5H1 DNA in a

real sample with no need of amplification of DNA copies. Due to the detection in dry conditions, no complex microfluidic channels and no isolation of metallic leads are required in our study. Therefore, our N-MWCNT based DNA sensor is a promising candidate for the fabrication of compact hand-held devices and applied in “point-of-care” microanalysis systems.

6. Performance of N-MWCNTs based gas sensor

In 2000, Kong [15] first demonstrated that semiconducting SWNTs integrated with FET can be applied as a fast and sensitive gas sensor at ambient temperatures. Since then, various groups have explored the potential of carbon nanotubes for gas sensing due to their specific chemical and physical properties. Although the scientific breakthroughs are numerous in this area, CNT based gas sensors still have certain limitations, like reproducibility, sometimes low sensitivity to analytes, lack of selectivity, irreversibility or long recovery time, etc. [11, 32, 298] To overcome these limitations, functionalization is often applied to alter the chemical nature of CNTs and thus enhance their sensing performance [112, 298, 299].

In this study, N doped multiwalled carbon nanotubes were applied as active materials for gas sensing. Firstly, a general overview of gas sensors based on CNTs was introduced, and then a systematic experimental study was presented in terms of the sensing properties of N-MWCNT based gas sensors to NH_3 and NO_2 .

6.1. Overview of CNT based gas sensors

CNTs have high surface area to volume ratio that is important for an enhanced sensitivity, high structural and chemical stability to be deployed in different environments, and can be subjected to versatile functionalization that is viable to imbue selectivity. All this makes them sensing materials with a high potential for the development of miniaturized and low-power gas sensors with high sensitivity and selectivity [11, 48, 69, 300].

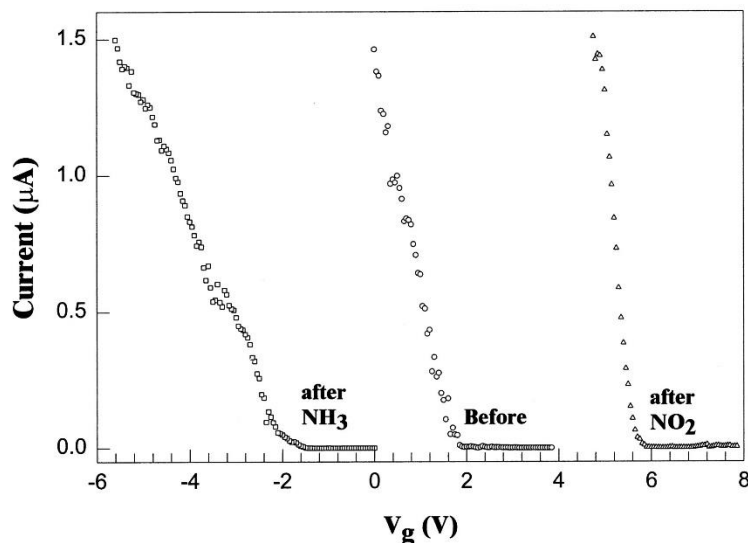


Fig. 6.1: Transfer characteristic change after exposure to NO₂ (triangles) and NH₃ (squares) of the SWCNT-FET gas sensor firstly reported by Kong et al. [15]

Kong et al. [15] firstly reported that single-walled carbon nanotube showed high sensitivity to NO₂ and NH₃ at room temperature. They used a single SWCNT as a transistor channel between two gold electrodes to fabricate a SWCNT based FET, which sensing property was monitored by changing the SWCNT-FET transfer characteristics, as shown in Fig. 6.1. The middle curve in Fig. 6.1 is the current versus gate voltage ($I-V_g$) curve before exposure, which presented p-doped semiconducting property [15]. After exposure, $I-V_g$ curve was shifted by -4 V exposed to NH₃, while in the contrast, presented a negative shift of $+4$ V under NO₂ exposure [15].

Besides carbon nanotubes, a large variety of 1D materials have been studied and applied for the gas sensing, including Si nanowires [301-303], semi-conducting metal oxides [34, 304, 305], and conducting polymers [306-308]. Usually, metal oxides require high operating temperatures (from 200 to 600 °C) in order to enhance their surface reactivity with respect to molecules of gas [309]. However, CNTs based gas sensors usually offer competing advantages in terms of room-temperature operation, lower power consumption, reduced size and good versatility [36, 300, 310]. Li et al. [69] fabricated SWCNTs gas sensors that can detect NO₂ as low as 44 ppb at room temperature, and Qi [311] reported that the multiple-SWCNT based FETs exhibited excellent sensitive to NO₂ in Ar.

SWCNT-FET is a very promising type for gas detection: not only the electrical properties of nanotubes are dramatically changed when exposed to the target gas analytes, but the gate voltage also can tune the conductance of CNTs leading to higher sensitivity [298]. However, pure semiconducting SWCNTs are very expensive and hard to be synthesized. MWCNTs have larger diameters than SWCNTs due to the multilayer tube structure, which can be synthesized at large scale with a relatively low cost [8]. MWCNTs usually exhibit more metallic behavior because of multi-layer structure [64, 112, 312], therefore, MWCNTs can only be integrated with chemiresistor-type devices. Compared with back-gated field effect transistors, chemiresistor processes inferior sensing performance but contains simpler chemistry and easier setup, no requirement of complex ancillary electronics.

To improve sensing performance of MWCNTs based chemiresistive gas sensors, functionalizing CNT sidewalls with specific materials was often applied. Penza et al. [313] reported that sensitivity of MWCNTs chemiresistors to NH₃ and NO₂ gases can be significantly improved when the surface of MWCNTs was functionalized with noble metal (Au, Pt) nanoclusters. Cui et

al. [112] reported that sensitivity of MWCNTs gas sensor can be increased by means of silver nanocrystal functionalization (from 2.8 to 9.0%) when exposed to 1% NH_3 .

Besides functionalization with metal nanostructures, a few experimental and theoretical studies indicated that doping CNTs with nitrogen atoms is capable to improve the sensitivity of CNT sensors. According to combined experimental and theoretical study by Adjizian et al. [106], N-doped MWCNTs (N concentration was 2.2at%) showed a better response to NO_2 and CO compared to pristine or boron doped multiwall carbon nanotubes at room temperature. Sadek et al. [20] also reported that N doped MWCNTs functionalized with Pt-Ni alloyed nanoparticles showed a fast response and recovery to H_2 gas, which can be explained by a combination of responses from the nitrogen-induced defects and the supported Pt nanoparticles. However, there are still very few data on gas sensing performance of N-MWCNTs to NH_3 and NO in literature.

6.2. Results and discussion

In this study, N-MWCNTs based chemiresistive devices were developed and applied as gas sensors for the detection of to NH_3 and NO at room temperature. The sensing mechanism of N-MWCNTs chemiresistor is based on the electrical resistance change attribute to charge transfer between CNTs and adsorbed analytes.

6.2.1. CNT characterization and device layout

The chemiresistor based on N-MWCNTs were fabricated using a standard microfabrication procedure, which has been described in section 2.3 in detail. CVD-grown N-MWCNT arrays were positioned directly on the substrates by contact printing, and then the Cr/Au (3 nm Cr and 50 nm Au) interdigitated electrode fingers with an interspacing of 3 μm were deposited across the N-MWCNT arrays. The gas sensing devices can be deposited on various substrates, such as silicon, quartz, and glass (see Fig. 6.2).

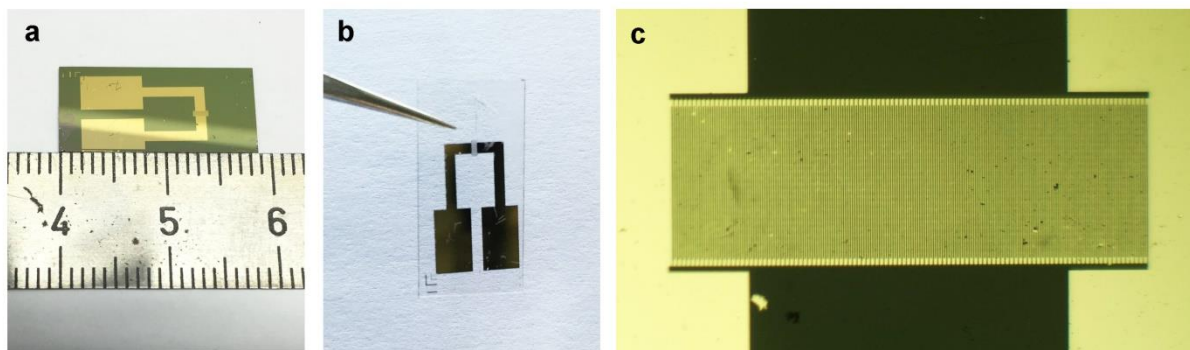


Fig. 6.2: Photos of gas sensing chemiresistor devices fabricated on (a) Si/SiO₂ and (b) glass substrates. (c) Optical microscope image of interdigitated electrodes of the gas-sensing device fabricated on a glass substrate.

Several researcher groups [314, 315] reported gas sensors made with nanotubes, which were placed on top of electrodes. In these cases, nanotubes may only weakly adhere to the electrodes that may lead to a reduced sensitivity of the sensors [316]. SEM images of the interdigitated-electrode area of our N-MWCNT based devices are presented in Fig.6.3: the nanotubes are lying under the electrodes and are in a tight contact with the electrodes on the glass substrate. It has to be noticed that N-MWCNTs were not subjected to any post chemical or thermal treatment after their synthesis.

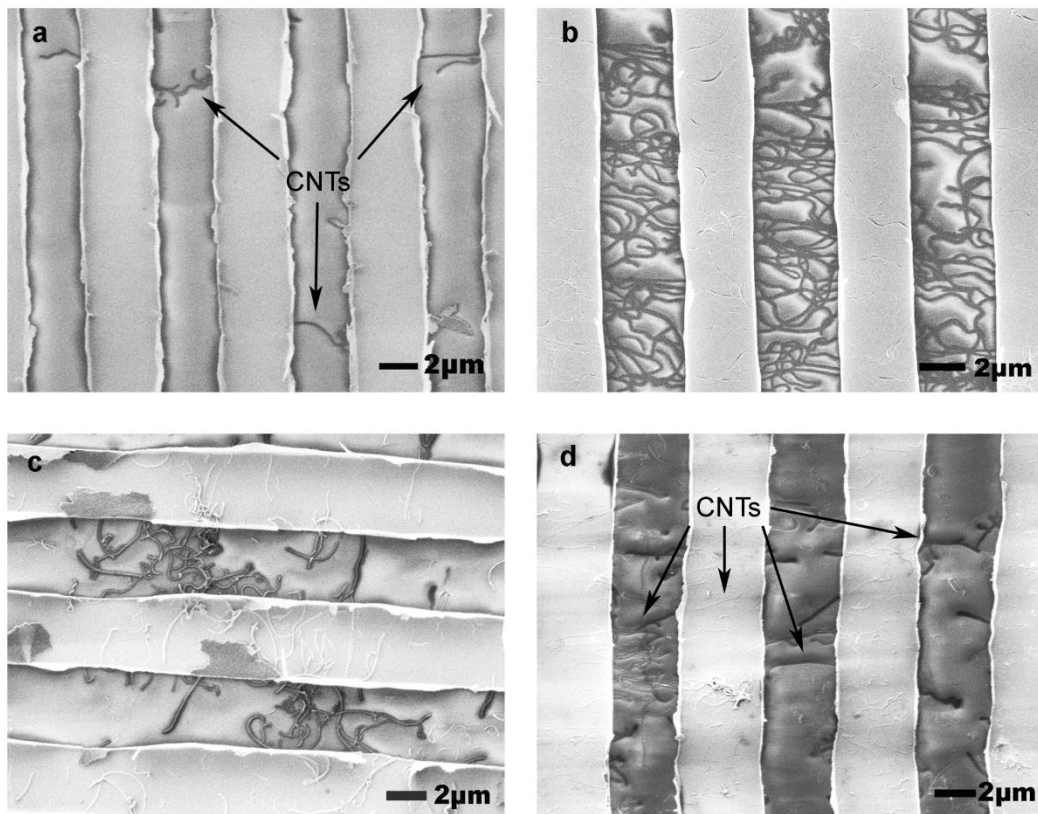


Fig. 6.3: SEM images of interdigitated-electrode areas of N-MWCNT based gas sensors on glass substrate with N concentration of (a) 8.3, (b) 7.3, (c) 5.5 and (d) 5.0at%.

Horizontally aligned N-MWCNT arrays lie under the electrodes with an interspacing distance of $\sim 3 \mu\text{m}$.

6.2.2. Annealing effect

In our experiments, all the devices were annealed at $200 \text{ }^\circ\text{C}$ in vacuum for 15 min after N-MWCNT deposition to improve the electrical contacts. The electrical characterizations consisting of the I-V curves of the chemiresistor devices before and after annealing are presented in Fig. 6.4. It can be seen that the source-drain current values of those two devices present inevitable differences. Because N-MWCMT growth in terms of their morphology, diameter, wall numbers, etc. as well as the number of transferred nanotubes is still difficult to exactly control, the conductivity of devices based on the CVD-grown N-MWCNT cannot be reproduced exactly even though they were fabricated following the same protocol. Additionally, a number of nanotubes bridging electrodes also greatly influences the conductivity and their positioning on the target substrate cannot be controlled accurately even by contact printing process. A similar report can also be found in ref. [317], in which SWCNT dispersion was drop-casted between the interdigitated electrodes for fabricating devices.

According to Fig. 6.4, the resistance of devices with different N doping concentration of 8.3 and 5.0at% decreased in general after annealing, indicating annealing stabilized the contact between metal electrodes and carbon nanotubes. The slope of the lines in the insets of the four I-V curves indicates that the N-MWCNTs all show metallic behavior, which is consistent with our previous reports in the section 5.3.2. Similar to pristine MWCNTs, the contact between the N-MWCNTs and the gold electrodes is Ohmic. Due to defective polygonal ends introduced through N-doping, only the outermost shell of N-MWCNT is responsible for the electrical transport (see section 1.3.3). As the Schottky barrier between the N-MWCNT and the electrodes was minimized, the main mechanism of sensing in our devices is a direct charge transfer between the N-MWCNTs and adsorbed gas molecules.

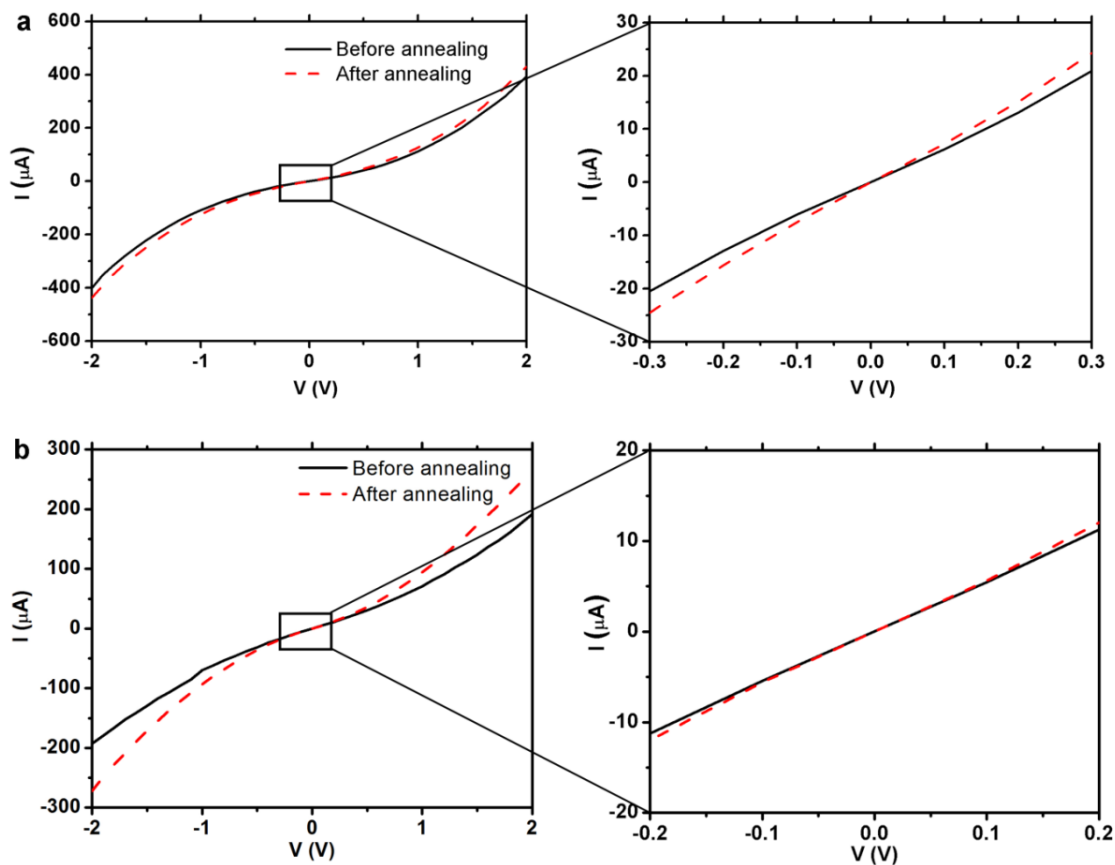


Fig. 6.4: I-V curves of chemiresistor devices based on N-MWCNTs with varying N doping concentration of (a) 8.3 and (b) 5.0at% before and after annealing at 200 °C. The insets are the magnified range at the center area of the I-V curves.

6.2.3. Exposure to ammonia

The real-time testing of gas sensing performance of the N-MWCNTs with the N concentration of 5.5at% was firstly carried out in the presence of different concentrations of NH_3 in the range from 1.5 to 50 ppm at room temperature. After the device was placed into the gas exposure chamber, a constant flow of 2 L/min of N_2 was introduced inside. In the meanwhile, the real-time current between two electrodes of the devices was monitored under a constant voltage of 0.1 V until the stable signal was obtained (after 50 min). Then, NH_3 flow was admixed to the N_2 flow in the chamber. As shown in Fig. 6.5(a), real-time sensing response was detected by monitoring and recording the resistance changes (R/R_0).

One can notice that the device resistance began to grow after exposure to NH_3 for 9 min and the resistance value of the N-MWCNT device presented a continuous increasing tendency with a stair step growth of NH_3 concentration from 1.5 to 50 ppm, this may be attributed to NH_3 molecule adsorption on the sidewalls of carbon nanotubes. NH_3 can be considered as a reducing gas, which donates electrons to CNTs, resulting in the holes depletion and thus increase the resistance of nanotubes [30, 318, 319]. After a cycle of analyte exposure, recovery was tested under pure N_2 flow, however, no apparent recovery was observed within 15 min. After 140 min exposure, the enhancement of the resistance value became slow, indicating that the gas sensing device reached saturation.

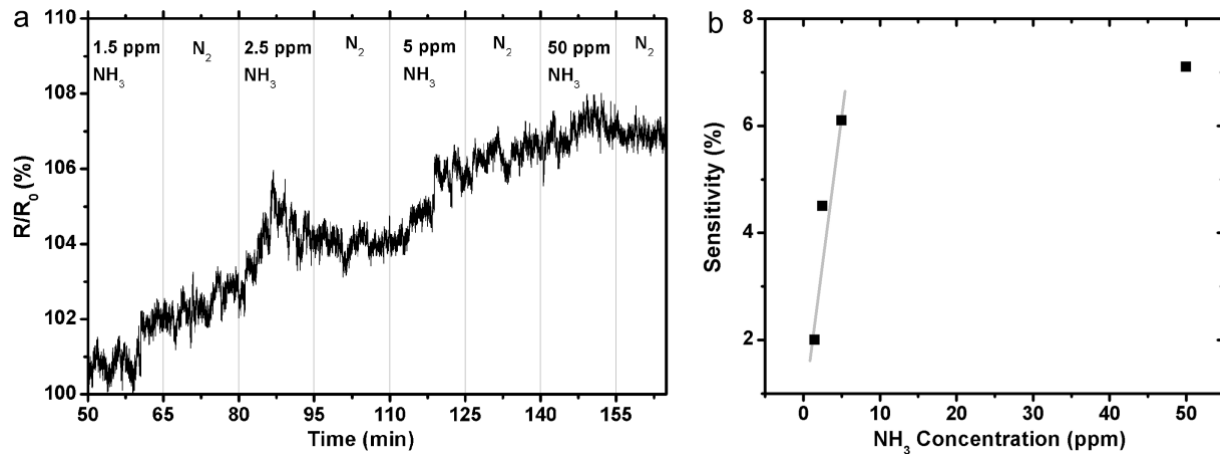


Fig. 6.5: (a) Real-time resistance changes ($(R/R_0)\%$, $R_0 = 1.54 \text{ k}\Omega$) of the N-MWCNT based gas sensor with nitrogen concentration of 5.5% as the response to increasing concentrations of NH_3 ranging from 1.5 to 50 ppm ($V = 0.1 \text{ V}$); exposure times are delimited by the vertically lines with the corresponding concentration. (b) Sensitivity ($S = |R - R_0|/R_0 \times 100\%$) of the device as a function of NH_3 gas concentrations.

Fig. 6.5(b) presents the sensitivity of the device ($S = (|R - R_0|/R_0) \%$) as a function of NH_3 concentration. The sensitivity of the device shows a linear growth at concentration 1.5, 2.5 and 5 ppm of NH_3 , and reaches 7.1% at 50 ppm. According to Nguyen [320], the sensitivity of resistive gas sensors based on MWCNTs coated with Co nanoparticles was 1.5% for a NH_3 concentration of 70 ppm with a response time of ~ 2 min.

To test the stability and repeatability of the N-MWCNT based gas sensor, other exposure experiments were carried out by applying different samples and exposing them to higher concentrations of NH_3 ranging from 200 to 1000 ppm. The images of a real-time response of N-MWCNTs with different N doping concentration ratios (5.5% and 8.3%) to varying NH_3 concentrations are shown in Fig. 6.6(a) and (c). A similar trend of resistance change was observed in Fig. 6.6(a), which started to grow at 32 min and maintain an upward tendency up to 70 min, followed by saturation. Fig. 6.6(b) presents the sensitivity value of N-MWCNTs (5.5%) as a function of NH_3 concentration, which is approximately 3% at 500 ppm and 4% at 1000 ppm. It can be observed that the sensitivity of N-doped nanotubes in this sample is lower than that shown in Fig.6.5 with the same doping level (5.5%), because two different and independent devices were used in these two sensing tests. As discussed above, the structure of the fabricated device is more complex than the CNT itself, resulting in many inevitable differences existing between different devices, such as CNTs structure, amount, and/or distribution of conduction channels, etc. Therefore, variation in resistance of two independent samples shown in Fig. 6.5 and Fig. 6.6 are not comparable.

Interesting, the resistance of N-MWCNTs with the highest doping level (8.3%) shows a declining trend under NH_3 exposure with increasing concentrations, as shown in Fig. 6.6(c). The resistance started to decrease from 32 min at 500 ppm, followed by a slight recovery in pure N_2 , which further decreased by 0.1% at 1000 ppm. A similar result was reported by Antal et al. [321], that N-MWCNTs with a N concentration of 2at% presented an opposite trend of sensing response to NH_3 compared to pristine MWCNTs, the resistance of which decreased by 4% after exposure.

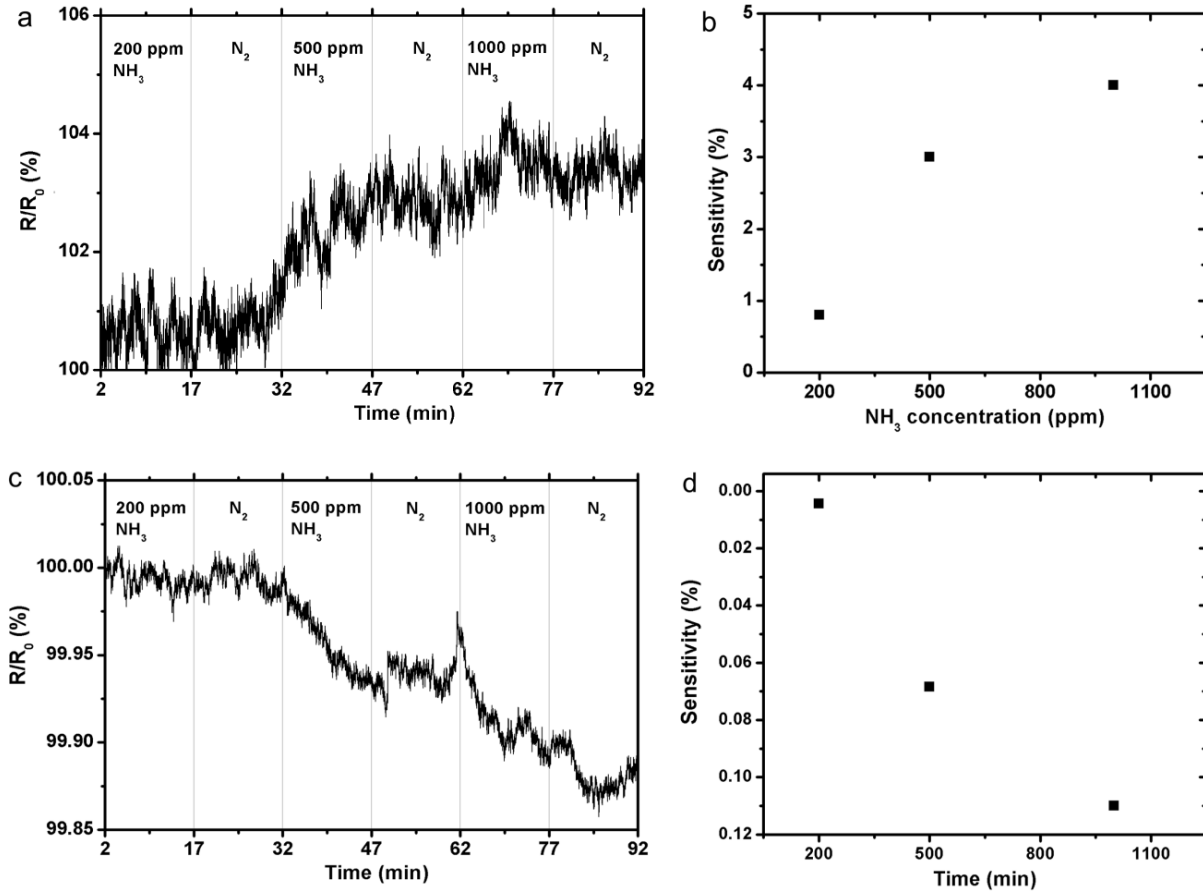


Fig. 6.6: Real-time sensing response (R/R_0)% of N-MWCNT based resistive device with a N concentration of (a) 5.5 and (c) 8.3% upon exposure to NH_3 gas at 200, 500 and 1000 ppm at room temperature ($V = 0.1 \text{ V}$); exposure times are delimited by the vertically lines with the corresponding concentration. (b) The dependence of sensitivity ($|R - R_0|/R_0 \times 100\%$) of N-MWCNTs with N concentration of (b) 5.5 and (d) 8.3% on increasing concentration of NH_3 gas.

The sensing mechanism of chemiresistor CNT based devices is based on the charge transfer between adsorbed gas molecules and CNTs leading to the resistance variation [70, 112, 298, 300, 318]. In our experiments, the resistance change of N-MWCNTs with a lower doping level (5.5%) showed a similar increasing trend with pristine CNTs in previous reports, but that of the N-MWCNTs with a higher N concentration (8.3%) presented an opposite downward trend. As discussed in section 1.3.3, pristine CNTs present a p-type behavior in the air because of oxygen adsorption, in which holes are the majority carriers. Therefore, carbon nanotubes accept electrons from reducing gases (e.g., NH_3), leading to holes depletion and the increase of

resistance. Similar results were also reported previously: Kong [15] reported that resistance of metallic SWCNT-FET sensor was increased under the exposure to NH_3 ; Wang [316] also studied the conductivity of MWCNT chemiresistor sensors at room temperature, which was decreased from 8 to $2.5 \mu\text{AV}^{-1}$ after exposure to 1% of NH_3 . As mentioned in section 1.3.3, Fermi level of N-doped nanotube will be shifted up because of the N incorporation into CNT lattice. If N doping is high enough to shift the Fermi level up to conduction band, the nanotube will display an n-type behavior; conversely, it maintains a p-type behavior. Therefore, the reverse sensing response of N-MWCNTs with a higher doping level (8.3%) may be explained by the effect that n-type nanotubes get more electrons into their conduction bands from adsorbed NH_3 molecules that leads to an increase of conductivity or a decrease of resistances (see Fig. 6.6(c)).

6.2.4. Exposure to NO

One finds very few data reported on sensing performance of N-MWCNTs on NO or NO_2 , but many studies focus on SWCNTs used for NO detection. Hoa et al. [322] applied porous single-wall carbon nanotube films for NO detection, and the sensitivity of such sensor was 5% under an exposure of 40 ppm NO at room temperature. Yu et al. [323] also reported 1% SWCNT/TWEEN-TEOS composite applied as a sensing material to detect 1000 ppm NO at room temperature with a response time of 5 min.

In this study, the room-temperature sensing performance of gas sensors based on N-MWCNTs with different doping levels (5.0 and 8.3%) under exposure to 1000 ppm NO was investigated. As shown in Fig. 6.7, two N-MWCNT devices with different N-doping concentration both exhibited a decline in response R/R_0 (%) upon exposure to NO. NO is a type of “electron-acceptor” gas, CNTs withdraw electrons to adsorbed NO molecules and leads to an opposite sensing behaviors compared to NH_3 . In Fig. 6.7(a), the resistance value of nanotubes dropped rapidly after 2 min exposure, which maintained for 3 min followed by the equilibration. Due to extremely large initial resistance ($15.3 \text{ M}\Omega$) of this device, the highest sensitivity ($|R - R_0|/R_0$)% reached 72%. The response of N-MWCNTs with N concentration ratio of 8.3% in Fig. 6.7(b) showed a similar tendency with a rapid drop after 3 min exposure, and the sensitivity of this device was of 3.4% approximately. Compared to the response of N-MWCNT based gas sensors to NH_3 , our sensors presented a lower resolution under exposure to NO.

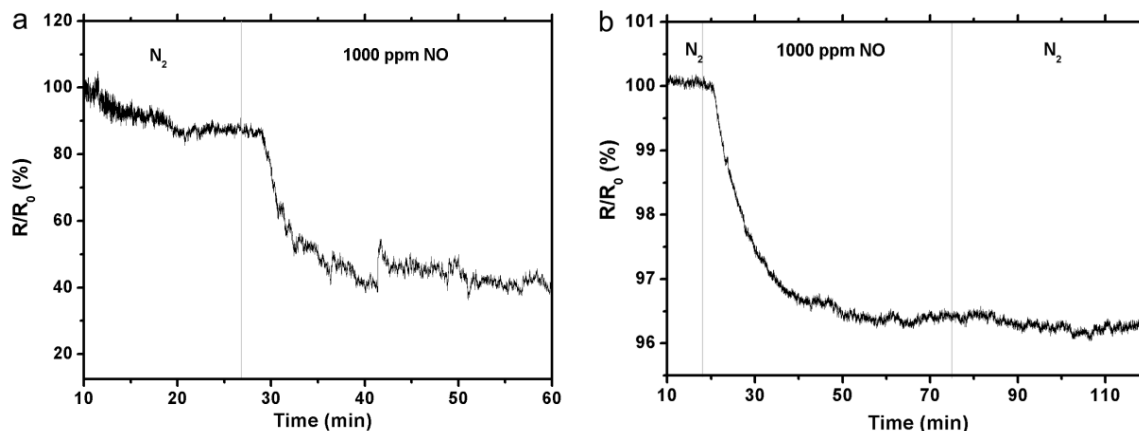


Fig. 6.7: Real time response (R/R_0)% of devices based on N-MWCNTs with different N-doping of (a) 5.0 and (b) 8.3% to 1000 ppm NO at a constant voltage of 0.1 V.

After exposure, the device did not show an apparent recovery over 40 min under pure N_2 flow. According to Zhang [298], the binding energy of the analytes to pristine CNT is usually large so that the analytes only slowly desorb from the CNTs after the sensor is exposed to an analyte-free atmosphere. To accelerate the recovery process of CNT sensors, an external energy source was often implemented for rapidly desorption by lowering the adsorption energy barrier, which can be achieved by heating to high temperatures (~ 200 °C) or illuminating by ultraviolet light [298, 324]. However, this also requires higher energy consumption [8]. Additionally, Dai [45] and Valentini [325] also reported that NH_3 is weakly physisorbed on nanotubes and can be removed by simple pumping in a vacuum, while NO_2 molecules have a strong physical adsorption with CNTs and do not desorb at significant rates at room temperature.

6.2.5. Applications in environmental and human breath monitoring

Ammonia is a colorless noxious gas with very pungent odor, which occurs naturally in the environment and also can be emitted by industry, agriculture or transport. If the concentration of NH_3 in the air exceeds 25 ppm, it can be detected by smell; and if the concentration is over than 500 ppm, NH_3 is immediate hazard to life [326]. NO is also a colorless toxic gas, and its permissible exposure limit is 25 ppm [327]. Therefore, the detection limits should reach to 20 ppm and air exposure effect should be carefully considered if applying NH_3 and/or NO gas sensors for environmental monitoring.

The working mechanism of our gas sensor lies in the electrical resistance variation due to gas molecule adsorption, so the sensor response is usually determined by the nanotube-molecule interaction. Most gas molecules studied (with exception of NO, NO_2 and O_2) are charge donors,

while O₂, NO and NO₂ are charge acceptors. Air mainly consists of nitrogen, oxygen, CO₂, Ar and H₂O vapor. Jijun et al. [328] calculated the adsorption of various gas molecules (NO₂, O₂, NH₃, N₂, CO₂, CH₄, H₂O, H₂, Ar) on SWCNTs using first-principles methods, and they found that the effects from most gas molecules in the air (i.e. N₂, CO₂, H₂O) are relatively weak, except O₂, which is an electron acceptor and makes all nanotubes p-type conductors. Wang [70] also reported that gas molecules like CO and water could not be adsorbed on nanotubes surface. However, oxygen has significant effects on nanotube resistance [329]. Peng et al. [330] studied NH₃ sensing mechanism and experimentally confirmed that NH₃ adsorption on CNTs surface can be facilitated by oxygen atoms adsorbed on the nanotubes from surrounding environment. They degassed the adsorbed oxygen by annealing and tested the devices in pure nitrogen, and they found that the device became insensitive to NH₃. According to Andzelm [331], pre-dissociated oxygen atoms can reduce the adsorption barrier for NH₃ on a defective CNT and enhance the charge transfer rate, thus improving the sensitivity of CNTs to NH₃. On the other hand, Valentini et al. [332] reported the response of CNTs to NO can be decreased after oxidizing in the air at 300 °C, but they supposed that the reduced sensitivity was mainly attributed to structure modification induced by annealing rather than oxygen effects. There are not much data reported the influence of oxygen on the sensing performance of CNTs on NO, so this question is not fully clarified yet.

Besides environment monitoring, highly sensitive and selective NH₃ and NO gas sensors also have potential to be applied for point-of-care testing through analyzing exhaled air. As a simple and fast medical diagnostic testing, PoCT is more effective and may play an increasingly important role in the future. According to the composition of human breathing listed in Table 5.5 [333], mouth-exhaled ammonia concentrations for humans is around 1 ppm, which requires gas sensors with a high sensitivity and a high resolution for NH₃ detection. Our N-MWCNTs have a small diameter and large surface area, and present a good sensitivity to NH₃ and NO at room temperature, but also face many disadvantages, such as poor sensitivity to low analyte concentration and reduced recovery ability. Besides, the selectivity of the gas sensors to these two gases at ambient conditions and for real exhaled air has not been clarified yet. Therefore, substantial research efforts are still needed to make CNT based sensors meet the requirement of environmental monitoring and even rapid PoCT for breath analysis.

Table 6.1: Composition of human breathing [333].

Gas	Inhale	Exhale
Nitrogen	78.62%	78%
Oxygen	20.84%	13-16%
Argon	0.96%	1%
Carbon Dioxide	0.04%	4-5.3%
Water Vapor	0.5%	5%
Hydrogen, Carbon monoxide	-	Several ppm
Ammonia	-	1 ppm
Acetone, Methanol, Ethanol	-	1ppm (unless ethanol)

Note: -, the concentration is so low that it can be neglected.

6.3. Conclusion

In this chapter, CVD-grown N doped multi-walled carbon nanotubes were integrated into chemiresistor nanodevices and applied for the detection of NH_3 and NO at low concentrations. Our investigations showed that N-MWCNT based chemiresistor-type devices are sensitive to both reducing gas NH_3 and oxidizing gases NO at room temperature. The response time of N-MWCNTs can reach several minutes, but a poor recovery was observed after introducing pure nitrogen flow at the same temperature.

7. Summary and outlook

7.1. Summary

This study gave a comprehensive picture of a compact, stable, and low-cost chemiresistor chemical sensor platform utilizing nitrogen doped multi-walled carbon nanotubes, which began from initial materials synthesis, integration and device fabrication, and up to the demonstration of their final application. Every single technological step was developed and optimized by us, meaning that the whole process could be accurately controlled thus making the results more reliable and repeatable. Additionally, we simplified the entire synthesis, fabrication and detection process so that one integrated cycle of the work, from synthesis to application, can be completed within two days that opens a prospect towards large-scale commercial applications of CNT-based chemical sensors in future.

In chapter 3, we reported the synthesis of vertically aligned N-MWCNTs with a varying N-doping concentration from 5.0 to 8.3 at% (N/C ratio: 5.6% to 9.3%) on the Si/SiO₂ substrate via chemical vapor deposition method. We confirmed that varying N-containing source could effectively control the nitrogen concentration incorporated into CNT lattices. The variation of nitrogen content in the carbon framework could significantly alter the morphology and electronic structure of certain nanotubes by introducing structural deformations, which provides a possibility to further tailor their sensing behavior. Moreover, we found that N incorporation greatly affects the nanotube growth: a higher content of N source mixed with ethanol leads to a lower growth temperature and higher concentration of N in nanotube lattice decreases the yield of CNTs as well as prevents crystalline CNTs growing. According to XPS analysis, the presence of three types of N incorporation in carbon matrix was confirmed, which are pyridinic, pyrrolic and quaternary nitrogen. The amount of these three forms can also be controlled through adjusting N-source concentration.

In chapter 4, we have developed a high performance, dry and low-temperature processing for transferring and patterning highly-aligned multiwall carbon nanotubes. Direct contact printing method was applied for scalable transfer of highly dense parallel arrays of N-MWCNTs onto a large area of target substrates. This method can successfully avoid the need of dispersing and sonication of nanotubes, which is not only beneficial for preserving structural and electronic properties of nanotubes, but also can avert the “coffee ring” effect. Many efforts have been made on the scalable positioning of N-MWCNTs, and results show that the surface coverage with printed N-MWCNTs can be varied from few tubes per square micron to a multilayer N-MWCNT film, which makes fabrication of CNT-based devices more controllable and reliable. In addition, we have demonstrated that both rigid and flexible substrates can be applied as target substrates,

including Si/SiO₂, quartz, glass and Kapton® polyimide foils. The way to enhance the attractive interaction between CNTs and various substrates with specially designed surface modifications that improved the performance of the direct contact-printing method was also presented in this chapter.

In chapter 5, we discussed flexible, sensitive, and label-free N-MWCNT based chemiresistive DNA sensors applied for detection DNA of AIV subtype H5N1. Compared to optical and other electrochemical methods, our sensors involve much simpler chemistry and easier fabrication and sensing setup. N-MWCNTs with different N-doping concentrations functionalized with probe DNA served as active conducting channels, which translate DNA T hybridization events into a directly detectable electrical signal. Modulation of Schottky barrier was not present in our N-MWCNT based devices, the sensing response relies solely on varying charge transfer of probe DNA molecules absorbed (or desorbed) on the sidewall of carbon nanotubes. The results show that the complementary DNA T at the concentration as low as 20 pM can be effectively detected with our sensors in just 15 min with the highest sensing response of 25%. Our N-MWCNT based DNA sensors hold the advantage of small size, flexibility, low-cost, easy integration with other, in particular portable devices which makes it a promising candidate for the development of an integrated, high-throughput and compact AIV biosensor for “point-of-care” diagnostics.

Besides the application for biosensing, preliminary investigations on gas sensing response of N-MWCNT based chemiresistor to reducing/oxidizing gases NH₃ and NO were reported in chapter 6. N-MWCNTs showed a bit lower sensitivity (especially in a range of several ppm concentrations) and recovery compared to semiconducting SWCNTs when applied as active materials for innovative gas sensors at room temperature. However, we validated that N-MWCNTs have a definite response in only several minutes when exposed to NH₃ and NO.

7.2. Remaining issues and outlook

A number of scientific breakthroughs have been recently achieved in the field of carbon nanotubes research and applications; however, there are still a lot of significant issues which require being further explored. One of the main issues is the large-scale production of carbon nanotubes in a controlled way in terms of chirality, alignment, diameter, length as well as predetermined electronic and chemical properties. This bottleneck greatly limits their commercial applications and thus makes the CNT sensors to remain at a proof-of-concept stage. To date, the concept of “cloning” SWCNTs has become increasingly attractive as a breakthrough approach, which uses open-ends of SWCNT fragments as “seeds/catalysts” to clone “new/duplicate” SWCNTs from the parent segments via an epitaxial growth mechanism [334]. This method does not need commonly used metal catalyst and can precisely control the

diameters and chirality of SWCNTs, meaning that selective production of pure semiconducting (or metallic) SWCNTs is possible. However, the yield of cloning is relatively low to date, which still requires a wide range of fundamental studies and technological developments.

Apart from such advantages like operation at room temperature, low power consumption and high sensitivity, CNT based gas sensors still face many problems. Application of SWCNTs with higher sensitivity is still hindered by their high prices, while available MWCNTs even functionalized still present low sensitivity and long response time. The selectivity of CNT-based sensors still needs to be improved, the response/recovery time requires to be decreased, and the stability in performances needs further improvement. In addition, nanotube conductance is also very sensitive to a variation of environmental conditions (moisture, temperature, gas-flow velocity), and molecule chemisorption could cause irreversible changes in nanotube conductivity [9]. Therefore, more investigations need to be performed to distinguish target gas in the air or gas mixtures.

For the selective detection of analytes, CNTs have to be functionalized with bio-recognition molecules, i.e. enzymes, antibodies, aptamers, etc. Covalent functionalization methods are often applied, which introduces carboxylic (-COOH) groups on CNT sidewalls to couple with the amine (-NH₂) groups in proteins or the amine-terminated ends of aptamers via amide bond formation [280, 335]. However, this covalent modification disrupts the in-plane sp^2 bonding in the carbon lattice pattern and introduces defects, leading to significant distortion of desirable electrical properties of CNTs [336]. Therefore, non-covalent functionalization of carbon nanomaterials to modify the nanotube surface in a non-destructive manner has to be further explored. Although biosensor investigation has taken a variety of directions in recent years, only a few of them appear to be viable for integration into a functional device and subsequent commercialization [337]. There are still major considerations surrounding the sensors that need to be carefully addressed before commercialization.

Besides the application of chemical sensors, the application of our vertically aligned N-MWCNTs also requires being explored applying in other research fields. Gong et al. [338] reported that vertically aligned nitrogen-containing carbon nanotubes can act as a metal-free electrode in alkaline fuel cells, which presented much better electrocatalytic activity, long-term operation stability and tolerance to crossover effect than platinum. Shin et al. [339] reported that lithium ions can diffuse through wall defects in N-MWCNTs to occupy a large portion of the interwall space as storage regions. They developed N-MWCNTs to improve the Li storage capability to 3500 mAh/g with a cycle life of greater than 10 000 times. García-García [340] applied N-MWCNTs to support ruthenium catalysts in the ammonia decomposition reaction, and they confirmed that catalytic activity of Ru particles was significantly improved when supported

on nitrogen doped carbon nanotubes. Lee et al. [341] also reported that carbon hybrid films made of vertically aligned N-doped carbon nanotubes grown on mechanically compliant reduced graphene films have outstanding flexible field emission properties. Qiao et al. [342] suggested that the field emission properties of carbon nanotubes can be enhanced by the doping with nitrogen atoms, because this causes a dramatic enhancement of density of states at Fermi level. Yao [343] also reported that magnetic metal (e.g. Fe, Co, Ni) nanocrystals encapsulated into nitrogen doped carbon nanotubes can be applied as Fenton-like catalysts for organic pollutant removal. Therefore, the technologies for N-MWCNTs developed in our work have high a potential for the application in other fields of research and development.

Appendix A

The Antoine equation [344] is given by:

$$\log_{10}p = A - \frac{B}{T+C} \quad (\text{A1})$$

where p is the vapor pressure, T is temperature and A , B and C are component-specific constants. For acetonitrile, $A = 7.12$, $B = 1314.40$, $C = 230.00$; while for ethanol, $A = 8.04$, $B = 1554.30$, $C = 222.65$. Therefore, the vapor pressures of acetonitrile and ethanol at different temperatures can be calculated, which are listed in Table A1.

Table A1: Vapor pressure of acetonitrile and ethanol at different temperatures from 10 to 40 °C.

Temperature/ °C	Vapor pressure/ mbar	
	Acetonitrile	Ethanol
10	58.6	30.83
15	75.84	42.61
20	97.03	58.12
25	122.92	78.27
30	154.85	104.19
35	192.70	137.16
40	237.09	178.69

Bibliography

- [1] H. Dai, Carbon nanotubes: opportunities and challenges, *Surface Science*, 500 (2002) 218-241.
- [2] B. Timmer, W. Olthuis, A.v.d. Berg, Ammonia sensors and their applications-a review, *Sensors and Actuators B: Chemical*, 107 (2005) 666-677.
- [3] P. Ramnani, N.M. Saucedo, A. Mulchandani, Carbon nanomaterial-based electrochemical biosensors for label-free sensing of environmental pollutants, *Chemosphere*, 143 (2016) 85-98.
- [4] D. Wei, M.J.A. Bailey, P. Andrew, T. Ryhanen, Electrochemical biosensors at the nanoscale, *Lab on a Chip*, 9 (2009) 2123-2131.
- [5] C. Staii, A.T. Johnson, M. Chen, A. Gelperin, DNA-decorated carbon nanotubes for chemical sensing, *Nano Letters*, 5 (2005) 1774-1778.
- [6] N. Chartuprayoon, M. Zhang, W. Bosze, Y.H. Choa, N.V. Myung, One-dimensional nanostructures based bio-detection, *Biosensors & Bioelectronics*, 63 (2015) 432-443.
- [7] Q. Zhang, Y. Qiao, F. Hao, L. Zhang, S. Wu, Y. Li, J. Li, X.M. Song, Fabrication of a biocompatible and conductive platform based on a single-stranded DNA/graphene nanocomposite for direct electrochemistry and electrocatalysis, *Chemistry*, 16 (2010) 8133-8139.
- [8] T. Kokabu, S. Inoue, Y. Matsumura, Trial for simple gas sensor composed of as-grown carbon nanotubes, *Chemical Physics Letters*, 628 (2015) 81-84.
- [9] A. Modi, N. Koratkar, E. Lass, B. Wei, P.M. Ajayan, Miniaturized gas ionization sensors using carbon nanotubes, *Nature*, 424 (2003) 171-174.
- [10] S. Iijima, Helical microtubules of graphitic carbon, *Nature*, 354 (1991) 56-58.
- [11] D.W.H. Fam, A. Palaniappan, A.I.Y. Tok, B. Liedberg, S.M. Moochhala, A review on technological aspects influencing commercialization of carbon nanotube sensors, *Sensors and Actuators B: Chemical*, 157 (2011) 1-7.
- [12] P.G. Collins, K. Bradley, M. Ishigami, A. Zettl, Extreme oxygen sensitivity of electronic properties of carbon nanotubes, *Science*, 287 (2000) 1801-1804.
- [13] W. Chen, *Doped nanomaterials and nanodevices*, American Scientific Publishers, 2010.

- [14] P. Britto, K. Santhanam, P. Ajayan, Carbon nanotube electrode for oxidation of dopamine, *Bioelectrochemistry and Bioenergetics*, 41 (1996) 121-125.
- [15] J. Kong, N.R. Franklin, C. Zhou, M.G. Chapline, S. Peng, K. Cho, H. Dai, Nanotube molecular wires as chemical sensors, *Science*, 287 (2000) 622-625.
- [16] Y. Cui, Q. Wei, H. Park, C.M. Lieber, Nanowire nanosensors for highly sensitive and selective detection of biological and chemical species, *Science*, 293 (2001) 1289-1292.
- [17] B.L. Allen, P.D. Kichambare, A. Star, Carbon nanotube field-effect-transistor-based biosensors, *Advanced Materials*, 19 (2007) 1439-1451.
- [18] E. Morales-Narvaez, A. Merkoci, Graphene oxide as an optical biosensing platform, *Advanced Materials*, 24 (2012) 3298-3308.
- [19] A. Star, E. Tu, J. Niemann, J.-C.P. Gabriel, C.S. Joiner, C. Valcke, Label-free detection of DNA hybridization using carbon nanotube network field-effect transistors, *Proceedings of the National Academy of Sciences of the United States of America*, 103 (2006) 921-926.
- [20] A.Z. Sadek, C. Zhang, Z. Hu, J.G. Partridge, D.G. McCulloch, W. Wlodarski, K. Kalantar-zadeh, Uniformly dispersed Pt-Ni nanoparticles on nitrogen-doped carbon nanotubes for hydrogen sensing, *The Journal of Physical Chemistry C*, 114 (2010) 238-242.
- [21] J. Kong, M.G. Chapline, H. Dai, Functionalized carbon nanotubes for molecular hydrogen sensors, *Advanced Materials*, 13 (2001) 1384-1386.
- [22] Y. Lu, J. Li, J. Han, H.-T. Ng, C. Binder, C. Partridge, M. Meyyappan, Room temperature methane detection using palladium loaded single-walled carbon nanotube sensors, *Chemical Physics Letters*, 391 (2004) 344-348.
- [23] N. Du, H. Zhang, X. Ma, D. Yang, Homogeneous coating of Au and SnO₂ nanocrystals on carbon nanotubes via layer-by-layer assembly: a new ternary hybrid for a room-temperature CO gas sensor, *Chemical Communications*, (2008) 6182-6184.
- [24] C.B. Jacobs, M.J. Peairs, B.J. Venton, Review: carbon nanotube based electrochemical sensors for biomolecules, *Analytica Chimica Acta*, 662 (2010) 105-127.
- [25] T. Kurkina, A. Vlandas, A. Ahmad, K. Kern, K. Balasubramanian, Label-free detection of few copies of DNA with carbon nanotube impedance biosensors, *Angewandte Chemie International Edition*, 50 (2011) 3710-3714.

- [26] K. Balasubramanian, K. Kern, 25th anniversary article: label-free electrical biodetection using carbon nanostructures, *Advanced Materials*, 26 (2014) 1154-1175.
- [27] NanoIntegris, Semiconducting SWNTs, Available from: <http://www.nanointegris.com/en/semiconducting>.
- [28] K. Wetchakun, T. Samerjai, N. Tamaekong, C. Liewhiran, C. Siriwong, V. Kruefu, A. Wisitsoraat, A. Tuantranont, S. Phanichphant, Semiconducting metal oxides as sensors for environmentally hazardous gases, *Sensors and Actuators B: Chemical*, 160 (2011) 580-591.
- [29] L. Li, F. Yang, J. Yu, X. Wang, L. Zhang, Y. Chen, H. Yang, In situ growth of ZnO nanowires on Zn comb-shaped interdigitating electrodes and their photosensitive and gas-sensing characteristics, *Materials Research Bulletin*, 47 (2012) 3971-3975.
- [30] J.B.K. Law, J.T.L. Thong, Improving the NH₃ gas sensitivity of ZnO nanowire sensors by reducing the carrier concentration, *Nanotechnology*, 19 (2008) 205502.
- [31] A. Star, E. Tu, J. Niemann, J.C. Gabriel, C.S. Joiner, C. Valcke, Label-free detection of DNA hybridization using carbon nanotube network field-effect transistors, *Proceedings of the National Academy of Sciences of the United States of America*, 103 (2006) 921-926.
- [32] U. Yaqoob, A.S.M.I. Uddin, G.-S. Chung, A high-performance flexible NO₂ sensor based on WO₃ NPs decorated on MWCNTs and RGO hybrids on PI/PET substrates, *Sensors and Actuators B: Chemical*, 224 (2016) 738-746.
- [33] G. Jimenez-Cadena, J. Riu, F.X. Rius, Gas sensors based on nanostructured materials, *Analyst*, 132 (2007) 1083-1099.
- [34] A. Afzal, N. Cioffi, L. Sabbatini, L. Torsi, NO_x sensors based on semiconducting metal oxide nanostructures: Progress and perspectives, *Sensors and Actuators B: Chemical*, 171-172 (2012) 25-42.
- [35] J. Kong, Nanotube Molecular Wires as Chemical Sensors, *Science*, 287 (2000) 622-625.
- [36] N. Iqbal, A. Afzal, N. Cioffi, L. Sabbatini, L. Torsi, NO_x sensing one- and two-dimensional carbon nanostructures and nanohybrids: progress and perspectives, *Sensors and Actuators B: Chemical*, 181 (2013) 9-21.
- [37] A. Eatemadi, H. Daraee, H. Karimkhanloo, M. Kouhi, N. Zarghami, A. Akbarzadeh, M. Abasi, Y. Hanifehpour, S.W. Joo, Carbon nanotubes: properties, synthesis, purification, and medical applications, *Nanoscale Research Letters*, 9 (2014) 393-393.

- [38] C.N.R. Rao, A.K. Sood, K.S. Subrahmanyam, A. Govindaraj, Graphene: the new two-dimensional nanomaterial, *Angewandte Chemie International Edition*, 48 (2009) 7752-7777.
- [39] A.K. Geim, K.S. Novoselov, The rise of graphene, *Nature materials*, 6 (2007) 183-191.
- [40] Philschatz/chemistry-book, Hybrid Atomic Orbitals, Available from: <http://philschatz.com/chemistry-book/contents/m51057.html>.
- [41] J.M. Arrieta, Tight-binding description of graphene nanostructures, in: modelling of plasmonic and graphene nanodevices, Springer, 2014, pp. 13-23.
- [42] G.G. Samsonidze, R. Saito, A. Jorio, M.A. Pimenta, A.G. Souza Filho, A. Gruneis, G. Dresselhaus, M.S. Dresselhaus, The concept of cutting lines in carbon nanotube science, *Journal of Nanoscience and Nanotechnology*, 3 (2003) 431-458.
- [43] A.H. Castro Neto, F. Guinea, N.M.R. Peres, K.S. Novoselov, A.K. Geim, The electronic properties of graphene, *Reviews of Modern Physics*, 81 (2009) 109-162.
- [44] M.F. Budyka, T.S. Zyubina, A.G. Ryabenko, S.H. Lin, A.M. Mebel, Bond lengths and diameters of armchair single wall carbon nanotubes, *Chemical Physics Letters*, 407 (2005) 266-271.
- [45] H. Dai, Carbon nanotubes: synthesis, integration, and properties, *Accounts of Chemical Research*, 35 (2002) 1035-1044.
- [46] T. Hayashi, Y.A. Kim, T. Matoba, M. Esaka, K. Nishimura, T. Tsukada, M. Endo, M.S. Dresselhaus, Smallest freestanding single-walled carbon nanotube, *Nano Letters*, 3 (2003) 887-889.
- [47] D. Bethune, C. Klang, M. De Vries, G. Gorman, R. Savoy, J. Vazquez, R. Beyers, Cobalt-catalysed growth of carbon nanotubes with single-atomic-layer walls, *Nature*, 363 (1993) 605-607.
- [48] R.H. Baughman, A.A. Zakhidov, W.A. de Heer, Carbon nanotubes-the route toward applications, *Science*, 297 (2002) 787-792.
- [49] T. Belin, F. Epron, Characterization methods of carbon nanotubes: a review, *Materials Science and Engineering: B*, 119 (2005) 105-118.
- [50] S. Iijima, T. Ichihashi, Single-shell carbon nanotubes of 1-nm diameter, *Nature*, 363 (1993) 603-605.

- [51] D.S. Bethune, C.H. Klang, M.S. de Vries, G. Gorman, R. Savoy, J. Vazquez, R. Beyers, Cobalt-catalysed growth of carbon nanotubes with single-atomic-layer walls, *Nature*, 363 (1993) 605-607.
- [52] P.M. Ajayan, J.M. Lambert, P. Bernier, L. Barbedette, C. Colliex, J.M. Planeix, Growth morphologies during cobalt-catalyzed single-shell carbon nanotube synthesis, *Chemical Physics Letters*, 215 (1993) 509-517.
- [53] E.T. Thostenson, Z. Ren, T.-W. Chou, Advances in the science and technology of carbon nanotubes and their composites: a review, *Composites Science and Technology*, 61 (2001) 1899-1912.
- [54] S. Subramoney, Novel nanocarbons-structure, properties, and potential applications, *Advanced Materials*, 10 (1998) 1157-1171.
- [55] X. Wang, Q. Li, J. Xie, Z. Jin, J. Wang, Y. Li, K. Jiang, S. Fan, Fabrication of ultralong and electrically uniform single-walled carbon nanotubes on clean substrates, *Nano Letters*, 9 (2009) 3137-3141.
- [56] A. Maiti, Carbon nanotubes: bandgap engineering with strain, *Nature Materials*, 2 (2003) 440-442.
- [57] M.S. Dresselhaus, Y.M. Lin, O. Rabin, A. Jorio, A.G. Souza Filho, M.A. Pimenta, R. Saito, G. Samsonidze, G. Dresselhaus, Nanowires and nanotubes, *Materials Science and Engineering: C*, 23 (2003) 129-140.
- [58] M.S. Dresselhaus, G. Dresselhaus, R. Saito, Physics of carbon nanotubes, *Carbon*, 33 (1995) 883-891.
- [59] M.S. Dresselhaus, G. Dresselhaus, A. Jorio, Unusual properties and structure of carbon nanotubes, *Annual Review of Materials Research*, 34 (2004) 247-278.
- [60] H. Fiedler, Preparation and characterization of carbon nanotube based vertical interconnections for integrated circuits, Ph.D. thesis, Technische Universität Chemnitz (2013) .
- [61] N. Hamada, S.-i. Sawada, A. Oshiyama, New one-dimensional conductors: graphitic microtubules, *Physical Review Letters*, 68 (1992) 1579-1581.
- [62] R. Saito, M. Fujita, G. Dresselhaus, M.S. Dresselhaus, Electronic structure of chiral graphene tubules, *Applied Physics Letters*, 60 (1992) 2204-2206.

- [63] P.G. Collins, P. Avouris, The electronic properties of carbon nanotubes, *Contemporary Concepts of Condensed Matter Science*, 3 (2008) 49-81.
- [64] T.W. Odom, J.-L. Huang, P. Kim, C.M. Lieber, Atomic structure and electronic properties of single-walled carbon nanotubes, *Nature*, 391 (1998) 62-64.
- [65] J.W. Wilder, L.C. Venema, A.G. Rinzler, R.E. Smalley, C. Dekker, Electronic structure of atomically resolved carbon nanotubes, *Nature*, 391 (1998) 59-62.
- [66] L. Chico, V.H. Crespi, L.X. Benedict, S.G. Louie, M.L. Cohen, Pure carbon nanoscale devices: nanotube heterojunctions, *Physical Review Letters*, 76 (1996) 971-974.
- [67] Y. Liu, S. Kumar, Polymer/carbon nanotube nano composite fibers-a review, *ACS Applied Materials & Interfaces*, 6 (2014) 6069-6087.
- [68] R. Martel, T. Schmidt, H.R. Shea, T. Hertel, P. Avouris, Single- and multi-wall carbon nanotube field-effect transistors, *Applied Physics Letters*, 73 (1998) 2447-2449.
- [69] J. Li, Y. Lu, Q. Ye, M. Cinke, J. Han, M. Meyyappan, Carbon nanotube sensors for gas and organic vapor detection, *Nano Letters*, 3 (2003) 929-933.
- [70] Y. Wang, J.T.W. Yeow, A Review of Carbon Nanotubes-based gas sensors, *Journal of Sensors*, 2009 (2009) 24.
- [71] M. Shim, N.W. Shi Kam, R.J. Chen, Y. Li, H. Dai, Functionalization of carbon nanotubes for biocompatibility and biomolecular recognition, *Nano Letters*, 2 (2002) 285-288.
- [72] R. Saito, G. Dresselhaus, M.S. Dresselhaus, *Physical properties of carbon nanotubes*, World Scientific, 1998.
- [73] T. Hertel, G. Moos, Electron-phonon interaction in single-wall carbon nanotubes: a time-domain study, *Physical Review Letters*, 84 (2000) 5002-5005.
- [74] P. Poncharal, C. Berger, Y. Yi, Z.L. Wang, W.A. de Heer, Room temperature ballistic conduction in carbon nanotubes, *The Journal of Physical Chemistry B*, 106 (2002) 12104-12118.
- [75] S. Sanvito, Y.-K. Kwon, D. Tománek, C.J. Lambert, Fractional quantum conductance in carbon nanotubes, *Physical Review Letters*, 84 (2000) 1974-1977.

- [76] Q. Zhang, J.Q. Huang, W.Z. Qian, Y.Y. Zhang, F. Wei, The road for nanomaterials industry: a review of carbon nanotube production, post-treatment, and bulk applications for composites and energy storage, *Small*, 9 (2013) 1237-1265.
- [77] M.-F. Yu, O. Lourie, M.J. Dyer, K. Moloni, T.F. Kelly, R.S. Ruoff, Strength and breaking mechanism of multiwalled carbon nanotubes under tensile load, *Science*, 287 (2000) 637-640.
- [78] J.P. Lu, Elastic properties of single and multilayered nanotubes, *Journal of Physics and Chemistry of Solids*, 58 (1997) 1649-1652.
- [79] G. Overney, W. Zhong, D. Tománek, Structural rigidity and low frequency vibrational modes of long carbon tubules, *Zeitschrift für Physik D Atoms, Molecules and Clusters*, 27 (1993) 93-96.
- [80] M. Dresselhaus, G. Dresselhaus, A. Jorio, Unusual properties and structure of carbon nanotubes, *Annual Review of Materials Research*, 34 (2004) 247-278.
- [81] J. Hone, Carbon nanotubes: thermal properties, *Journal of Nanoscience and Nanotechnology*, 6 (2004) 603-610.
- [82] H.T. Ham, Y.S. Choi, I.J. Chung, An explanation of dispersion states of single-walled carbon nanotubes in solvents and aqueous surfactant solutions using solubility parameters, *Journal of Colloid and Interface Science*, 286 (2005) 216-223.
- [83] J.C. Carrero-Sánchez, A.L. Elías, R. Mancilla, G. Arrellín, H. Terrones, J.P. Laclette, M. Terrones, Biocompatibility and toxicological studies of carbon nanotubes doped with nitrogen, *Nano Letters*, 6 (2006) 1609-1616.
- [84] A. Jimeno, S. Goyanes, A. Eceiza, G. Kortaberria, I. Mondragon, M.A. Corcuera, Effects of amine molecular structure on carbon nanotubes functionalization, *Journal of Nanoscience and Nanotechnology*, 9 (2009) 6222-6227.
- [85] V.J. González, E. Gracia-Espino, A. Morelos-Gómez, F. López-Urías, H. Terrones, M. Terrones, Biotin molecules on nitrogen-doped carbon nanotubes enhance the uniform anchoring and formation of Ag nanoparticles, *Carbon*, 88 (2015) 51-59.
- [86] W. Han, Y. Bando, K. Kurashima, T. Sato, Boron-doped carbon nanotubes prepared through a substitution reaction, *Chemical Physics Letters*, 299 (1999) 368-373.

- [87] R. Czerw, M. Terrones, J.C. Charlier, X. Blase, B. Foley, R. Kamalakaran, N. Grobert, H. Terrones, D. Tekleab, P.M. Ajayan, W. Blau, M. Rühle, D.L. Carroll, Identification of electron donor states in N-doped carbon nanotubes, *Nano Letters*, 1 (2001) 457-460.
- [88] Y. Cao, H. Yu, J. Tan, F. Peng, H. Wang, J. Li, W. Zheng, N.-B. Wong, Nitrogen-, phosphorous- and boron-doped carbon nanotubes as catalysts for the aerobic oxidation of cyclohexane, *Carbon*, 57 (2013) 433-442.
- [89] E. Cruz-Silva, F. López-Urías, E. Muñoz-Sandoval, B.G. Sumpter, H. Terrones, J.-C. Charlier, V. Meunier, M. Terrones, Electronic transport and mechanical properties of phosphorus- and phosphorus-nitrogen-doped carbon nanotubes, *ACS Nano*, 3 (2009) 1913-1921.
- [90] J. Haihui, Z. Dongju, W. Ruoxi, Silicon-doped carbon nanotubes: a potential resource for the detection of chlorophenols/chlorophenoxy radicals, *Nanotechnology*, 20 (2009) 145501.
- [91] M. Terrones, A.S. Filho, A. Rao, Doped carbon nanotubes: synthesis, characterization and applications, in: A. Jorio, G. Dresselhaus, M. Dresselhaus (Eds.) *Carbon Nanotubes*, Springer Berlin Heidelberg, 2008, pp. 531-566.
- [92] F. Xu, M. Minniti, P. Barone, A. Sindona, A. Bonanno, A. Oliva, Nitrogen doping of single walled carbon nanotubes by low energy N_2^+ ion implantation, *Carbon*, 46 (2008) 1489-1496.
- [93] O. Stephan, P. Ajayan, C. Colliex, P. Redlich, Doping graphitic and carbon nanotube structures with boron and nitrogen, *Science*, 266 (1994) 1683.
- [94] C. Deng, J. Chen, X. Chen, C. Xiao, L. Nie, S. Yao, Direct electrochemistry of glucose oxidase and biosensing for glucose based on boron-doped carbon nanotubes modified electrode, *Biosensors and Bioelectronics*, 23 (2008) 1272-1277.
- [95] I. Mukhopadhyay, N. Hoshino, S. Kawasaki, F. Okino, W. Hsu, H. Touhara, Electrochemical Li insertion in B-doped multiwall carbon nanotubes, *Journal of the Electrochemical Society*, 149 (2002) A39-A44.
- [96] Q. Wei, X. Tong, G. Zhang, J. Qiao, Q. Gong, S. Sun, Nitrogen-doped carbon nanotube and graphene materials for oxygen reduction reactions, *Catalysts*, 5 (2015) 1574-1602.
- [97] P. Ayala, R. Arenal, M. Rummeli, A. Rubio, T. Pichler, The doping of carbon nanotubes with nitrogen and their potential applications, *Carbon*, 48 (2010) 575-586.

- [98] J.W. Jang, C.E. Lee, S.C. Lyu, T.J. Lee, C.J. Lee, Structural study of nitrogen-doping effects in bamboo-shaped multiwalled carbon nanotubes, *Applied Physics Letters*, 84 (2004) 2877.
- [99] E.N. Nxumalo, N.J. Coville, Nitrogen doped carbon nanotubes from organometallic compounds: a review, *Materials*, 3 (2010) 2141-2171.
- [100] K. Ghosh, M. Kumar, T. Maruyama, Y. Ando, Tailoring the field emission property of nitrogen-doped carbon nanotubes by controlling the graphitic/pyridinic substitution, *Carbon*, 48 (2010) 191-200.
- [101] E.N. Nxumalo, V.O. Nyamori, N.J. Coville, CVD synthesis of nitrogen doped carbon nanotubes using ferrocene/aniline mixtures, *Journal of Organometallic Chemistry*, 693 (2008) 2942-2948.
- [102] J.D. Wiggins-Camacho, K.J. Stevenson, Effect of nitrogen concentration on capacitance, density of states, electronic conductivity, and morphology of N-doped carbon nanotube electrodes, *The Journal of Physical Chemistry C*, 113 (2009) 19082-19090.
- [103] I. Stavarache, A.-M. Lepadatu, V.S. Teodorescu, M.L. Ciurea, V. Iancu, M. Dragoman, G. Konstantinidis, R. Buiculescu, Electrical behavior of multi-walled carbon nanotube network embedded in amorphous silicon nitride, *Nanoscale Research Letters*, 6 (2011) 88.
- [104] S. Maldonado, S. Morin, K.J. Stevenson, Structure, composition, and chemical reactivity of carbon nanotubes by selective nitrogen doping, *Carbon*, 44 (2006) 1429-1437.
- [105] R. Czerw, M. Terrones, J.-C. Charlier, X. Blase, B. Foley, R. Kamalakaran, N. Grobert, H. Terrones, D. Tekleab, P. Ajayan, Identification of electron donor states in N-doped carbon nanotubes, *Nano Letters*, 1 (2001) 457-460.
- [106] J.-J. Adjizian, R. Leghrib, A.A. Koos, I. Suarez-Martinez, A. Crossley, P. Wagner, N. Grobert, E. Llobet, C.P. Ewels, Boron- and nitrogen-doped multi-wall carbon nanotubes for gas detection, *Carbon*, 66 (2014) 662-673.
- [107] Y. Wang, Y. Shao, D.W. Matson, J. Li, Y. Lin, Nitrogen-doped graphene and its application in electrochemical biosensing, *ACS Nano*, 4 (2010) 1790-1798.
- [108] Q. Liu, Z. Pu, A.M. Asiri, X. Sun, Bamboo-like nitrogen-doped carbon nanotubes toward fluorescence recovery assay for DNA detection, *Sensors and Actuators B: Chemical*, 206 (2015) 37-42.

- [109] T. Susi, T. Pichler, P. Ayala, X-ray photoelectron spectroscopy of graphitic carbon nanomaterials doped with heteroatoms, *Beilstein Journal of Nanotechnology*, 6 (2015) 177-192.
- [110] A.L. Elias, P. Ayala, A. Zamudio, M. Grobosch, E. Cruz-Silva, J.M. Romo-Herrera, J. Campos-Delgado, H. Terrones, T. Pichler, M. Terrones, Spectroscopic characterization of N-doped single-walled carbon nanotube strands: an X-ray photoelectron spectroscopy and Raman study, *Journal of Nanoscience and Nanotechnology*, 10 (2010) 3959-3964.
- [111] C. Schmädicke, Silicon nanowire based sensor for highly sensitive and selective detection of ammonia. Ph.D. Thesis, Technische Universität Dresden (2015).
- [112] S. Cui, H. Pu, G. Lu, Z. Wen, E.C. Mattson, C. Hirschmugl, M. Gajdardziska-Josifovska, M. Weinert, J. Chen, Fast and selective room-temperature ammonia sensors using silver nanocrystal-functionalized carbon nanotubes, *ACS applied materials & interfaces*, 4 (2012) 4898-4904.
- [113] M. Reyes-Reyes, N. Grobert, R. Kamalakaran, T. Seeger, D. Golberg, M. Rühle, Y. Bando, H. Terrones, M. Terrones, Efficient encapsulation of gaseous nitrogen inside carbon nanotubes with bamboo-like structure using aerosol thermolysis, *Chemical Physics Letters*, 396 (2004) 167-173.
- [114] O. Stephan, P.M. Ajayan, C. Colliex, P. Redlich, J.M. Lambert, P. Bernier, P. Lefin, Doping graphitic and carbon nanotube structures with boron and nitrogen, *Science*, 266 (1994) 1683-1685.
- [115] R. Droppa Jr, P. Hammer, A.C.M. Carvalho, M.C. dos Santos, F. Alvarez, Incorporation of nitrogen in carbon nanotubes, *Journal of Non-Crystalline Solids*, 299-302, Part 2 (2002) 874-879.
- [116] M. Glerup, J. Steinmetz, D. Samaille, O. Stephan, S. Enouz, A. Loiseau, S. Roth, P. Bernier, Synthesis of N-doped SWNT using the arc-discharge procedure, *Chemical Physics Letters*, 387 (2004) 193-197.
- [117] B. Wang, Y. Ma, Y. Wu, N. Li, Y. Huang, Y. Chen, Direct and large scale electric arc discharge synthesis of boron and nitrogen doped single-walled carbon nanotubes and their electronic properties, *Carbon*, 47 (2009) 2112-2115.
- [118] A.A. Koós, F. Dillon, R.J. Nicholls, L. Bulusheva, N. Grobert, N-SWCNTs production by aerosol-assisted CVD method, *Chemical Physics Letters*, 538 (2012) 108-111.

- [119] Z. Yang, Y. Xia, R. Mokaya, Aligned N-doped carbon nanotube bundles prepared via CVD using zeolite substrates, *Chemistry of Materials*, 17 (2005) 4502-4508.
- [120] M. Yudasaka, R. Kikuchi, Y. Ohki, S. Yoshimura, Nitrogen-containing carbon nanotube growth from Ni phthalocyanine by chemical vapor deposition, *Carbon*, 35 (1997) 195-201.
- [121] Y. Wang, X. Cui, Y. Li, L. Chen, H. Chen, L. Zhang, J. Shi, A co-pyrolysis route to synthesize nitrogen doped multiwall carbon nanotubes for oxygen reduction reaction, *Carbon*, 68 (2014) 232-239.
- [122] P. Ayala, A. Grüneis, T. Gemming, D. Grimm, C. Kramberger, M.H. Rummeli, F.L. Freire, H. Kuzmany, R. Pfeiffer, A. Barreiro, Tailoring N-doped single and double wall carbon nanotubes from a nondiluted carbon/nitrogen feedstock, *The Journal of Physical Chemistry C*, 111 (2007) 2879-2884.
- [123] C. Tang, D. Golberg, Y. Bando, F. Xu, B. Liu, Synthesis and field emission of carbon nanotubular fibers doped with high nitrogen content, *Chemical Communications*, (2003) 3050-3051.
- [124] C.V. Rao, C.R. Cabrera, Y. Ishikawa, In search of the active site in nitrogen-doped carbon nanotube electrodes for the oxygen reduction reaction, *The Journal of Physical Chemistry Letters*, 1 (2010) 2622-2627.
- [125] C. Venkateswara Rao, Y. Ishikawa, Activity, selectivity, and anion-exchange membrane fuel cell performance of virtually metal-free nitrogen-doped carbon nanotube electrodes for oxygen reduction reaction, *The Journal of Physical Chemistry C*, 116 (2012) 4340-4346.
- [126] Z. Mo, S. Liao, Y. Zheng, Z. Fu, Preparation of nitrogen-doped carbon nanotube arrays and their catalysis towards cathodic oxygen reduction in acidic and alkaline media, *Carbon*, 50 (2012) 2620-2627.
- [127] D.H. Lee, W.J. Lee, S.O. Kim, Highly efficient vertical growth of wall-number-selected, N-doped carbon nanotube arrays, *Nano Letters*, 9 (2009) 1427-1432.
- [128] K.L. Choy, Special issue on aerosol-assisted chemical vapor deposition, *Chemical Vapor Deposition*, 12 (2006) 581-582.
- [129] K. Hata, D.N. Futaba, K. Mizuno, T. Namai, M. Yumura, S. Iijima, Water-assisted highly efficient synthesis of impurity-free single-walled carbon nanotubes, *Science*, 306 (2004) 1362-1364.

- [130] Y. Murakami, S. Chiashi, Y. Miyauchi, M. Hu, M. Ogura, T. Okubo, S. Maruyama, Growth of vertically aligned single-walled carbon nanotube films on quartz substrates and their optical anisotropy, *Chemical Physics Letters*, 385 (2004) 298-303.
- [131] G. Zhang, D. Mann, L. Zhang, A. Javey, Y. Li, E. Yenilmez, Q. Wang, J.P. McVittie, Y. Nishi, J. Gibbons, Ultra-high-yield growth of vertical single-walled carbon nanotubes: hidden roles of hydrogen and oxygen, *Proceedings of the National Academy of Sciences of the United States of America*, 102 (2005) 16141-16145.
- [132] A.J. Hart, L. van Laake, A.H. Slocum, Desktop growth of carbon-nanotube monoliths with in situ optical imaging, *Small*, 3 (2007) 772-777.
- [133] M. Kumar, Y. Ando, Chemical vapor deposition of carbon nanotubes: a review on growth mechanism and mass production, *Journal of Nanoscience and Nanotechnology*, 10 (2010) 3739-3758.
- [134] E.M.M. Ibrahim, V.O. Khavrus, A. Leonhardt, S. Hampel, S. Oswald, M.H. Rummeli, B. Büchner, Synthesis, characterization, and electrical properties of nitrogen-doped single-walled carbon nanotubes with different nitrogen content, *Diamond and Related Materials*, 19 (2010) 1199-1206.
- [135] T.C. Nagaiah, S. Kundu, M. Bron, M. Muhler, W. Schuhmann, Nitrogen-doped carbon nanotubes as a cathode catalyst for the oxygen reduction reaction in alkaline medium, *Electrochemistry Communications*, 12 (2010) 338-341.
- [136] A. Gohel, K. Chin, Y. Zhu, C. Sow, A. Wee, Field emission properties of N₂ and Ar plasma-treated multi-wall carbon nanotubes, *Carbon*, 43 (2005) 2530-2535.
- [137] H.R. Barzegar, E. Gracia-Espino, T. Sharifi, F. Nitze, T. Wågberg, Nitrogen doping mechanism in small diameter single-walled carbon nanotubes: impact on electronic properties and growth selectivity, *The Journal of Physical Chemistry C*, 117 (2013) 25805-25816.
- [138] Y. Shao, J. Sui, G. Yin, Y. Gao, Nitrogen-doped carbon nanostructures and their composites as catalytic materials for proton exchange membrane fuel cell, *Applied Catalysis B: Environmental*, 79 (2008) 89-99.
- [139] P. Chen, T.Y. Xiao, Y.H. Qian, S.S. Li, S.H. Yu, A Nitrogen-doped graphene/carbon nanotube nanocomposite with synergistically enhanced electrochemical activity, *Advanced Materials*, 25 (2013) 3192-3196.

- [140] E.G. Wang, A new development in covalently bonded carbon nitride and related materials, *Advanced Materials*, 11 (1999) 1129-1133.
- [141] M. Glerup, M. Castignolles, M. Holzinger, G. Hug, A. Loiseau, P. Bernier, Synthesis of highly nitrogen-doped multi-walled carbon nanotubes, *Chemical Communications*, (2003) 2542-2543.
- [142] J. Liu, R. Czerw, D. Carroll, Large-scale synthesis of highly aligned nitrogen doped carbon nanotubes by injection chemical vapor deposition methods, *Journal of Materials Research*, 20 (2005) 538-543.
- [143] L.S. Panchakarla, A. Govindaraj, C.N.R. Rao, Nitrogen- and boron-doped double-walled carbon nanotubes, *ACS Nano*, 1 (2007) 494-500.
- [144] F. Jaouen, M. Lefèvre, J.-P. Dodelet, M. Cai, Heat-treated Fe/N/C catalysts for O₂ electroreduction: are active sites hosted in micropores?, *The Journal of Physical Chemistry B*, 110 (2006) 5553-5558.
- [145] K. Yamamoto, T. Kamimura, K. Matsumoto, Nitrogen doping of single-walled carbon nanotube by using mass-separated low-energy ion beams, *Japanese Journal of Applied Physics*, 44 (2005) 1611.
- [146] P. Ayala, A. Grüneis, C. Kramberger, M. Rummeli, I. Solorzano, F. Freire Jr, T. Pichler, Effects of the reaction atmosphere composition on the synthesis of single and multiwalled nitrogen-doped nanotubes, *The Journal of Chemical Physics*, 127 (2007) 184709-184709.
- [147] J. Gavillet, A. Loiseau, C. Journet, F. Willaime, F. Ducastelle, J.C. Charlier, Root-growth mechanism for single-wall carbon nanotubes, *Physical Review Letters*, 87 (2001) 275504.
- [148] R.S. Wagner, W.C. Ellis, Vapor-liquid-solid mechanism of single crystal growth, *Applied Physics Letters*, 4 (1964) 89-90.
- [149] S. Taubert, K. Laasonen, Initial stages of growth of nitrogen-doped single-walled carbon nanotubes, *The Journal of Physical Chemistry C*, 116 (2012) 18538-18549.
- [150] M. Kumar, Y. Ando, Carbon nanotube synthesis and growth mechanism, INTECH Open Access Publisher, 2011.
- [151] M. Terrones, A.M. Benito, C. Manteca-Diego, W.K. Hsu, O.I. Osman, J.P. Hare, D.G. Reid, H. Terrones, A.K. Cheetham, K. Prassides, H.W. Kroto, D.R.M. Walton, Pyrolytically

grown BxCyNz nanomaterials: nanofibres and nanotubes, *Chemical Physics Letters*, 257 (1996) 576-582.

[152] K. Chizari, U. Sundararaj, The effects of catalyst on the morphology and physicochemical properties of nitrogen-doped carbon nanotubes, *Materials Letters*, 116 (2014) 289-292.

[153] J. Jiang, T. Feng, X. Cheng, L. Dai, G. Cao, B. Jiang, X. Wang, X. Liu, S. Zou, Synthesis and growth mechanism of Fe-catalyzed carbon nanotubes by plasma-enhanced chemical vapor deposition, *Nuclear Instruments and Methods in Physics Research Section B: Beam Interactions with Materials and Atoms*, 244 (2006) 327-332.

[154] A.M. Cassell, J.A. Raymakers, J. Kong, H. Dai, Large scale CVD synthesis of single-walled carbon nanotubes, *The Journal of Physical Chemistry B*, 103 (1999) 6484-6492.

[155] C.J. Lee, J. Park, Growth model of bamboo-shaped carbon nanotubes by thermal chemical vapor deposition, *Applied Physics Letters*, 77 (2000) 3397-3399.

[156] S. Van Dommele, A. Romero-Izquierdo, R. Brydson, K. De Jong, J. Bitter, Tuning nitrogen functionalities in catalytically grown nitrogen-containing carbon nanotubes, *Carbon*, 46 (2008) 138-148.

[157] K. Chizari, I. Janowska, M. Houllé, I. Florea, O. Ersen, T. Romero, P. Bernhardt, M.J. Ledoux, C. Pham-Huu, Tuning of nitrogen-doped carbon nanotubes as catalyst support for liquid-phase reaction, *Applied Catalysis A: General*, 380 (2010) 72-80.

[158] H. Dai, J. Kong, C. Zhou, N. Franklin, T. Tomblor, A. Cassell, S. Fan, M. Chapline, Controlled chemical routes to nanotube architectures, physics, and devices, *The Journal of Physical Chemistry B*, 103 (1999) 11246-11255.

[159] H. Yokomichi, F. Sakai, M. Ichihara, N. Kishimoto, Carbon nanotubes synthesized by thermal chemical vapor deposition using $M(NO_3)_n \cdot nH_2O$ as catalyst, *Physica B: Condensed Matter*, 323 (2002) 311-313.

[160] L. Zheng, X. Liao, Y.T. Zhu, Parametric study of carbon nanotube growth via cobalt-catalyzed ethanol decomposition, *Materials Letters*, 60 (2006) 1968-1972.

[161] K.P. De Jong, J.W. Geus, Carbon nanofibers: catalytic synthesis and applications, *Catalysis Reviews*, 42 (2000) 481-510.

[162] A. Grüneis, C. Kramberger, D. Grimm, T. Gemming, M.H. Rummeli, A. Barreiro, P. Ayala, T. Pichler, C. Schaman, H. Kuzmany, J. Schumann, B. Büchner, Eutectic limit for the

growth of carbon nanotubes from a thin iron film by chemical vapor deposition of cyclohexane, *Chemical Physics Letters*, 425 (2006) 301-305.

[163] P. Ayala, A. Grüneis, T. Gemming, B. Büchner, M.H. Rummeli, D. Grimm, J. Schumann, R. Kaltofen, F.L. Freire Jr, H.D.F. Filho, T. Pichler, Influence of the catalyst hydrogen pretreatment on the growth of vertically aligned nitrogen-doped carbon nanotubes, *Chemistry of Materials*, 19 (2007) 6131-6137.

[164] D.B. Geohegan, A.A. Puzos, I.N. Ivanov, S. Jesse, G. Eres, J.Y. Howe, In situ growth rate measurements and length control during chemical vapor deposition of vertically aligned multiwall carbon nanotubes, *Applied Physics Letters*, 83 (2003) 1851-1853.

[165] G. Chen, R.C. Davis, H. Kimura, S. Sakurai, M. Yumura, D.N. Futaba, K. Hata, The relationship between the growth rate and the lifetime in carbon nanotube synthesis, *Nanoscale*, 7 (2015) 8873-8878.

[166] Zhong, T. Iwasaki, J. Robertson, H. Kawarada, Growth kinetics of 0.5 cm vertically aligned single-walled carbon nanotubes, *The Journal of Physical Chemistry B*, 111 (2007) 1907-1910.

[167] M.J. Bronikowski, Longer Nanotubes at Lower Temperatures: The influence of effective activation energies on carbon nanotube growth by thermal chemical vapor deposition, *The Journal of Physical Chemistry C*, 111 (2007) 17705-17712.

[168] K. Chizari, A. Vena, L. Laurentius, U. Sundararaj, The effect of temperature on the morphology and chemical surface properties of nitrogen-doped carbon nanotubes, *Carbon*, 68 (2014) 369-379.

[169] H.C. Choi, J. Park, B. Kim, Distribution and structure of N atoms in multiwalled carbon nanotubes using variable-energy X-ray photoelectron spectroscopy, *The Journal of Physical Chemistry B*, 109 (2005) 4333-4340.

[170] F. Villalpando-Paez, A. Zamudio, A. Elias, H. Son, E. Barros, S. Chou, Y. Kim, H. Muramatsu, T. Hayashi, J. Kong, Synthesis and characterization of long strands of nitrogen-doped single-walled carbon nanotubes, *Chemical Physics Letters*, 424 (2006) 345-352.

[171] G. Bepete, Z.N. Tetana, S. Lindner, M.H. Rummeli, Z. Chiguvare, N.J. Coville, The use of aliphatic alcohol chain length to control the nitrogen type and content in nitrogen doped carbon nanotubes, *Carbon*, 52 (2013) 316-325.

- [172] A.A. Koós, M. Dowling, K. Jurkschat, A. Crossley, N. Grobert, Effect of the experimental parameters on the structure of nitrogen-doped carbon nanotubes produced by aerosol chemical vapour deposition, *Carbon*, 47 (2009) 30-37.
- [173] X.X. Zhang, Z.Q. Li, G.H. Wen, K.K. Fung, J. Chen, Y. Li, Microstructure and growth of bamboo-shaped carbon nanotubes, *Chemical Physics Letters*, 333 (2001) 509-514.
- [174] B.G. Sumpter, J. Huang, V. Meunier, J.M. Romo-Herrera, E. Cruz-Silva, H. Terrones, M. Terrones, A theoretical and experimental study on manipulating the structure and properties of carbon nanotubes using substitutional dopants, *International Journal of Quantum Chemistry*, 109 (2009) 97-118.
- [175] B.G. Sumpter, V. Meunier, J.M. Romo-Herrera, E. Cruz-Silva, D.A. Cullen, H. Terrones, D.J. Smith, M. Terrones, Nitrogen-mediated carbon nanotube growth: diameter reduction, metallicity, bundle dispersability, and bamboo-like structure formation, *ACS Nano*, 1 (2007) 369-375.
- [176] M. Aksak, S. Kir, Y. Selamet, Effect of the growth temperature on carbon nanotubes grown by thermal chemical vapor deposition method, *Journal of Optoelectronics and Advanced Materials*, 1 (2009) 281-284.
- [177] Q.N. Thanh, H. Jeong, J. Kim, J.W. Kevek, Y.H. Ahn, S. Lee, E.D. Minot, J.Y. Park, Transfer-printing of as-fabricated carbon nanotube devices onto various substrates, *Advanced Materials*, 24 (2012) 4499-4504.
- [178] V.K. Sangwan, A. Southard, T.L. Moore, V.W. Ballarotto, D.R. Hines, M.S. Fuhrer, E.D. Williams, Transfer printing approach to all-carbon nanoelectronics, *Microelectronic Engineering*, 88 (2011) 3150-3154.
- [179] F. Mirri, A.W.K. Ma, T.T. Hsu, N. Behabtu, S.L. Eichmann, C.C. Young, D.E. Tsentelovich, M. Pasquali, High-performance carbon nanotube transparent conductive films by scalable dip coating, *ACS Nano*, 6 (2012) 9737-9744.
- [180] N.-W. Pu, C.-A. Wang, Y.-M. Liu, Y. Sung, D.-S. Wang, M.-D. Ger, Dispersion of graphene in aqueous solutions with different types of surfactants and the production of graphene films by spray or drop coating, *Journal of the Taiwan Institute of Chemical Engineers*, 43 (2012) 140-146.
- [181] L.E. Scriven, Physics and applications of DIP coating and spin coating, *MRS Online Proceedings Library Archive*, 121 (1988) 717.

- [182] C. Park, S.W. Kim, Y.-S. Lee, S.H. Lee, K.H. Song, L.S. Park, Spray coating of carbon nanotube on polyethylene terephthalate film for touch panel application, *Journal of Nanoscience and Nanotechnology*, 12 (2012) 5351-5355.
- [183] S. Kim, X. Wang, J.H. Yim, W.C. Tsoi, J.S. Kim, S. Lee, J.C. deMello, Efficient organic solar cells based on spray-patterned single wall carbon nanotube electrodes, *Photoe*, 2 (2012) 021010-021019.
- [184] T. Taishi, M. Noriko, L. Sheng-Yi, O. Haruya, A. Takeshi, S. Masashi, I. Yoshihiro, Ink-jet printing of carbon nanotube thin-film transistors on flexible plastic substrates, *Applied Physics Express*, 2 (2009) 025005.
- [185] H. Ago, K. Murata, M. Yumura, J. Yotani, S. Uemura, Ink-jet printing of nanoparticle catalyst for site-selective carbon nanotube growth, *Applied Physics Letters*, 82 (2003) 811-813.
- [186] A. Denneulin, J. Bras, F. Carcone, C. Neuman, A. Blayo, Impact of ink formulation on carbon nanotube network organization within inkjet printed conductive films, *Carbon*, 49 (2011) 2603-2614.
- [187] O.-S. Kwon, H. Kim, H. Ko, J. Lee, B. Lee, C.-H. Jung, J.-H. Choi, K. Shin, Fabrication and characterization of inkjet-printed carbon nanotube electrode patterns on paper, *Carbon*, 58 (2013) 116-127.
- [188] J. Liu, M.J. Casavant, M. Cox, D.A. Walters, P. Boul, W. Lu, A.J. Rimberg, K.A. Smith, D.T. Colbert, R.E. Smalley, Controlled deposition of individual single-walled carbon nanotubes on chemically functionalized templates, *Chemical Physics Letters*, 303 (1999) 125-129.
- [189] M.A. Meitl, Y. Zhou, A. Gaur, S. Jeon, M.L. Usrey, M.S. Strano, J.A. Rogers, Solution casting and transfer printing single-walled carbon nanotube films, *Nano Letters*, 4 (2004) 1643-1647.
- [190] J. Wang, M. Musameh, Carbon nanotube screen-printed electrochemical sensors, *Analyst*, 129 (2004) 1-2.
- [191] R.D. Deegan, Pattern formation in drying drops, *Physical Review E*, 61 (2000) 475-485.
- [192] R.D. Deegan, O. Bakajin, T.F. Dupont, G. Huber, S.R. Nagel, T.A. Witten, Capillary flow as the cause of ring stains from dried liquid drops, *Nature*, 389 (1997) 827-829.
- [193] R. Tortorich, J.-W. Choi, Inkjet printing of carbon nanotubes, *Nanomaterials*, 3 (2013) 453.

- [194] M. Anyfantakis, Z. Geng, M. Morel, S. Rudiuk, D. Baigl, Modulation of the coffee-ring effect in particle/surfactant mixtures: the importance of particle-interface interactions, *Langmuir*, 31 (2015) 4113-4120.
- [195] H. Zhang, Y. Liu, M. Kuwata, E. Bilotti, T. Peijs, Improved fracture toughness and integrated damage sensing capability by spray coated CNTs on carbon fibre prepreg, *Composites Part A: Applied Science and Manufacturing*, 70 (2015) 102-110.
- [196] A. Bédier, F. Seichepine, E. Flahaut, C. Vieu, A simple and versatile micro contact printing method for generating carbon nanotubes patterns on various substrates, *Microelectronic Engineering*, 97 (2012) 301-305.
- [197] J.W. Jo, J.W. Jung, J.U. Lee, W.H. Jo, Fabrication of highly conductive and transparent thin films from single-walled carbon nanotubes using a new non-ionic surfactant via spin coating, *ACS Nano*, 4 (2010) 5382-5388.
- [198] S.R. Shin, R. Farzad, A. Tamayol, V. Manoharan, P. Mostafalu, Y.S. Zhang, M. Akbari, S.M. Jung, D. Kim, M. Comotto, N. Annabi, F.E. Al-Hazmi, M.R. Dokmeci, A. Khademhosseini, A bioactive carbon nanotube-based ink for printing 2D and 3D flexible electronics, *Advanced Materials*, 28 (2016) 3280-3289.
- [199] L. Huang, Y. Huang, J. Liang, X. Wan, Y. Chen, Graphene-based conducting inks for direct inkjet printing of flexible conductive patterns and their applications in electric circuits and chemical sensors, *Nano Research*, 4 (2011) 675-684.
- [200] L. Hu, D.S. Hecht, G. Grüner, Carbon nanotube thin films: fabrication, properties, and applications, *Chemical Reviews*, 110 (2010) 5790-5844.
- [201] A. Lucas, C. Zakri, M. Maugey, M. Pasquali, P. van der Schoot, P. Poulin, Kinetics of nanotube and microfiber scission under sonication, *The Journal of Physical Chemistry C*, 113 (2009) 20599-20605.
- [202] D. Hecht, L. Hu, G. Grüner, Conductivity scaling with bundle length and diameter in single walled carbon nanotube networks, *Applied Physics Letters*, 89 (2006) 133112.
- [203] Y. Xia, G.M. Whitesides, Soft lithography, *Angewandte Chemie International Edition*, 37 (1998) 550-575.
- [204] J.A. Rogers, R.G. Nuzzo, Recent progress in soft lithography, *Materials Today*, 8 (2005) 50-56.

- [205] A. Kumar, H.A. Biebuyck, G.M. Whitesides, Patterning self-assembled monolayers: applications in materials science, *Langmuir*, 10 (1994) 1498-1511.
- [206] F.N. Ishikawa, H.-k. Chang, K. Ryu, P.-c. Chen, A. Badmaev, L. Gomez De Arco, G. Shen, C. Zhou, Transparent electronics based on transfer printed aligned carbon nanotubes on rigid and flexible substrates, *ACS Nano*, 3 (2009) 73-79.
- [207] D.R. Hines, S. Mezhenny, M. Breban, E.D. Williams, V.W. Ballarotto, G. Esen, A. Southard, M.S. Fuhrer, Nanotransfer printing of organic and carbon nanotube thin-film transistors on plastic substrates, *Applied Physics Letters*, 86 (2005) 163101.
- [208] C.L. Pint, Y.-Q. Xu, S. Moghazy, T. Cherukuri, N.T. Alvarez, E.H. Haroz, S. Mahzooni, S.K. Doorn, J. Kono, M. Pasquali, R.H. Hauge, Dry contact transfer printing of aligned carbon nanotube patterns and characterization of their optical properties for diameter distribution and alignment, *ACS Nano*, 4 (2010) 1131-1145.
- [209] Y.-L. Loo, R.L. Willett, K.W. Baldwin, J.A. Rogers, Additive, nanoscale patterning of metal films with a stamp and a surface chemistry mediated transfer process: Applications in plastic electronics, *Applied Physics Letters*, 81 (2002) 562-564.
- [210] Y.-S. Kim, H.-J. Ahn, S.H. Nam, S.H. Lee, H.-S. Shim, W.B. Kim, Patterned array of nanoparticles on substrates via contact printing method with CNTs/AAO stamp, *Journal of Nanoscience and Nanotechnology*, 8 (2008) 4803-4807.
- [211] Z. Fan, J.C. Ho, Z.A. Jacobson, R. Yerushalmi, R.L. Alley, H. Razavi, A. Javey, Wafer-scale assembly of highly ordered semiconductor nanowire arrays by contact printing, *Nano Letters*, 8 (2008) 20-25.
- [212] Q. Li, Y.T. Zhu, I.A. Kinloch, A.H. Windle, Self-organization of carbon nanotubes in evaporating droplets, *The Journal of Physical Chemistry B*, 110 (2006) 13926-13930.
- [213] J. Li, P.C. Ma, W.S. Chow, C.K. To, B.Z. Tang, J.K. Kim, Correlations between percolation threshold, dispersion state, and aspect ratio of carbon nanotubes, *Advanced Functional Materials*, 17 (2007) 3207-3215.
- [214] M.A.S. Mohammad Haniff, H.W. Lee, D.C.S. Bien, A.S. Teh, I.A. Azid, Highly sensitive integrated pressure sensor with horizontally oriented carbon nanotube network, *Nanoscale Research Letters*, 9 (2014) 1-5.

- [215] M.L. Chabiny, A. Salleo, Y. Wu, P. Liu, B.S. Ong, M. Heeney, I. McCulloch, Lamination method for the study of interfaces in polymeric thin film transistors, *Journal of the American Chemical Society*, 126 (2004) 13928-13929.
- [216] P. Müller, R. Kern, Equilibrium nano-shape changes induced by epitaxial stress (generalised Wulf-Kaisew theorem), *Surface Science*, 457 (2000) 229-253.
- [217] S.C. Lim, S.H. Kim, J.H. Lee, M.K. Kim, D.J. Kim, T. Zyung, Surface-treatment effects on organic thin-film transistors, *Synthetic Metals*, 148 (2005) 75-79.
- [218] A. Shimoni, S. Azoubel, S. Magdassi, Inkjet printing of flexible high-performance carbon nanotube transparent conductive films by "coffee ring effect", *Nanoscale*, 6 (2014) 11084-11089.
- [219] WHO, Avian and other zoonotic influenza: fact sheet, Available from: http://www.who.int/mediacentre/factsheets/avian_influenza/en/.
- [220] T.W.C.o.t.W.H.O.C.o.H.I. A/H5, Avian influenza A (H5N1) infection in humans, *New England Journal of Medicine*, 353 (2005) 1374-1385.
- [221] S.P. Layne, T.J. Beugelsdijk, C.K.N. Patel, J.K. Taubenberger, N.J. Cox, I.D. Gust, A.J. Hay, M. Tashiro, D. Lavanchy, A global lab against influenza, *Science*, 293 (2001) 1729-1729.
- [222] L. Xu, R. Wang, L.C. Kelso, Y. Ying, Y. Li, A target-responsive and size-dependent hydrogel aptasensor embedded with QD fluorescent reporters for rapid detection of avian influenza virus H5N1, *Sensors and Actuators B: Chemical*, 234 (2016) 98-108.
- [223] K. Malecka, A. Stachyra, A. Góra-Sochacka, A. Sirko, W. Zagórski-Ostoja, H. Radecka, J. Radecki, Electrochemical genosensor based on disc and screen printed gold electrodes for detection of specific DNA and RNA sequences derived from avian influenza virus H5N1, *Sensors and Actuators B: Chemical*, 224 (2016) 290-297.
- [224] D.J. Alexander, Avian influenza-diagnosis, *Zoonoses and Public Health*, 55 (2008) 16-23.
- [225] X. Liu, Z. Cheng, H. Fan, S. Ai, R. Han, Electrochemical detection of avian influenza virus H5N1 gene sequence using a DNA aptamer immobilized onto a hybrid nanomaterial-modified electrode, *Electrochimica Acta*, 56 (2011) 6266-6270.
- [226] K. Dybkær, M. Munch, K.J. Handberg, P.H. Jørgensen, Application and evaluation of RT-PCR—ELISA for the nucleoprotein and RT-PCR for detection of low-pathogenic H5 and H7 subtypes of avian influenza virus, *Journal of Veterinary Diagnostic Investigation*, 16 (2004) 51-56.

- [227] P. Palese, M.L. Shaw, Orthomyxoviridae: the viruses and their replication, *Fields Virology*, 2 (2007) 1647-1689.
- [228] J. Liu, H. Xiao, F. Lei, Q. Zhu, K. Qin, X.-w. Zhang, X.-l. Zhang, D. Zhao, G. Wang, Y. Feng, J. Ma, W. Liu, J. Wang, G.F. Gao, Highly pathogenic H5N1 influenza virus infection in migratory birds, *Science*, 309 (2005) 1206-1206.
- [229] B. Panigrahy, D.A. Senne, J.E. Pearson, Presence of Avian influenza virus (AIV) subtypes H5N2 and H7N1 in emus (*Dromaius novaehollandiae*) and rheas (*Rhea Americana*): virus isolation and serologic findings, *Avian Diseases*, 39 (1995) 64-67.
- [230] K.E. Wright, G.A. Wilson, D. Novosad, C. Dimock, D. Tan, J.M. Weber, Typing and subtyping of influenza viruses in clinical samples by PCR, *Journal of Clinical Microbiology*, 33 (1995) 1180-1184.
- [231] WHO, Seasonal influenza and influenza A (H1N1), Available from: http://www.who.int/ith/diseases/si_iAh1n1/en/.
- [232] E.C.J. Claas, A.D.M.E. Osterhaus, R. van Beek, J.C. De Jong, G.F. Rimmelzwaan, D.A. Senne, S. Krauss, K.F. Shortridge, R.G. Webster, Human influenza A H5N1 virus related to a highly pathogenic avian influenza virus, *The Lancet*, 351 (1998) 472-477.
- [233] Y. Ha, D.J. Stevens, J.J. Skehel, D.C. Wiley, H5 avian and H9 swine influenza virus haemagglutinin structures: possible origin of influenza subtypes, *The EMBO Journal*, 21 (2002) 865-875.
- [234] M.-S. Lee, P.-C. Chang, J.-H. Shien, M.-C. Cheng, H.K. Shieh, Identification and subtyping of avian influenza viruses by reverse transcription-PCR, *Journal of virological methods*, 97 (2001) 13-22.
- [235] P. Puthavathana, P. Auewarakul, P.C. Charoenying, K. Sangsiriwut, P. Pooruk, K. Boonnak, R. Khanyok, P. Thawachsupa, R. Kijphati, P. Sawanpanyalert, Molecular characterization of the complete genome of human influenza H5N1 virus isolates from Thailand, *Journal of General Virology*, 86 (2005) 423-433.
- [236] WHO, Influenza virus infections in humans, Available from: http://www.who.int/influenza/human_animal_interface/virology_laboratories_and_vaccines/influenza_virus_infections_humans_feb14.pdf?ua=1.

- [237] D. Vijaykrishna, J. Bahl, S. Riley, L. Duan, J.X. Zhang, H. Chen, J.S.M. Peiris, G.J.D. Smith, Y. Guan, Evolutionary dynamics and emergence of panzootic H5N1 influenza viruses, *PLOS Pathogens*, 4 (2008) e1000161.
- [238] WHO, Monthly risk assessment summary: influenza at the human-animal interface. Available from: http://www.who.int/influenza/human_animal_interface/HAI_Risk_Assessment/en/.
- [239] D.S. Song, Y.J. Lee, O.M. Jeong, Y.J. Kim, C.H. Park, J.E. Yoo, W.J. Jeon, J.H. Kwon, G.W. Ha, B.K. Kang, C.S. Lee, H.K. Kim, B.Y. Jung, J.H. Kim, J.S. Oh, Evaluation of a competitive ELISA for antibody detection against avian influenza virus, *Journal of Veterinary Science*, 10 (2009) 323-329.
- [240] B. Charlton, B. Crossley, S. Hietala, Conventional and future diagnostics for avian influenza, *Comparative Immunology, Microbiology & Infectious Diseases*, 32 (2009) 341-350.
- [241] J.S. Ellis, M.C. Zambon, Molecular diagnosis of influenza, *Reviews in Medical Virology*, 12 (2002) 375-389.
- [242] A.J. Eisfeld, G. Neumann, Y. Kawaoka, Influenza A virus isolation, culture and identification, *Nature Protocols*, 9 (2014) 2663-2681.
- [243] S. Shan, L.-S. Ko, R.A. Collins, Z. Wu, J. Chen, K.-Y. Chan, J. Xing, L.-T. Lau, A.C.-H. Yu, Comparison of nucleic acid-based detection of avian influenza H5N1 with virus isolation, *Biochemical and Biophysical Research Communications*, 302 (2003) 377-383.
- [244] B. Charlton, B. Crossley, S. Hietala, Conventional and future diagnostics for avian influenza, *Comparative Immunology, Microbiology and Infectious Diseases*, 32 (2009) 341-350.
- [245] G.K. Hirst, The agglutination of red cells by allantoic fluid of chick embryos infected with influenza virus, *Science*, 94 (1941) 22-23.
- [246] T. Francis, H.E. Pearson, J.E. Salk, P.N. Brown, Immunity in human subjects artificially infected with influenza virus, Type B, *American Journal of Public Health and the Nations Health*, 34 (1944) 317-334.
- [247] J.C. Pedersen, Hemagglutination-inhibition test for avian influenza virus subtype identification and the detection and quantitation of serum antibodies to the avian influenza virus, in: E. Spackman (Ed.) *Avian Influenza Virus*, Humana Press, Totowa, NJ, 2008, pp. 53-66.
- [248] E. Starick, O. Werner, H. Schirmer, B. Köllner, R. Riebe, E. Mundt, Establishment of a competitive ELISA (cELISA) system for the detection of influenza A virus nucleoprotein

antibodies and its application to field sera from different species, *Journal of Veterinary Medicine, Series B*, 53 (2006) 370-375.

[249] R. Saiki, S. Scharf, F. Faloona, K. Mullis, G. Horn, H. Erlich, N. Arnheim, Enzymatic amplification of beta-globin genomic sequences and restriction site analysis for diagnosis of sickle cell anemia, *Science*, 230 (1985) 1350-1354.

[250] J.S. Ellis, M.C. Zambon, Molecular diagnosis of influenza, *Reviews in Medical Virology*, 12 (2002) 375-389.

[251] T.R. Shojaei, M. Tabatabaei, S. Shawky, M.A. Salleh, D. Bald, A review on emerging diagnostic assay for viral detection: the case of avian influenza virus, *Molecular Biology Reports*, 42 (2015) 187-199.

[252] E. Spackman, D.A. Senne, T.J. Myers, L.L. Bulaga, L.P. Garber, M.L. Perdue, K. Lohman, L.T. Daum, D.L. Suarez, Development of a real-time reverse transcriptase pcr assay for type a influenza virus and the avian H5 and H7 hemagglutinin subtypes, *Journal of Clinical Microbiology*, 40 (2002) 3256-3260.

[253] W. Zhao, W.P. Zhang, Z.L. Zhang, R.L. He, Y. Lin, M. Xie, H.Z. Wang, D.W. Pang, Robust and highly sensitive fluorescence approach for point-of-care virus detection based on immunomagnetic separation, *Analytical Chemistry*, 84 (2012) 2358-2365.

[254] M. Medina-Sanchez, B. Ibarlucea, N. Perez, D.D. Karnaushenko, S.M. Weiz, L. Baraban, G. Cuniberti, O.G. Schmidt, High-Performance Three-dimensional tubular nanomembrane sensor for DNA detection, *Nano Letters*, 16 (2016) 4288-4296.

[255] M. Medina-Sánchez, B. Ibarlucea, N. Pérez, D.D. Karnaushenko, S.M. Weiz, L. Baraban, G. Cuniberti, O.G. Schmidt, High-Performance Three-dimensional tubular nanomembrane sensor for DNA detection, *Nano Letters*, 16 (2016) 4288-4296.

[256] D. Karnaushenko, B. Ibarlucea, S. Lee, G. Lin, L. Baraban, S. Pregl, M. Melzer, D. Makarov, W.M. Weber, T. Mikolajick, O.G. Schmidt, G. Cuniberti, Light weight and flexible high-performance diagnostic platform, *Advanced Healthcare Materials*, 4 (2015) 1517-1525.

[257] W.-A. Lai, C.-H. Lin, Y.-S. Yang, M.S.C. Lu, Ultrasensitive and label-free detection of pathogenic avian influenza DNA by using CMOS impedimetric sensors, *Biosensors and Bioelectronics*, 35 (2012) 456-460.

- [258] J. Thavanathan, N.M. Huang, K.L. Thong, Colorimetric detection of DNA hybridization based on a dual platform of gold nanoparticles and graphene oxide, *Biosensors and Bioelectronics*, 55 (2014) 91-98.
- [259] D. Gerion, F. Chen, B. Kannan, A. Fu, W.J. Parak, D.J. Chen, A. Majumdar, A.P. Alivisatos, Room-temperature single-nucleotide polymorphism and multiallele DNA detection using fluorescent nanocrystals and microarrays, *Analytical Chemistry*, 75 (2003) 4766-4772.
- [260] T.A. Taton, C.A. Mirkin, R.L. Letsinger, Scanometric DNA array detection with nanoparticle probes, *Science*, 289 (2000) 1757-1760.
- [261] K. Maehashi, K. Matsumoto, K. Kerman, Y. Takamura, E. Tamiya, Ultrasensitive detection of DNA hybridization using carbon nanotube field-effect transistors, *Japanese Journal of Applied Physics*, 43 (2004) L1558-L1560.
- [262] C.-P. Chen, A. Ganguly, C.-Y. Lu, T.-Y. Chen, C.-C. Kuo, R.-S. Chen, W.-H. Tu, W.B. Fischer, K.-H. Chen, L.-C. Chen, Ultrasensitive in situ label-free dna detection using a gan nanowire-based extended-gate field-effect-transistor sensor, *Analytical Chemistry*, 83 (2011) 1938-1943.
- [263] Rajesh, B.K. Das, S. Srinives, A. Mulchandani, ZnS nanocrystals decorated single-walled carbon nanotube based chemiresistive label-free DNA sensor, *Applied Physics Letters*, 98 (2011) 013701.
- [264] X. Zhu, S. Ai, Q. Chen, H. Yin, J. Xu, Label-free electrochemical detection of Avian Influenza Virus genotype utilizing multi-walled carbon nanotubes-cobalt phthalocyanine-PAMAM nanocomposite modified glassy carbon electrode, *Electrochemistry Communications*, 11 (2009) 1543-1546.
- [265] C. García-Aljaro, M.A. Bangar, E. Baldrich, F.J. Muñoz, A. Mulchandani, Conducting polymer nanowire-based chemiresistive biosensor for the detection of bacterial spores, *Biosensors and Bioelectronics*, 25 (2010) 2309-2312.
- [266] C. García-Aljaro, L.N. Cella, D.J. Shirale, M. Park, F.J. Muñoz, M.V. Yates, A. Mulchandani, Carbon nanotubes-based chemiresistive biosensors for detection of microorganisms, *Biosensors and Bioelectronics*, 26 (2010) 1437-1441.
- [267] L. Wei, D. Lu, J. Wang, H. Wei, J. Zhao, H. Geng, Y. Zhang, Highly sensitive detection of trinitrotoluene in water by chemiresistive sensor based on noncovalently amino functionalized single-walled carbon nanotube, *Sensors and Actuators B: Chemical*, 190 (2014) 529-534.

- [268] C.-H. Lin, C.-H. Hung, C.-Y. Hsiao, H.-C. Lin, F.-H. Ko, Y.-S. Yang, Poly-silicon nanowire field-effect transistor for ultrasensitive and label-free detection of pathogenic avian influenza DNA, *Biosensors and Bioelectronics*, 24 (2009) 3019-3024.
- [269] M.A. Bangar, D.J. Shirale, W. Chen, N.V. Myung, A. Mulchandani, Single Conducting polymer nanowire chemiresistive label-free immunosensor for cancer biomarker, *Analytical Chemistry*, 81 (2009) 2168-2175.
- [270] X. Tang, S. Bansaruntip, N. Nakayama, E. Yenilmez, Y.-I. Chang, Q. Wang, Carbon nanotube DNA sensor and sensing mechanism, *Nano Letters*, 6 (2006) 1632-1636.
- [271] G.-J. Zhang, L. Zhang, M.J. Huang, Z.H.H. Luo, G.K.I. Tay, E.-J.A. Lim, T.G. Kang, Y. Chen, Silicon nanowire biosensor for highly sensitive and rapid detection of Dengue virus, *Sensors and Actuators B: Chemical*, 146 (2010) 138-144.
- [272] B. Kim, J. Lee, S. Namgung, J. Kim, J.Y. Park, M.-S. Lee, S. Hong, DNA sensors based on CNT-FET with floating electrodes, *Sensors and Actuators B: Chemical*, 169 (2012) 182-187.
- [273] R.A. Villamizar, A. Maroto, F.X. Rius, I. Inza, M.J. Figueras, Fast detection of *Salmonella* *Infantis* with carbon nanotube field effect transistors, *Biosensors & Bioelectronics*, 24 (2008) 279-283.
- [274] Y. Yasuki, M. Kenzo, O. Yasuhide, M. Kazuhiko, Electrical Detection of negatively charged proteins using n-type carbon nanotube field-effect transistor biosensors, *Japanese Journal of Applied Physics*, 49 (2010) 02BD10.
- [275] O.O. Fatunmbi, J.A. Newman, V. Sivanandan, D.A. Halvorson, A broad-spectrum avian influenza subtype antigen for indirect enzyme-linked immunosorbent assay, *Avian Diseases*, 33 (1989) 264-269.
- [276] A. Abraham, V. Sivanandan, D.A. Halvorson, J.A. Newman, Standardization of enzyme-linked immunosorbent assay for avian influenza virus antibodies in turkeys, *American Journal of Veterinary Research*, 47 (1986) 561-566.
- [277] Wikipedia, ELISA, Available from: <https://en.wikipedia.org/wiki/ELISA>.
- [278] J. Huang, Z. Xie, Z. Xie, S. Luo, L. Xie, L. Huang, Q. Fan, Y. Zhang, S. Wang, T. Zeng, Silver nanoparticles coated graphene electrochemical sensor for the ultrasensitive analysis of avian influenza virus H7, *Analytica Chimica Acta*, 913 (2016) 121-127.

- [279] A. Miodek, H. Sauriat-Dorizon, C. Chevalier, B. Delmas, J. Vidic, H. Korri-Youssoufi, Direct electrochemical detection of PB1-F2 protein of influenza A virus in infected cells, *Biosensors & Bioelectronics*, 59 (2014) 6-13.
- [280] S. Song, L. Wang, J. Li, C. Fan, J. Zhao, Aptamer-based biosensors, *TrAC Trends in Analytical Chemistry*, 27 (2008) 108-117.
- [281] R. Wang, J. Zhao, T. Jiang, Y.M. Kwon, H. Lu, P. Jiao, M. Liao, Y. Li, Selection and characterization of DNA aptamers for use in detection of avian influenza virus H5N1, *Journal of Virological Methods*, 189 (2013) 362-369.
- [282] L. Brockman, R. Wang, J. Lum, Y. Li, QCM Aptasensor for rapid and specific detection of avian influenza virus, *Open Journal of Applied Biosensor*, Vol.02No.04 (2013) 7.
- [283] S.P. Layne, T.J. Beugelsdijk, C.K. Patel, J.K. Taubenberger, N.J. Cox, I.D. Gust, A.J. Hay, M. Tashiro, D. Lavanchy, A global lab against influenza, *Science*, 293 (2001) 1729.
- [284] K. Jiang, L.S. Schadler, R.W. Siegel, X. Zhang, H. Zhang, M. Terrones, Protein immobilization on carbon nanotubes via a two-step process of diimide-activated amidation, *Journal of Materials Chemistry*, 14 (2004) 37-39.
- [285] L. Chen, H. Xie, W. Yu, Functionalization methods of carbon nanotubes and its applications, INTECH Open Access Publisher, 2011.
- [286] M. Zheng, A. Jagota, E.D. Semke, B.A. Diner, R.S. McLean, S.R. Lustig, R.E. Richardson, N.G. Tassi, DNA-assisted dispersion and separation of carbon nanotubes, *Nature Materials*, 2 (2003) 338-342.
- [287] T.-T. Tran, A. Mulchandani, Carbon nanotubes and graphene nano field-effect transistor-based biosensors, *TrAC Trends in Analytical Chemistry*, 79 (2016), 222-232.
- [288] Sigma-Aldrich, Triton™ X-100, Available from: http://www.sigmaaldrich.com/catalog/product/SIAL/X100?lang=de®ion=DE&gclid=Cj0KEQjwvve_BRDmg9Kt9ufO15EBEiQAKoc6qitWUXiuuVMI7Q4PKVhBjS6O4YMDzm9-9I7VwhrS9x8aArsi8P8HAQ.
- [289] V. Bezugly, H. Eckert, J. Kunstmann, F. Kemmerich, H. Meskine, G. Cuniberti, Quantification of curvature effects in boron and carbon nanotubes: band structures and ballistic current, *Physical Review B*, 87 (2013) 245409.
- [290] M.D. de Jong, C.P. Simmons, T.T. Thanh, V.M. Hien, G.J.D. Smith, T.N.B. Chau, D.M. Hoang, N. Van Vinh Chau, T.H. Khanh, V.C. Dong, P.T. Qui, B. Van Cam, D.Q. Ha, Y. Guan,

J.S.M. Peiris, N.T. Chinh, T.T. Hien, J. Farrar, Fatal outcome of human influenza A (H5N1) is associated with high viral load and hypercytokinemia, *Nature Medicine*, 12 (2006) 1203-1207.

[291] L. Römhildt, C. Pahlke, F. Zörgiebel, H.-G. Braun, J. Opitz, L. Baraban, G. Cuniberti, Patterned biochemical functionalization improves aptamer-based detection of unlabeled thrombin in a sandwich assay, *ACS Applied Materials & Interfaces*, 5 (2013) 12029-12035.

[292] Q. Zhao, X. Lu, C.-G. Yuan, X.-F. Li, X.C. Le, Aptamer-linked assay for thrombin using gold nanoparticle amplification and inductively coupled plasma-mass spectrometry detection, *Analytical Chemistry*, 81 (2009) 7484-7489.

[293] K. Malecka, I. Grabowska, J. Radecki, A. Stachyra, A. Góra-Sochacka, A. Sirko, H. Radecka, Voltammetric detection of a specific dna sequence of avian influenza virus H5N1 using HS-ssDNA probe deposited onto gold electrode, *Electroanalysis*, 24 (2012) 439-446.

[294] K. Kurzątkowska, A. Sirko, W. Zagórski-Ostoja, W. Dehaen, H. Radecka, J. Radecki, Electrochemical label-free and reagentless genosensor based on an ion barrier switch-off system for DNA sequence-specific detection of the avian influenza virus, *Analytical Chemistry*, 87 (2015) 9702-9709.

[295] K. Malecka, I. Grabowska, J. Radecki, A. Stachyra, A. Góra-Sochacka, A. Sirko, H. Radecka, Electrochemical detection of avian influenza virus genotype using amino-ssDNA probe modified gold electrodes, *Electroanalysis*, 25 (2013) 1871-1878.

[296] I. Grabowska, K. Malecka, A. Stachyra, A. Góra-Sochacka, A. Sirko, W. Zagórski-Ostoja, H. Radecka, J. Radecki, Single electrode genosensor for simultaneous determination of sequences encoding hemagglutinin and neuraminidase of avian influenza virus type H5N1, *Analytical Chemistry*, 85 (2013) 10167-10173.

[297] S. Singh, A. Kumar, S. Khare, A. Mulchandani, Rajesh, Single-walled carbon nanotubes based chemiresistive genosensor for label-free detection of human rheumatic heart disease, *Applied Physics Letters*, 105 (2014) 213701.

[298] T. Zhang, S. Mubeen, N.V. Myung, M.A. Deshusses, Recent progress in carbon nanotube-based gas sensors, *Nanotechnology*, 19 (2008) 332001.

[299] W.-K. Jang, J.-M. Yun, H.-I. Kim, Y.-S. Lee, Improvement in ammonia gas sensing behavior by polypyrrole/multi-walled carbon nanotubes composites, *Carbon Letters*, 13 (2012) 88-93.

- [300] P. Bondavalli, P. Legagneux, D. Pribat, Carbon nanotubes based transistors as gas sensors: State of the art and critical review, *Sensors and Actuators B: Chemical*, 140 (2009) 304-318.
- [301] A. Cao, E.J. Sudholter, L.C. de Smet, Silicon nanowire-based devices for gas-phase sensing, *Sensors*, 14 (2013) 245-271.
- [302] X.T. Zhou, J.Q. Hu, C.P. Li, D.D.D. Ma, C.S. Lee, S.T. Lee, Silicon nanowires as chemical sensors, *Chemical Physics Letters*, 369 (2003) 220-224.
- [303] K.-Q. Peng, X. Wang, S.-T. Lee, Gas sensing properties of single crystalline porous silicon nanowires, *Applied Physics Letters*, 95 (2009) 243112.
- [304] N. Ramgir, N. Datta, M. Kaur, S. Kailasaganapathi, A.K. Debnath, D.K. Aswal, S.K. Gupta, Metal oxide nanowires for chemiresistive gas sensors: issues, challenges and prospects, *Colloids and Surfaces A: Physicochemical and Engineering Aspects*, 439 (2013) 101-116.
- [305] Q. Wan, Q.H. Li, Y.J. Chen, T.H. Wang, X.L. He, J.P. Li, C.L. Lin, Fabrication and ethanol sensing characteristics of ZnO nanowire gas sensors, *Applied Physics Letters*, 84 (2004) 3654-3656.
- [306] J. Janata, M. Josowicz, Conducting polymers in electronic chemical sensors, *Nature Materials*, 2 (2003) 19-24.
- [307] . u, M. Tre o, M.E. Nicho, .M. Saniger, A. arc a-Valenzuela, Adsorption kinetics of optochemical NH₃ gas sensing with semiconductor polyaniline films, *Sensors and Actuators B: Chemical*, 82 (2002) 14-23.
- [308] S.A. Waghuley, S.M. Yenorkar, S.S. Yawale, S.P. Yawale, Application of chemically synthesized conducting polymer-polypyrrole as a carbon dioxide gas sensor, *Sensors and Actuators B: Chemical*, 128 (2008) 366-373.
- [309] M. Arab, F. Berger, F. Picaud, C. Ramseyer, J. Glory, M. Mayne-L' ermite, Direct growth of the multi-walled carbon nanotubes as a tool to detect ammonia at room temperature, *Chemical Physics Letters*, 433 (2006) 175-181.
- [310] K.-P. Yoo, K.-H. Kwon, N.-K. Min, M.J. Lee, C.J. Lee, Effects of O₂ plasma treatment on NH₃ sensing characteristics of multiwall carbon nanotube/polyaniline composite films, *Sensors and Actuators B: Chemical*, 143 (2009) 333-340.

- [311] P. Qi, O. Vermesh, M. Grecu, A. Javey, Q. Wang, H. Dai, S. Peng, K.J. Cho, Toward large arrays of multiplex functionalized carbon nanotube sensors for highly sensitive and selective molecular detection, *Nano Letters*, 3 (2003) 347-351.
- [312] G. Lu, L.E. Ocola, J. Chen, Room-temperature gas sensing based on electron transfer between discrete tin oxide nanocrystals and multiwalled carbon nanotubes, *Advanced Materials*, 21 (2009) 2487-2491.
- [313] M. Penza, G. Cassano, R. Rossi, M. Alvisi, A. Rizzo, M.A. Signore, T. Dikonimos, E. Serra, R. Giorgi, Enhancement of sensitivity in gas chemiresistors based on carbon nanotube surface functionalized with noble metal (Au, Pt) nanoclusters, *Applied Physics Letters*, 90 (2007) 173123.
- [314] R. Leghrib, A. Felten, J.J. Pireaux, E. Llobet, Gas sensors based on doped-CNT/SnO₂ composites for NO₂ detection at room temperature, *Thin Solid Films*, 520 (2011) 966-970.
- [315] A.Z. Sadek, V. Bansal, D.G. McCulloch, P.G. Spizzirri, K. Latham, D.W.M. Lau, Z. Hu, K. Kalantar-zadeh, Facile, size-controlled deposition of highly dispersed gold nanoparticles on nitrogen carbon nanotubes for hydrogen sensing, *Sensors and Actuators B: Chemical*, 160 (2011) 1034-1042.
- [316] S.G. Wang, Q. Zhang, D.J. Yang, P.J. Sellin, G.F. Zhong, Multi-walled carbon nanotube-based gas sensors for NH₃ detection, *Diamond and Related Materials*, 13 (2004) 1327-1332.
- [317] L.A.P. Ruiz, Highly efficient carbon-nanostructures-based gas sensors for biomedical and other applications, Master Thesis, Technische Universität Dresden (2015).
- [318] S. Junya, Z. Guangbin, H. Masanori, Fabrication of a carbon nanotube-based gas sensor using dielectrophoresis and its application for ammonia detection by impedance spectroscopy, *Journal of Physics D: Applied Physics*, 36 (2003) L109.
- [319] N. Van Hieu, L.T.B. Thuy, N.D. Chien, Highly sensitive thin film NH₃ gas sensor operating at room temperature based on SnO₂/MWCNTs composite, *Sensors and Actuators B: Chemical*, 129 (2008) 888-895.
- [320] L.Q. Nguyen, P.Q. Phan, H.N. Duong, C.D. Nguyen, L.H. Nguyen, Enhancement of NH₃ gas sensitivity at room temperature by carbon nanotube-based sensor coated with Co nanoparticles, *Sensors (Basel, Switzerland)*, 13 (2013) 1754-1762.

- [321] A.A. Koós, R.J. Nicholls, F. Dillon, K. Kertész, L.P. Biró, A. Crossley, N. Grobert, Tailoring gas sensing properties of multi-walled carbon nanotubes by in situ modification with Si, P, and N, *Carbon*, 50 (2012) 2816-2823.
- [322] N.D. Hoa, N. Van Quy, Y. Cho, D. Kim, Porous single-wall carbon nanotube films formed by in Situ arc-discharge deposition for gas sensors application, *Sensors and Actuators B: Chemical*, 135 (2009) 656-663.
- [323] M.-R. Yu, G. Suyambrakasam, R.-J. Wu, M. Chavali, Preparation of organic-inorganic (SWCNT/TWEEN-TEOS) nano hybrids and their NO gas sensing properties, *Sensors and Actuators B: Chemical*, 161 (2012) 938-947.
- [324] R.J. Chen, N.R. Franklin, J. Kong, J. Cao, T.W. Tomblor, Y. Zhang, H. Dai, Molecular phodesorption from single-walled carbon nanotubes, *Applied Physics Letters*, 79 (2001) 2258-2260.
- [325] L. Valentini, C. Cantalini, I. Armentano, J.M. Kenny, L. Lozzi, S. Santucci, Investigation of the NO₂ sensitivity properties of multiwalled carbon nanotubes prepared by plasma enhanced chemical vapor deposition, *Journal of Vacuum Science & Technology B*, 21 (2003) 1996-2000.
- [326] T.E. Toolbox, Ammonia and health symptoms-smell and threat to life, available from: http://www.engineeringtoolbox.com/ammonia-health-symptoms-d_901.html.
- [327] The National Institute for Occupational Safety and Health (NIOSH), Nitric oxide, Available from: <https://www.cdc.gov/niosh/npg/npgd0448.html>.
- [328] Z. Jijun, B. Alper, H. Jie, L. Jian Ping, Gas molecule adsorption in carbon nanotubes and nanotube bundles, *Nanotechnology*, 13 (2002) 195.
- [329] A. Roch, M. Greifzu, E.R. Talens, L. Stepien, T. Roch, J. Hege, N. Van Nong, T. Schmiel, I. Dani, C. Leyens, O. Jost, A. Leson, Ambient effects on the electrical conductivity of carbon nanotubes, *Carbon*, 95 (2015) 347-353.
- [330] N. Peng, Q. Zhang, C.L. Chow, O.K. Tan, N. Marzari, Sensing mechanisms for carbon nanotube based NH₃ gas detection, *Nano Letters*, 9 (2009) 1626-1630.
- [331] J. Andzelm, N. Govind, A. Maiti, Nanotube-based gas sensors-role of structural defects, *Chemical Physics Letters*, 421 (2006) 58-62.

- [332] L. Valentini, L. Lozzi, C. Cantalini, I. Armentano, J. Kenny, L. Ottaviano, S. Santucci, Effects of oxygen annealing on gas sensing properties of carbon nanotube thin films, *Thin Solid Films*, 436 (2003) 95-100.
- [333] Wikipedia, Breathing, Available from: <https://en.wikipedia.org/wiki/Breathing>.
- [334] Y. Yao, C. Feng, . Zhang, Z. Liu, "Cloning" of single-walled carbon nanotubes via open-end growth mechanism, *Nano Letters*, 9 (2009) 1673-1677.
- [335] K. Balasubramanian, M. Burghard, Biosensors based on carbon nanotubes, *Analytical and Bioanalytical Chemistry*, 385 (2006) 452-468.
- [336] R.J. Chen, N.R. Franklin, J. Kong, J. Cao, T.W. Tomblor, Y. Zhang, H. Dai, Molecular photodesorption from single-walled carbon nanotubes, *Applied Physics Letters*, 79 (2001) 2258.
- [337] R.J. Chen, S. Bangsaruntip, K.A. Drouvalakis, N. Wong Shi Kam, M. Shim, Y. Li, W. Kim, P.J. Utz, H. Dai, Noncovalent functionalization of carbon nanotubes for highly specific electronic biosensors, *Proceedings of the National Academy of Sciences*, 100 (2003) 4984-4989.
- [338] K. Gong, F. Du, Z. Xia, M. Durstock, L. Dai, Nitrogen-doped carbon nanotube arrays with high electrocatalytic activity for oxygen reduction, *Science*, 323 (2009) 760-764.
- [339] W.H. Shin, H.M. Jeong, B.G. Kim, J.K. Kang, J.W. Choi, Nitrogen-doped multiwall carbon nanotubes for lithium storage with extremely high capacity, *Nano Letters*, 12 (2012) 2283-2288.
- [340] F. Garcia-Garcia, J. Alvarez-Rodriguez, I. Rodriguez-Ramos, A. Guerrero-Ruiz, The use of carbon nanotubes with and without nitrogen doping as support for ruthenium catalysts in the ammonia decomposition reaction, *Carbon*, 48 (2010) 267-276.
- [341] D.H. Lee, J.A. Lee, W.J. Lee, S.O. Kim, Flexible field emission of nitrogen-doped carbon nanotubes/reduced graphene hybrid films, *Small*, 7 (2011) 95-100.
- [342] L. Qiao, W.T. Zheng, H. Xu, L. Zhang, Q. Jiang, Field emission properties of N-doped capped single-walled carbon nanotubes: A first-principles density-functional study, *The Journal of Chemical Physics*, 126 (2007) 164702.
- [343] Y. Yao, H. Chen, C. Lian, F. Wei, D. Zhang, G. Wu, B. Chen, S. Wang, Fe, Co, Ni nanocrystals encapsulated in nitrogen-doped carbon nanotubes as Fenton-like catalysts for organic pollutant removal, *Journal of Hazardous Materials*, 314 (2016) 129-139.

[344] C. Antoine, Thermodynamic vapor pressures: New relation between the pressures and the temperatures (Thermodynamique, Tensions des Vapeurs: Nouvelle Relation entre les Tensions et les Temperatures), CR Hebd. Comptes Rendus Hebdomadaires des Séances de l'Académie, 107 (1888) 836.

Acknowledgements

Above all, I would like to thank Prof. G. Cuniberti for accepting me as a Ph.D. candidate at the Chair of Material Science and Nanotechnology, TU Dresden. It has been an absolute pleasure working in this warm group with a pleasant work atmosphere. I am particularly grateful to Prof. T. Wallmersperger, who kindly agreed to be my second referee.

Secondly, I would like to express my deepest gratitude to my advisor Dr. V. Bezugly, who gives me the opportunity to work on this project and has always been supportive of my work.

I especially thank Dr. V. Khavrus, Dr. L. Baraban, Dr. H. Yang, Dr. C. Schmädicke and Dr. B. Ibarlucea for guiding me on my experiments, and thanks to all my colleagues and co-operators, especially L. A. Panes-Ruiz and V. H. Romay-Lopez, who helped me with sensing performance detection. I sincerely thank P. Goldberg and Dr. A. Benke for the kindly help with the German translation of the abstract.

Further, I would like to thank my colleagues from IFW Dresden, first of all, Prof. M. Rümmeli, Dr. A. Bachmatiuk and Dr. I. Ibrahim for setting-up CVD synthesis experiments and helpful suggestions. Special thanks to Dr. D. Makarov and his group for producing catalyst layers, Dr. S. Oswald for the XPS analysis and Dr. I. Gonzalez for the help with TEM characterization. Further, I would like to thank also Prof. H. Li from Northwestern Polytechnical University for his kind help and collaboration. Also, I would like to say thanks to my friends for accompanying with me and supporting me.

I also appreciate financial support from China Scholarship Council (CSC), Graduate Academy (GA) and Gesellschaft von Freunden und Förderern der TU Dresden e.V. (GFF) during my Ph.D. studies.

Finally, I would like to thank my beloved parents Y. Fu and R. Yang as well as my husband K. Deng who has supported me, given me years of joy and happiness.